# PHASE SENSITIVE MEASUREMENTS OF FERROMAGNETIC JOSEPHSON JUNCTIONS FOR CRYOGENIC MEMORY APPLICATIONS

By

Bethany Maria Niedzielski

A DISSERTATION

Submitted to
Michigan State University
in partial fulfillment of the requirements
for the degree of

Physics – Doctor of Philosophy

2017

**ABSTRACT**

PHASE SENSITIVE MEASUREMENTS OF FERROMAGNETIC JOSEPHSON JUNCTIONS FOR CRYOGENIC MEMORY APPLICATIONS

By

Bethany Maria Niedzielski

A Josephson junction is made up of two superconducting layers separated by a barrier. The original Josephson junctions, studied in the early 1960's, contained an insulating barrier. Soon thereafter, junctions with normal-metal barriers were also studied. Ferromagnetic materials were not even theoretically considered as a barrier layer until around 1980, due to the competing order between ferromagnetic and superconducting systems. However, many exciting physical phenomena arise in hybrid superconductor/ferromagnetic devices, including devices where the ground state phase difference between the two superconductors is shifted by $\pi$. Since their experimental debut in 2001, so-called $\pi$ junctions have been demonstrated by many groups, including my own, in systems with a single ferromagnetic layer. In this type of system, the phase of the junction can be set to either 0 or $\pi$ depending on the thickness of the ferromagnetic layer. Of interest, however, is the ability to control the phase of a single junction between the 0 and $\pi$ states. This was theoretically shown to be possible in a system containing two ferromagnetic layers (spin-valve junctions). If the materials and their thicknesses are properly chosen to manipulate the electron pair correlation function, then the phase state of a spin-valve Josephson junction should be capable of switching between the 0 and $\pi$ phase states when the magnetization directions of the two ferromagnetic layers are oriented in the antiparallel and parallel configurations, respectively. Such a phase-controllable junction would have immediate applications in cryogenic memory, which is a necessary component to an ultra-low power superconducting computer. A fully superconducting computer is estimated to be orders of magnitude more energy-efficient than current semiconductor-based supercomputers.

The goal of this work was to experimentally verify this prediction for a phase-controllable ferromagnetic Josephson junction. To address this complicated system, first, studies of junctions with only a single ferromagnetic junction were required to determine the 0-$\pi$ transition thickness

of that material, the decay of the critical current through the junction with thickness, and the switching field of the material. The materials studied included NiFeMo, NiFe, Ni, and NiFeCo. Additionally, roughness studies of several different superconducting base electrodes and normal metal buffer and spacer layers were performed to determine the optimum junction layers. The ferromagnetic layers used were on the order of 1-2 nm thick, so a smooth growth template is imperative to maintain continuous films with in-plane magnetizations. Lastly, single junction spin-valve samples were studied. We are not equipped to measure the phase of a single junction, but series of samples where one ferromagnetic layer is systematically varied in thickness can inform the proper thicknesses needed for 0-$\pi$ switching based on relative critical current values between the parallel and antiparallel magnetic configurations.

Utilizing this background information, two spin-valve samples were incorporated in a superconducting loop so that the relative phase of the two junctions could be investigated. Through this process, the first phase-controllable ferromagnetic Josephson junctions were experimentally demonstrated using phase-sensitive measurement techniques. This provided the proof of concept for the Josephson Magnetic Random Access Memory (JMRAM), a superconducting memory system in development at Northrop Grumman, with whom we collaborate on this work. Phase-controllable systems were successfully demonstrated using two different magnetic material stacks and verified with several analysis techniques.

"For nothing is hidden except to be made manifest; nor is anything secret except to come to light."
Mark 4:22

## ACKNOWLEDGEMENTS

I have been truly blessed by the guidance and support of so many people through my time in this program. First thanks must go to my adviser, Professor Norman Birge. Joining your group was probably the best decision I made in graduate school. I appreciate all the opportunities you gave me to present my work at conferences and collaboration meetings, prepare technical documents for publications and conference calls, and network with academic and industry professionals. I always feel that you respect and value my scientific opinion, giving me confidence in my abilities as a researcher. It will be a difficult task to find a better boss.

Next, I must thank Professor William Pratt. In addition to your council on the direction of my work and design and upkeep of much of the essential measurement equipment, you were a fount of knowledge on topics from spin-flip scattering to boating knots. I hope to one day know as much physics as you have forgotten.

The labs in the basement would all be in pieces without the care and dedication of Dr. Reza Loloee. Thank you for all the maintenance procedures that keep our lab running smoothly, for teaching me your sputtering and ion mill operational tips and tricks, and for being my lifeline when something goes wrong. Besides the invaluable technical support, you encourage a friendly and respectful work environment by taking the time to laugh and joke and engage with us lowly graduate students. In the clean room, Dr. Baokang Bi similarly upkeeps the shared equipment and is an invaluable technical resource. Thanks for your patient teachings on all the clean room equipment and project counsel.

When I joined the Birge group, I had very little experience in condensed matter physics research. My success is largely due to the mentorship from my fellow group members, both past and present. I need to thank by name Eric Gingrich, Yixing Wang, Bill Martinez, Joseph Glick, Alex Cramer, Mazin Khasawneh, Victor Aguilar, and Josh Willard for their guidance and friendship. Special thanks to Joseph Glick for invaluable Mathematica analysis software, most notably to fit the SQUID oscillations, and Victor Aguilar for faster and better featured Labview measurement

software. I know I leave this group in capable hands and look forward to the great work to come.

My research was greatly aided from collaboration with Northrop Grumman and Arizona State University. Special thanks go to Nick Rizzo, Don Miller, Anna Herr, and Ofer Namman. I am also grateful to Northrop Grumman and IARPA for funding this work.

I have been able to fully focus on my research due to the excellent support staff in the P-A department. Superstars like Debbie Barratt, Cathy Cords, Lisa Ruess, and especially Kim Crosslan have made all the non-technical aspects of my MSU tenure incredibly smooth.

Outside of work, I need to thank my fellow classmates who pulled me through my first year courses and even managed to make it a fun experience at times. Since then I have been lucky to meet even more great friends here in Michigan, some who cared enough to drive to Connecticut to help celebrate my wedding. The past and present members of the Grand Canonical Ensemble gave me a fun and creative artistic outlet. All the students and faculty who supported my goals for the Women and Minorities in the Physical Sciences (WaMPS) group have my sincere appreciation. Especially my officers for the past three years have really helped me turn WaMPS into a strong and impactful group.

Through it all, I have been blessed with the love and support of an incredible family. My parents have always encouraged my scientific interests and pushed me to be my best. They are my biggest champions when things are going well and a listening ear when they are not. I have the best siblings in Amanda, Drew, and Luke who share my silly voice and remind me what is important in life. Most of all, I must thank my husband, Andrew Huffman. You have continually made sacrifices to enable my career goals and just been my rock through this whole crazy process. I know we can do anything together. You truly are my favorite.

Lastly, I would like to thank my committee members, Professor Phil Duxbury, Professor Stuart Tessmer, Professor Don Morelli, and Professor Brian O'Shea for their direction and guidance over the years.

To all those named and unnamed, I greatly appreciate your impact on my success and I couldn't have done it without you.

## TABLE OF CONTENTS

## LIST OF TABLES

## LIST OF FIGURES

# CHAPTER 1

# INTRODUCTION

## 1.1 Motivation

The growth of Information Technology over the past several decades has been dramatic and impressive. But, this growth comes with a cost: supercomputer and data center facilities now use a noticeable fraction of the world's electrical power budget. There is a strong incentive to develop new computing technologies that are substantially more energy efficient than our existing semiconductor-based technology. The development of a fully superconducting computer is one approach being pursued. Such a computer would take advantage of energy efficiencies in three major areas: logic, memory, and interconnects. Some workers believe that such a computer could be up to 100 times more efficient than a semiconductor-based computer, even taking into account the energy used to cool the entire system to liquid helium temperatures [38].

A superconducting supercomputer could have many potential advantages. Josephson junctions switch on the picosecond time-scale and dissipate very little energy per switch. Single Flux Quantum logic circuits transmit small current pulses between neighboring loops that can travel at speeds up to 1/3 of the speed of light [51]. Several energy-efficient variants of that logic have been developed over the past several years [51, 56, 43, 81, 37], but this technology has not yet become competitive, in part due to the lack of a compatible superconducting memory [76].

Recently, Josephson junctions with ferromagnetic interlayers (SFS junctions) have attracted interest for the role they can play in addressing this issue. The theory behind these devices will be explained in Chapter 2. Proposals to use ferromagnetic Josephson junctions in memory applications come in several flavors, with some using the orbital or field effect [50, 34, 19, 5], and others using the exchange field [35, 1, 10, 31]. Among those using the exchange field, the bit can be controlled using either the amplitude of the critical current or the ground-state phase across the junction [65, 4, 50]. In this work, we focus on the development of Josephson Magnetic Random

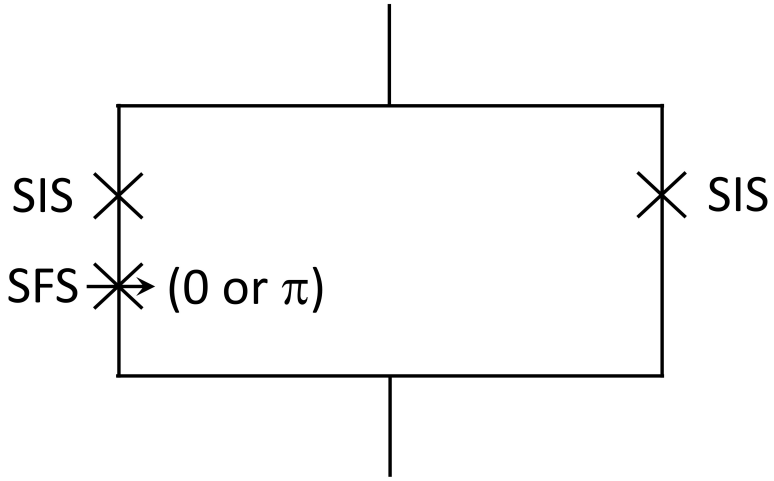


Figure 1.1 **Simplified Schematic of JMRAM Cell Layout.** The cell includes two SIS junctions and the phase-controllable SFS junction together in a superconducting loop. As described in Chapter 2, the critical current of the loop will oscillate with the applied flux through the loop. This leads to the cell having a larger critical current when the SFS junction contributes 0 additional phase into the loop and a smaller critical current when the SFS junction contributes $\pi$ additional phase into the loop.

Access Memory (JMRAM) which uses the exchange field and phase control [35, 36]. We are drawn to this approach due to its advantages in scaling and operational speed.

JMRAM is currently being developed by Northrop Grumman Corporation and draws inspirations from the field of spintronics, and specifically from commercial MRAM, which has been designed and marketed by Everspin Technologies [64]. In JMRAM, the phase-switching element would be a Josephson junction with two ferromagnetic layers. Changing the relative magnetization directions of these two layers between the parallel and anitparallel configuration can change the ground-state phase difference of the junction between $\pi$ and 0. The mechanism for this is explained in Chapter 2. The JMRAM design incorporates this phase-controllable Josephson junction into a superconducting loop with two conventional SIS junctions (junctions with an insulating barrier) which is shown schematically in Figure 1.1. This design uses the SFS junction only as a passive phase shifter, either adding an additional 0 or $\pi$ phase into the loop. Because the critical current of the loop will naturally oscillate with phase, this results in the loop having a high critical current when the SFS junction is in the 0 state and a low critical current when the SFS junction is in the $\pi$

state. These two states would act as the 0 and 1 of the memory system. You can imagine biasing the loop at a current between the high and low value and if the cell is in the 0 state, its critical current will be larger than this bias and nothing will happen, and if the cell is in the $\pi$ state, its critical current will be exceeded and it will emit a measurable voltage pulse. The speed of this "read" operation is inversely proportional to the critical current times normal state resistance, or $I_cR_N$. In this case where the SFS junction is used as a passive phase shifter, the voltage pulse will be produced by the SIS junctions, which is a major advantage of the JMRAM design since the SIS junctions have a much larger $I_cR_N$ product than the SFS junctions. If the critical current of the SFS junction is larger than that of the SIS junctions in the loop, then only the latter will switch into the normal state when the critical current of the SQUID is exceeded. This leads to an extremely energy efficient read operation for the memory cell. For more details, see [28, 35, 36]. In parallel, Northrop Grumman is also developing logic that is compatible with this memory system. Together, they form an important stepping stone towards a fully superconducting computer.

## 1.2 Thesis Structure

This thesis will detail my work on the phase-control and optimization of Josephson junctions with ferromagnetic interlayers for use in memory applications. It is structured as follows: Chapter 2 will describe the theoretical background needed to understand this work, introducing the topics of Josephson junctions, the proximity effect at superconductor/normal metal and superconductor/ferromagnet interfaces, phase effects in ferromagnetic Josephson junctions, and properties of dc SQUIDs. Chapter 3 details the sample fabrication process used in this work including a discussion of the relevant equipment and detailed processing steps. Chapter 4 will share my results from several studies aimed at reducing the roughness of the base superconducting electrode and the normal metal spacer layers to enhance the properties of the junctions overall. In Chapter 5, magnetometry measurements of blanket thin films of various magnetic materials are shown. All these materials will be used later in this work in Josephson junctions. Chapters 6 and 7 show the

results of Josephson junction studies that include a single ferromagnetic layer or two ferromagnetic layers respectively. Chapter 8 details the crowning achievement of this work, the demonstration of a phase-controllable Josephson junction with two ferromagnetic layers. After the initial demonstration, several additional devices using different materials and design schemes were also tested to optimize the phase control. Lastly, Chapter 9 will give a summary of the results and look forward to future work that can build on this progress.

# CHAPTER 2

# THEORETICAL BACKGROUND

Since the discovery of superconductivity in 1911 [59], over 20 elemental superconductors have been found and many useful devices have been developed. Below a critical temperature, these materials allow current to flow with no dissipation and completely eject magnetic field lines from their interior. These phenomena are inherently quantum mechanical in nature, but manifest themselves on a macroscopic scale. For conventional superconductors, including those studied in this work, a full microscopic theory (called BCS theory) was developed by J. Bardeen, L.N. Cooper and J.R. Schrieffer in 1957 [7, 8]. This theory identified that the dissipationless current flow of the superconducting state is due to electron pairs (called Cooper pairs) that have opposite spin and opposite momenta. These Cooper pairs form a zero-spin state and act as a boson, which allows the entire ensemble of pairs to condense to the lowest energy state characterized by a single phase-coherent wavefunction. This leads to interesting effects in systems that combine superconductors with normal metals and especially ferromagnets. In this chapter, I will discuss the theory of the Josephson equations, the RCSJ model for Josephson junction circuit elements, the effect of a magnetic field on the critical current of a Josephson junction, the superconducting proximity effect in normal metal and ferromagnetic materials, the phase properties of ferromagnetic Josephson junctions, and Superconducting QUantum Interference Devices (SQUIDs).

## 2.1 Josephson Junctions

In 1962, Brian Josephson analyzed the behavior of the junction between two closely spaced superconductors separated by an insulating barrier. If this insulating barrier is thin enough, Josephson postulated that electron pairs would be able to tunnel through the barrier [40, 41]. This type of system with two superconductors separated by an insulating layer became known as a Josephson junction, and the barrier material was later expanded to include normal metals and ferromagnets.

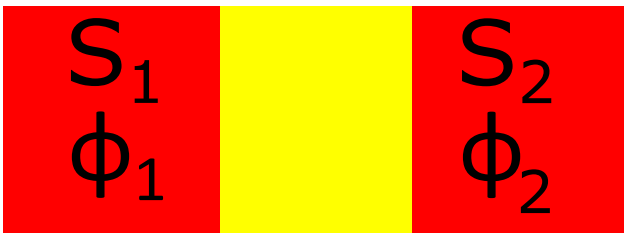


Figure 2.1 **Cartoon of a Josephson junction.** $S_1$ and $S_2$ are the two superconducting electrodes which are separated by a non-superconducting barrier material. Each superconductor has its own macroscopic phase. As defined in the text, the junction carries a positive supercurrent flowing for $S_1$ to $S_2$.

Each superconductor is characterized by a macroscopic phase $\phi$ as shown in Figure 2.1. Two equations, called the Josephson equations govern the flow of supercurrent ($I_S$) across the junction. The first equation

$$I_S = I_c sin\phi \tag{2.1}$$

shows how the supercurrent varies with $\phi$, the phase difference between the two superconducting electrodes ($\phi_2$ - $\phi_1$). $I_c$ is the maximum or critical current of the junction. If the critical current is exceeded, a voltage will arise across the junction. This equation is also called the current-phase relation. If a constant voltage V is applied to the Josephson junction, we obtain

$$\frac{\delta\phi}{\delta t} = \frac{2e}{\hbar}V = \frac{2\pi}{\Phi_0}V \tag{2.2}$$

where $\Phi_0$ is the flux quantum with a value of $\frac{h}{2e}$ = 2.07*$10^{-15}$ Wb. This second Josephson equation is also called the voltage-phase relation. Together, they describe the behavior of a Josephson junction and lead to several interesting effects. The DC Josephson effect states that a DC current can be drawn through the junction without any voltage drop as long as the current is smaller than $I_c$ and $\phi$ has a constant, nonzero value. When a constant voltage is applied to the junction, the phase different between the two superconductors will vary linearly with time, causing the current through the junction to oscillate with an amplitude of $I_c$ and a frequency of $\frac{2e}{h}$V. This is called the AC Josephson effect.

These Josephson equations can be derived by following the arguments laid out by L.D. Landau and E.M. Lifschitz [48] or from the famous Feynman lectures [26]. The predictions from

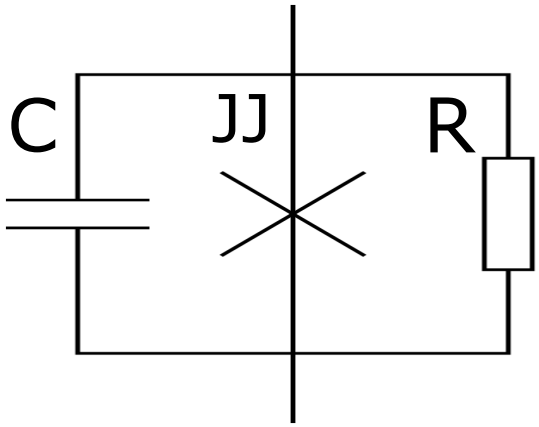


Figure 2.2 **Circuit equivalent of the RCSJ Model showing a capacitor and resistor in parallel with the Josephson junction supercurrent**

this formalism were experimentally validated only one year after Josephson's paper by Philip W. Anderson and John M. Rowell [2].

### 2.1.1 Resistively and Capacitively Shunted Junction (RCSJ) Model

The RCSJ model is used to gain some insight into the dynamics of a Josephson junction by describing the DC current-voltage characteristic. In this model, the Josephson junction has a critical current $I_c$ and is in parallel with its self-capacitance C and a resistance R [79, 73, 53]. The equivalent circuit is shown in Figure 2.2. This model assumes a linear resistance and neglects the current noise from the resistor. Adding the current through these elements gives

$$I = I_c sin\phi + \frac{V}{R} + C\frac{dV}{dt}. \tag{2.3}$$

Combining this with the second Josephson relation, equation 2.2, we find that

$$I = I_c sin\phi + \frac{\Phi_0}{2\pi}\frac{1}{R}\frac{d\phi}{dt} + \frac{\Phi_0}{2\pi}C\frac{d^2\phi}{dt^2} \tag{2.4}$$

If we multiply by $\frac{\Phi_0}{2\pi}$, use the Josephson coupling energy $E_{J0} = \frac{\Phi_0}{2\pi}I_c$, normalize the current with $i_n = \frac{I}{I_c}$, and re-arrange the terms, we find that

$$\left(\frac{\Phi_0}{2\pi}\right)^2 C\frac{d^2\phi}{dt^2} + \left(\frac{\Phi_0}{2\pi}\right)^2 \frac{1}{R}\frac{d\phi}{dt} + \frac{d}{d\phi}(E_{J0}[1 - cos\phi - i_n\phi]) = 0 \tag{2.5}$$

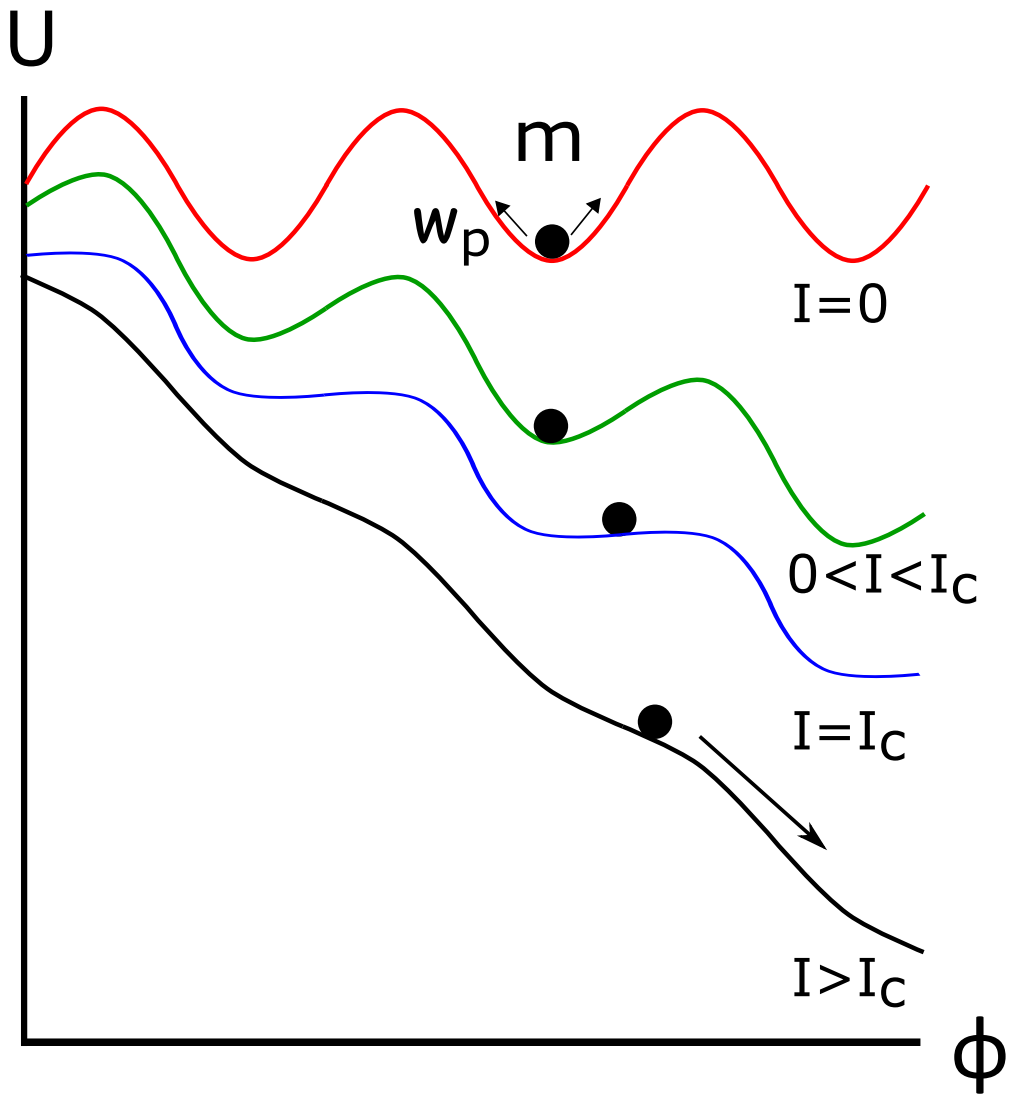


Figure 2.3 **Tilted Washboard Potential Analogy** Analogy between the motion of the phase different of a Josephson junction and the damped motion of a particle of mass m in the tilted washboard potential. When the current through the junction is low, the 'mass' is trapped in one well of the potential and can oscillate at the plasma frequency. The increase in current is modeled as increasing the tilt of the potential. As the current is increased, the barrier height is reduced until the applied current equals the critical current where any fluctuation can send the particle out of its well. Above the critical current, there are no stable states and the particle will move freely along the potential.

This equation describes the equation of motion for the phase difference across the junction and is analogous to the equation of motion of a particle with mass m and damping $\eta$ in a potential U:

$$m\frac{dx^2}{dt^2} + \eta\frac{dx}{dt} + \nabla U = 0. \tag{2.6}$$

Comparing these equations, we find that

$$m = \left(\frac{\Phi_0}{2\pi}\right)^2 C \tag{2.7}$$

$$\eta = \left(\frac{\Phi_0}{2\pi}\right)^2 \frac{1}{R} \tag{2.8}$$

$$U = E_{J0}[1 - cos\phi - i_n\phi] \tag{2.9}$$

Examining these relationships, we see that the mass of the particle is proportional to the capacitance C, the damping is inversely proportional to the resistance R, and the potential is that of a tilted washboard. This description is visualized in Figure 2.3. When there is no current through the junction, the particle is confined to a potential minimum. The time average of the phase difference, and hence the time averaged dc voltage, is zero in this state. Increasing the current corresponds to tilting the potential and lowering the barrier for the particle. If the current exceeds the critical current, the washboard is tilted so far that the particle can't stay in its well and it will slide down the washboard. This dynamic case is associated with a finite dc voltage across the junction which increases with increasing bias current.

Equation 2.5 is commonly written in reduced units by using the normalized time $\tau = t\frac{2\pi I_c R}{\Phi_0}$ and the Stewart-McCumber parameter $\beta_c = \frac{2\pi}{\Phi_0} I_c R^2 C$ [73, 53] to get

$$\beta_c\frac{d^2\phi}{d\tau^2} + \frac{d\phi}{d\tau} + sin\phi - i_n = 0. \tag{2.10}$$

If we neglect the damping and consider a horizontal potential (zero driving current) and small amplitudes (so $\sin\phi \simeq \phi$) then we can write equation 2.10 as

$$\beta_c\frac{d^2\phi}{d\tau^2} + \phi = 0. \tag{2.11}$$

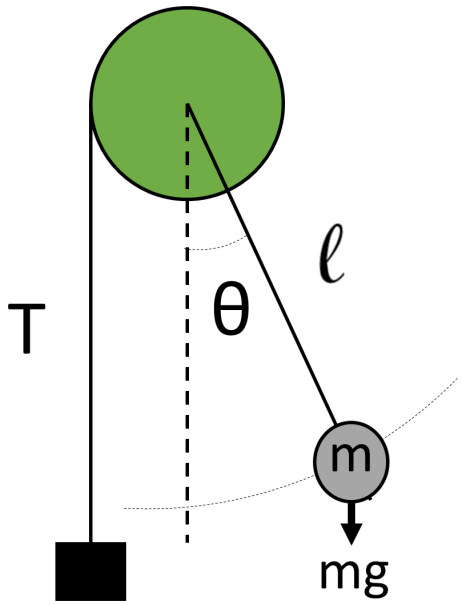


Figure 2.4 **Pendulum Analogy** Analogy between the motion of the phase different of a Josephson junction and the damped motion of a physical pendulum. The pendulum has mass m and length $\ell$ deflected by angle $\theta$ due to a torque T that is represented by an unwinding mass.

The solution of that equation is

$$\phi = Ae^{i\frac{\tau}{\sqrt{\beta_c}}} = Ae^{i\omega_p t}. \tag{2.12}$$

where A is a constant and the plasma frequency $\omega_p = \sqrt{\frac{2\pi I_c}{\Phi_0 C}}$. The plasma frequency represents the oscillation frequency of the particle around the potential minimum at small amplitudes.

Another mechanical analogue that can be used to describe the dynamics of a Josephson junction is a physical pendulum. The pendulum is defined by mass m and length $\ell$ that is deflected from normal by an angle $\theta$ inflicted by a torque T. This torque is directed parallel to the rotation axis and has a magnitude of the product between the gravitational force mgsin$\theta$ and the pendulum length $\ell$. This system is shown in Figure 2.4 and is represented by the equation of motion

$$T = \Theta\ddot{\theta} + \Gamma\dot{\theta} + mg\ell sin\theta. \tag{2.13}$$

where $\Theta = m\ell^2$ is the moment of inertia of the pendulum and $\Gamma$ is the damping coefficient. By comparing with equation 2.4, we see that they are equivalent with I $\leftrightarrow$ T, $I_c \leftrightarrow$ mg$\ell$, $\Phi_0/2\pi$R $\leftrightarrow \Gamma$, C$\Phi_0/2\pi \leftrightarrow \Theta$, and $\phi \leftrightarrow \theta$. The dynamics of the Josephson junction correspond to the

dynamics of an oscillation or rotation of the pendulum. When the torque is zero, the pendulum will oscillate around its equilibrium position with a frequency of $\sqrt{g/\ell}$ which corresponds to the plasma frequency of the Josephson junction. A finite torque that causes a constant deflection angle of the pendulum corresponds to a finite current less than the critical current being applied to the Josephson junction, causing a constant phase difference across the junction. A torque that deflects the pendulum by 90° or more causing a rotation of the pendulum corresponds to a current above the critical current and causes a changing phase difference in the Josephson junction, and therefore a finite voltage.

### 2.1.2 Overdamped Josephson Junction

We will now consider the case of an overdamped Josephson junction, which corresponds to the type that are measured in this work. In this case, $\beta_c = 2\pi I_c R^2 C/\Phi_0 \ll 1$, so the junction capacitance and/or resistance are small, corresponding to a particle with a small mass and large damping in the tilted washboard scheme. If you imagine this limiting case starting with a current larger than the critical current and reducing to zero, the strong damping will cause the particle to become re-trapped in a local minima as soon as the current is less than the critical current. This leads to a non-hysteretic current-voltage characteristic for the overdamped Josephson junction. To derive the current-voltage relationship, we can neglect the $\beta_c$ term from equation 2.10 to get

$$\frac{d\phi}{d\tau} + sin\phi - i_n = 0. \tag{2.14}$$

At values less than the junction critical current, we expect all the current to flow as supercurrent. The voltage phase relation implies that the junction is in the zero voltage state so there is no time evolution of the phase. This leads to the relationship

$$\phi = sin^{-1} i_n \qquad for \quad i_n \leq 1. \tag{2.15}$$

Above the critical current, the full time dependence of the relationship must be taken into account. Integrating equation 2.14, it can be shown that the time-averaged voltage has the following form

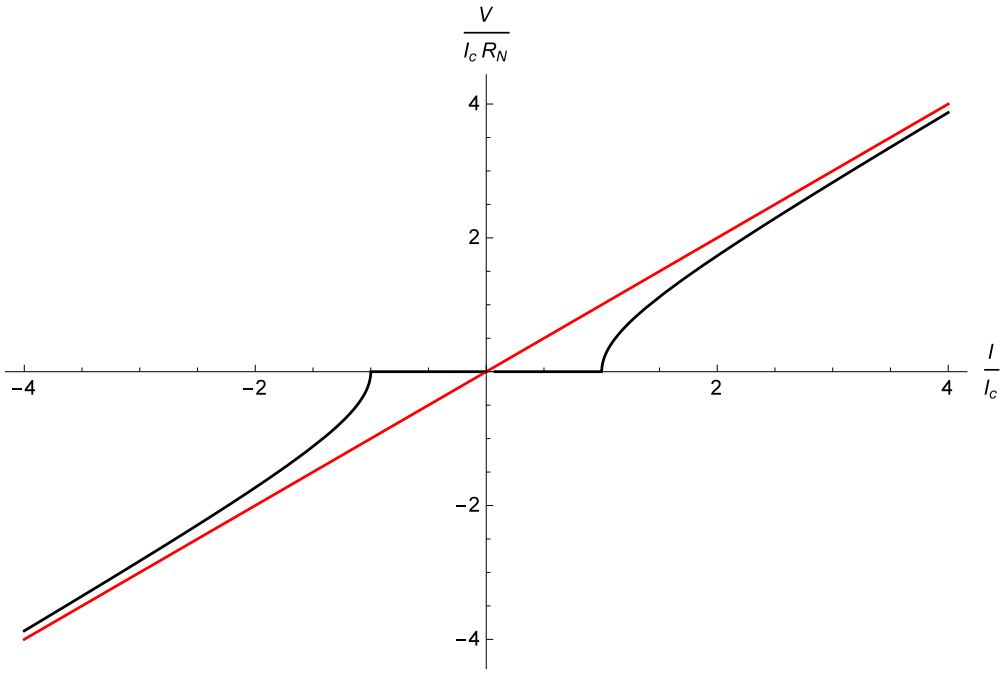


Figure 2.5 **IV characteristic for an overdamped Josephson junction** The black curve represents equation 2.16 with zero voltage for currents below the critical current and voltages approaching Ohm's Law (shown in red) above the critical current.

[32]:

$$\langle V(t)\rangle = I_c R\sqrt{i_n^2 - 1} = I_c R\sqrt{\left(\frac{I}{I_c}\right)^2 - 1} \qquad for \quad I > I_c \tag{2.16}$$

At current values much greater than the critical current, this equation approaches Ohm's Law. The full current-voltage characteristic for an overdamped Josephson junction is shown in Figure 2.5.

### 2.1.3 Short Circular Junction in a Magnetic Field

So far, we have only considered zero-dimensional Josephson junctions characterized by the Josephson current $I_s$ with maximum value $I_c$, and the phase difference $\phi$ across the junction. Now we will allow for spatial variations in the supercurrent and phase difference and we will show that spatial interference in the Josephson junction can be observed if we apply an external magnetic field [9, 32]. The observed interference effect is analogous to the single slit diffraction pattern in optics. We will examine the short junction case, where the magnetic field generated by the Josephson current itself is negligible compared to the externally applied magnetic field. Consider a circular

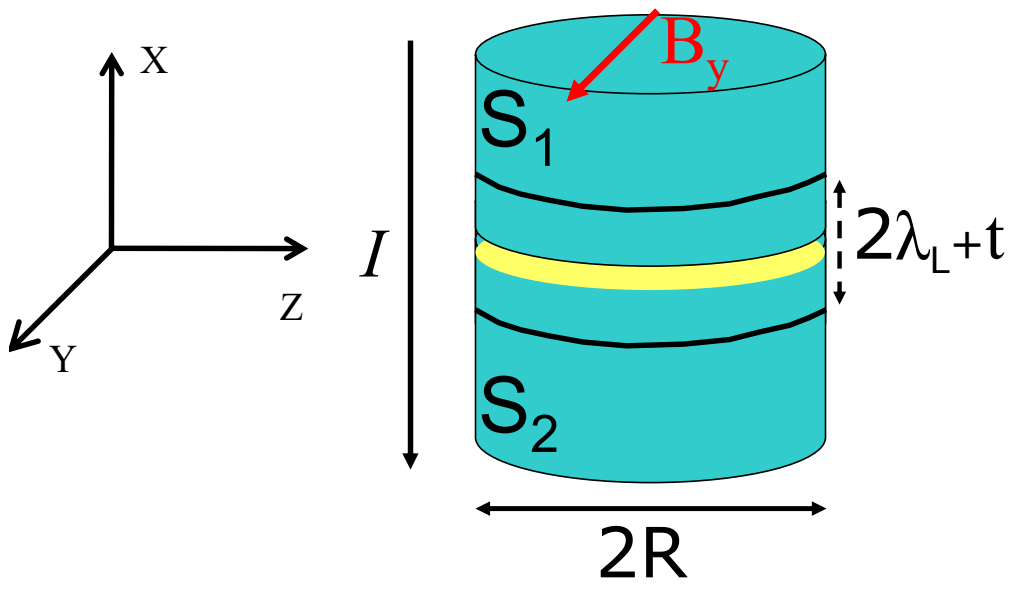


Figure 2.6 **Circular Josephson Junction in a Magnetic Field** Circular Josephson Junction with radius R in a Magnetic Field $H_y$. The current flows through the junction in the x-direction, t is the thickness of the junction barrier layer and $\lambda_L$ is the London penetration depth.

Josephson junction with radius R in an external field H = (0, $H_y$, 0) as shown in Figure 2.6. When a uniform external field is applied to the junction, the field will decay inside the superconductor as $e^{-|x|/\lambda_L}$ where $\lambda_L = \sqrt{\frac{m}{\mu_0 n e^2}}$. The phase difference will have spatial dependence as

$$\nabla\phi = \left(\frac{2\pi}{\Phi_0}d\right)\boldsymbol{H}\times\hat{\boldsymbol{x}} \tag{2.17}$$

where d = $2\lambda_L$ + t, t is the barrier thickness, H is the magnetic field in the plane of the junction (including both the externally applied magnetic field and the field generated by currents flowing in the junction), and $\hat{x}$ is the unit vector in the x direction. Integrating this equation for a field in the y-direction, we find

$$\phi(z) = \frac{2\pi d}{\Phi_0}H_y z + \phi_0 \tag{2.18}$$

where $\phi_0$ is an integration constant. There is a linear spatial variation in the z-direction which is proportional to the applied magnetic field. Plugging this result into the first Josephson relation, we find that

$$J(z) = J_c sin\left(\frac{2\pi d}{\Phi_0}H_y z + \phi_0\right). \tag{2.19}$$

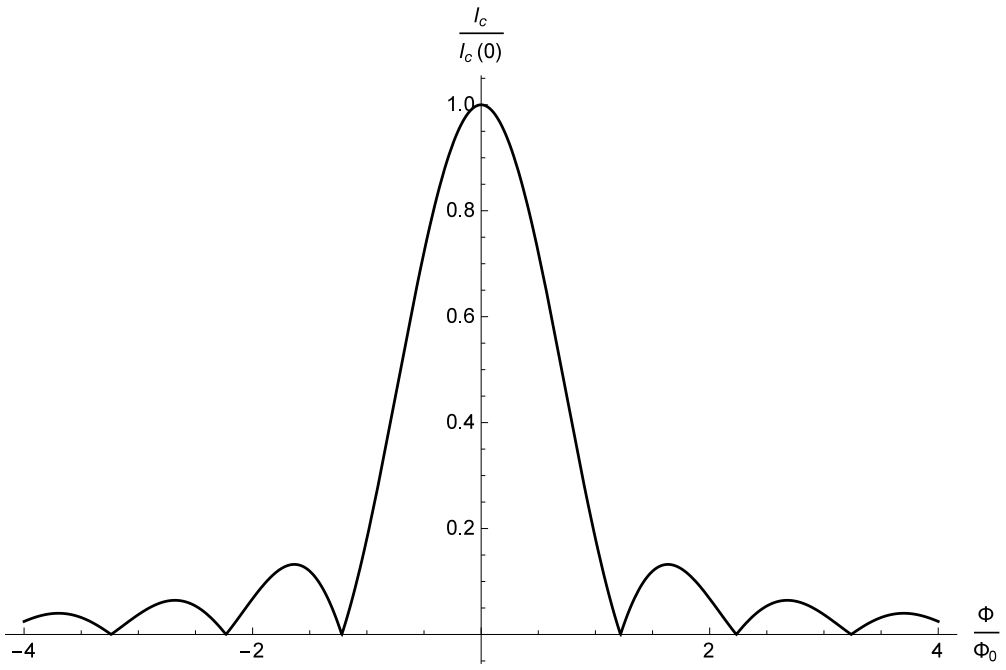


Figure 2.7 **Airy Diffraction Pattern** Maximum critical current vs normalized flux through the a circular junction resulting in an Airy Pattern.

This indicates that the current density has a periodic nature inside the junction which will lead to certain values of the external magnetic field that result in zero net current through the junction. The total current in the junction is given by

$$I = \int\int dydz J_c sin\left(\frac{2\pi d}{\Phi_0} H_{yz} + \phi_0\right) \tag{2.20}$$

where integration is performed over the junction area. For the case of a circular junction with radius R, this integral can be solved and maximized [52] to give

$$I_c = 2I_{c0}\left|\frac{J_1(\frac{\pi\Phi}{\Phi_0})}{\frac{\pi\Phi}{\Phi_0}}\right| \tag{2.21}$$

where the critical current with no external field $I_{c0} = \pi J_c R^2$, $J_1$ is the Bessel function of first kind and order, and the flux through the junction $\Phi = B_y 2R(2\lambda_L + t)$. This result is known as an Airy pattern and it is plotted in Figure 2.7. Though calculated for a circular junction, the resulting pattern is the same for the elliptical junctions studied in this work. If calculated for a rectangular junction, the result is called a Fraunhofer pattern with a similar mathematical form to the optical

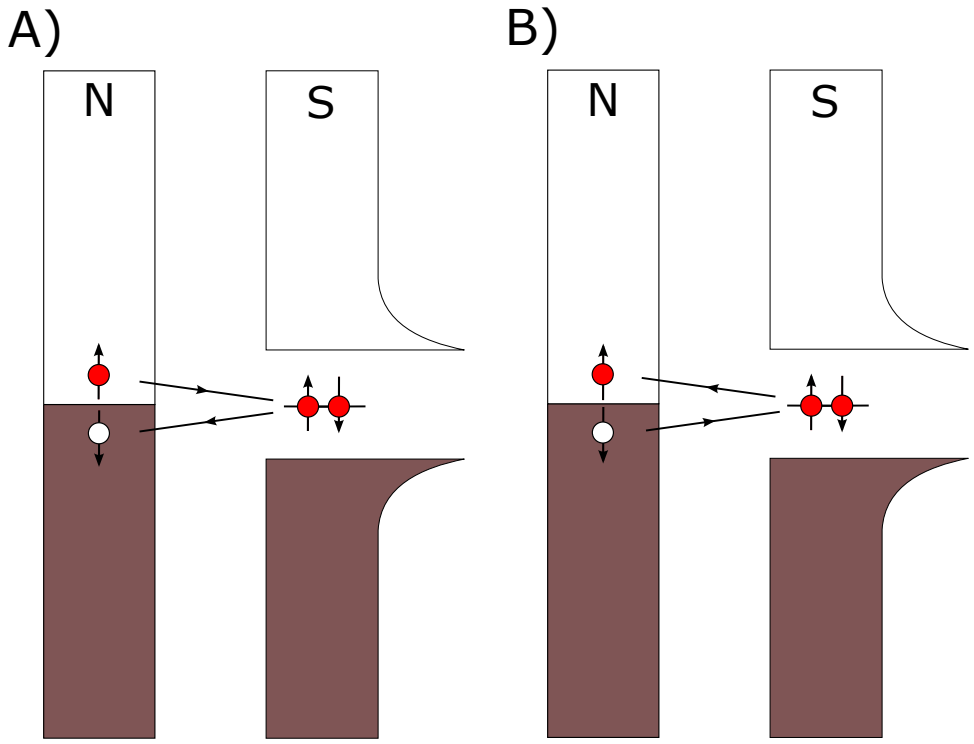


Figure 2.8 **Schematic of Andreev Reflection** Schematic of Andreev Reflection using the semiconductor model of a superconductor. The energy bands for the normal metal N and superconductor S are shown filled up to the Fermi energy. Electrons are shown as red circles and holes as white circles. For electrons to flow across this boundary, the process must exchange a charge of -2e. In Andreev Reflection A) this is modeled as an electron in N traveling into S and retroreflecting a hole back into N, thus creating a Cooper pair in S. In Inverse Andreev Reflection B) a Cooper pair in S can travel into N as a hole incident on the interface and a retroreflected electron.

Fraunhofer pattern. Throughout this thesis, the term "Fraunhofer pattern" is used in place of "Airy pattern" due to colloquialism and the similar shape of the two functions.

## 2.2 S/N and S/F Proximity Effects

Thus far, all the properties that have been derived for Josephson junctions are general, and apply to junctions of any barrier type. Now we will turn our attention to the specific effect that ferromagnetic materials have on the junction by comparing the effect of a superconductor (S)/normal metal (N) interface with a superconductor (S)/ferromagnet (F) interface.

When a material becomes superconducting, the electrons at the Fermi level begin to pair up into Cooper pairs. This leaves behind an energy gap in the single-electron density of states. The electrons in a normal metal are nonlocalized with single-electron states filled up to the Fermi level. You might then naively assume that these two materials could not exchange electrons, but this is not the case. The microscopic model that describes how electrons can flow in this system is called Andreev Reflection [3] and is shown schematically in Figure 2.8. Consider an electron in N with spin $\uparrow$, momentum $k$, and energy above the Fermi level but below the superconductor energy gap. There are no single-electron states in the superconductor, so the electron must find a partner in N with opposite spin, momenta, and energy. Then these two electrons can fill a Cooper pair state in S at the Fermi level, but must leave behind a hole in N with spin $\downarrow$ and momentum $-k$ below the Fermi level. The inverse of this process is also allowed to transmit Cooper pairs into the normal metal. In all processes across this interface, an exchange of 2e is required.

In the case where Cooper paired electrons travel into the normal metal, those electrons are no longer paired, but do retain a phase coherence with each other up to a certain length scale in N. This length scale has a different functional form depending on if the electron transport in N is in the diffusive or ballistic limit [21, 60, 23]. These limits depend on the relationship between the pair coherence length in N, $\xi_N$, (defined momentarily), and the electronic mean free path, $l$. The ballistic or clean limit is defined when the mean free path is much larger than $\xi_N$. In this case, the electrons are moving at the Fermi velocity and travel in relatively straight paths without scattering through N, leading to a coherence length through the normal metal of $v_F * \tau$ where $v_F$ is the Fermi velocity of the electrons and $\tau = \frac{\hbar}{\varepsilon}$ is the coherence time. Taking the convolution of this length scale with the Fermi-Dirac distribution with respect to energy, we find that only energies within $k_B$T of the Fermi energy have a significant contribution, so we can write $\varepsilon \approx 2\pi k_B T$. This leads to a normal metal coherence length of

$$\xi_N = \frac{\hbar v_F}{2\pi k_B T} \tag{2.22}$$

in this limit. The diffusive or dirty limit is characterized by a mean free path that is much shorter than $\xi_N$, leading to multiple scatterings of the electrons as they travel through N according to the

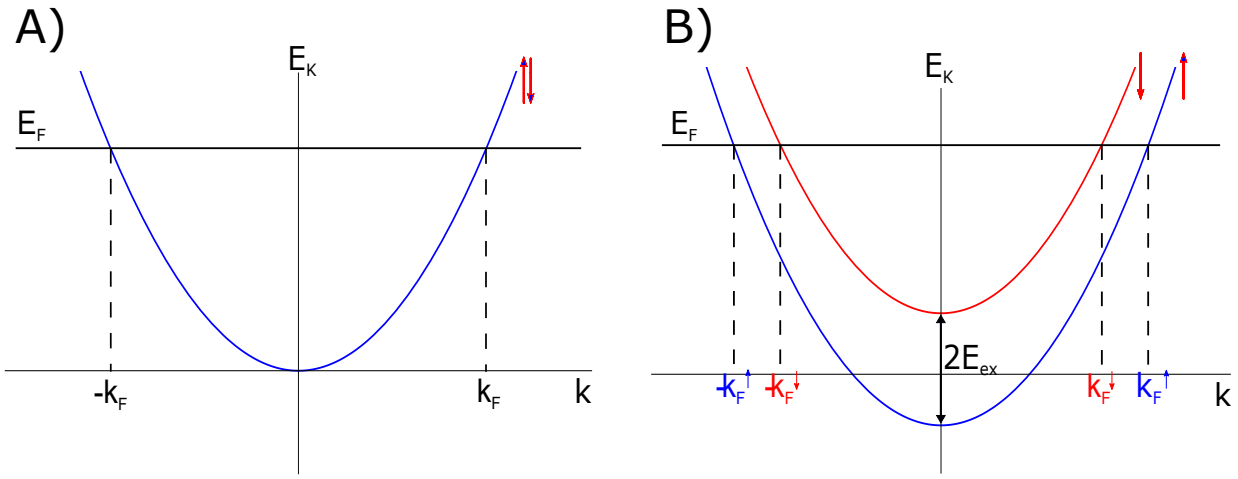


Figure 2.9 **S/F Interface Band Structure** Toy band structure for S/F interface. The band structure of the ferromagnet is modeled as a normal metal in a magnetic field with Zeeman splitting equal to twice the exchange energy of the ferromagnet. Cooper pair electrons that enter the ferromagnet must go into different spin-bands which have different potential energies leading to $|\uparrow\downarrow\rangle$ pairs gaining a center of mass momentum of Q = $k_F^{\uparrow} - k_F^{\downarrow}$, and $|\downarrow\uparrow\rangle$ pair gaining a center of mass momentum of -Q.

diffusion constant D. In this limit, the normal metal coherence length is

$$\xi_N = \sqrt{\frac{\hbar D}{2\pi k_B T}}. \tag{2.23}$$

For temperatures below 1 K, this length can be on the order of a micron and demonstrates how far the once-superconducting electrons can remain coherent. This induces superconducting-like properties in the normal metal corresponding to the Proximity Effect. Simultaneously, this leakage of Cooper pairs weakens the superconductivity at this boundary, reducing the critical temperature of the superconductor corresponding to the Inverse Proximity Effect.

In the case of a superconductor (S)/ Ferromagnet (F) interface, the exchange field and spin-band splitting cause drastically different outcomes for the electron transport across the boundary and coherence length in F. This topic has been treated extensively by Buzdin and Radović [15, 16, 17, 62, 63] but here we will follow the qualitative picture set forth by Demler, Arnold, and Beasley [22]. This is a hand-waving derivation but it gets across the key features of the S/F interface. In this picture, we will model the band structure in the ferromagnet as that of a normal metal with Zeeman splitting equal to twice the exchange energy of the ferromagnet, as shown in Figure 2.9.

In a conventional superconductor, the Cooper pairs form a spin singlet state given by

$$\Psi = \frac{1}{\sqrt{2}}(|\uparrow\downarrow\rangle - |\downarrow\uparrow\rangle) \tag{2.24}$$

where we are ignoring the spatial state of the Cooper pair in this simplified picture. Let us consider the $|\uparrow\downarrow\rangle$ component with its momenta normal to the interface being transported across the S/F interface. Because of the exchange field in F, the two electrons must enter different spin bands leading to the up-spin electron lowering its potential energy by the exchange energy $E_{ex}$ while the down-spin electron raises its potential energy by $E_{ex}$. To conserve total energy, the electrons must compensate for these changes by adjusting their kinetic energy. This leads to a non-zero center of mass momentum between the two electrons of

$$\hbar Q = \hbar(k_F^{\uparrow} - k_F^{\downarrow}). \tag{2.25}$$

If we assume that the bands are parabolic and that the Fermi velocity is the same in the two spin-bands since $E_{ex} \ll E_F$, this can be reduced to

$$Q = \frac{2E_{ex}}{\hbar v_F}. \tag{2.26}$$

Because of the antisymmetric nature of the electron pair wavefunction, we must consider this case together with the case in which the up and down spin electrons are exchanged, so a $|\uparrow\downarrow\rangle$ pair will have a center of mass momentum of Q while a $|\downarrow\uparrow\rangle$ pair will have a center of mass momentum of -Q. This can also be seen in Figure 2.9. Combining these pairs into the spin singlet configuration given in equation 2.24, we see that the wavefunction is modified by the exchange field in the ferromagnet to give

$$\Psi = \frac{1}{\sqrt{2}}(|\uparrow\downarrow\rangle\, e^{iQX/\hbar} - |\downarrow\uparrow\rangle\, e^{-iQX/\hbar}) \tag{2.27}$$

where X is the center of mass coordinate of the electron pair. Converting the exponentials into sine and cosine terms and grouping those components, we find

$$\Psi = \frac{1}{\sqrt{2}}\,(|\uparrow\downarrow\rangle - |\downarrow\uparrow\rangle)\, cos(Qx) + i\,(|\uparrow\downarrow\rangle + |\downarrow\uparrow\rangle)\, sin(Qx). \tag{2.28}$$

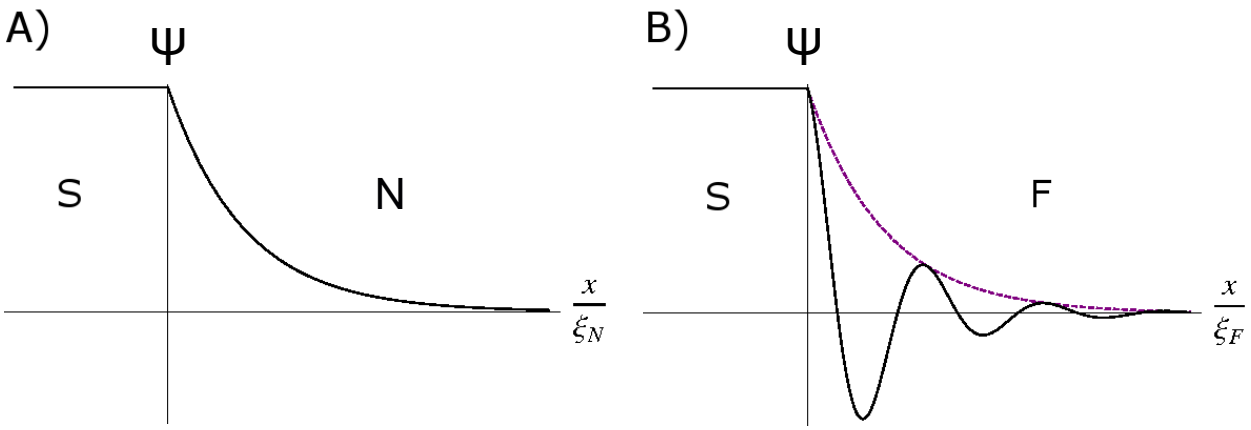


Figure 2.10 **S/N and S/F Pair Correlation Functions** S/N and S/F pair correlation functions highlighting the steep decay and oscillation of the function in the ferromagnetic case. The horizontal scales are not the same in A) and B) with a much longer length scale in A) than in B).

The sine term represents a spin triplet component and can be neglected in this case with one (or two) ferromagnetic layer(s) and S-wave superconductors. More generally, the pairs may not have normal incidence with the interface but their momenta can make an angle $\theta$ with respect to normal incidence. In this case, the pair momenta parallel to the interface must be conserved, so the normal momenta are modified to Q/cos$\theta$. After integrating over all angles, the total pair correlation amplitude

$$\psi \propto \frac{sin\frac{x}{\xi_F}}{\frac{x}{\xi_F}} \tag{2.29}$$

in the clean limit, with the coherence length

$$\xi_F = \frac{\hbar v_F}{2E_{ex}}. \tag{2.30}$$

In the dirty limit, the pair correlation function becomes

$$\psi \propto e^{\left(\frac{-x}{\xi_F}\right)} sin\left(\frac{x}{\xi_F}\right) \tag{2.31}$$

with a coherence length of

$$\xi_F = \sqrt{\frac{\hbar D}{E_{ex}}} \tag{2.32}$$

[14]. For elemental ferromagnets such as Fe, Ni, or Co, $E_{ex}$ is on the order of 1 eV [24, 25]. Hence, this coherence length in the ferromagnet is on the order of 1 nm - about 1000 times smaller than that of a normal metal at low temperature.

Figure 2.10 shows the comparison between the S/N and S/F pair correlation functions. In addition to having a much shorter decay length, the oscillations in the ferromagnetic case lead to several other interesting features of this system including oscillations in the critical temperature [55, 75] and density of states of S/F bilayers [47, 12] as a function of F-layer thickness. More relevant to the remainder of this thesis will be the oscillation of the critical current with ferromagnetic layer thickness in S/F/S Josephson junctions. This leads to the possibility of obtaining $\pi$ phase coupling between the two superconducting electrodes instead of the conventional 0 phase coupling. This effect results in a $\pi$ junction, which will be further detailed in the next section.

### 2.2.1 Phase of Ferromagnetic Josephson Junctions

A conventional Josephson junction will have a zero ground state phase difference between the two superconductors. The energy stored in a so-called 0-junction is given by

$$E_J(\phi) = \frac{\Phi_0 I_c}{2\pi}(1 - cos\phi) = E_{J0}(1 - cos\phi). \tag{2.33}$$

as was found in equation 2.9 and is clearly minimized when $\phi$ = 0. But, it was predicted that negative critical current could be obtained in the case of tunneling through an insulator with enough magnetic impurities [13]. This negative critical current leads to a ground state phase difference of $\phi = \pi$. This type of junction is called a $\pi$ junction, as mentioned in the preivous section. Buzdin showed that an S/F/S Josephson junction would be able to have either 0 or $\pi$ coupling depending on the thickness of the central ferromagnetic layer [15]. This is characterized by a decay and oscillation of the junction's critical current with F layer thickness. The thicknesses where the critical current drops to zero indicate the phase changing from 0 to $\pi$ or $\pi$ to 0 since only the absolute value of the critical current is measured in most experiments. This critical current

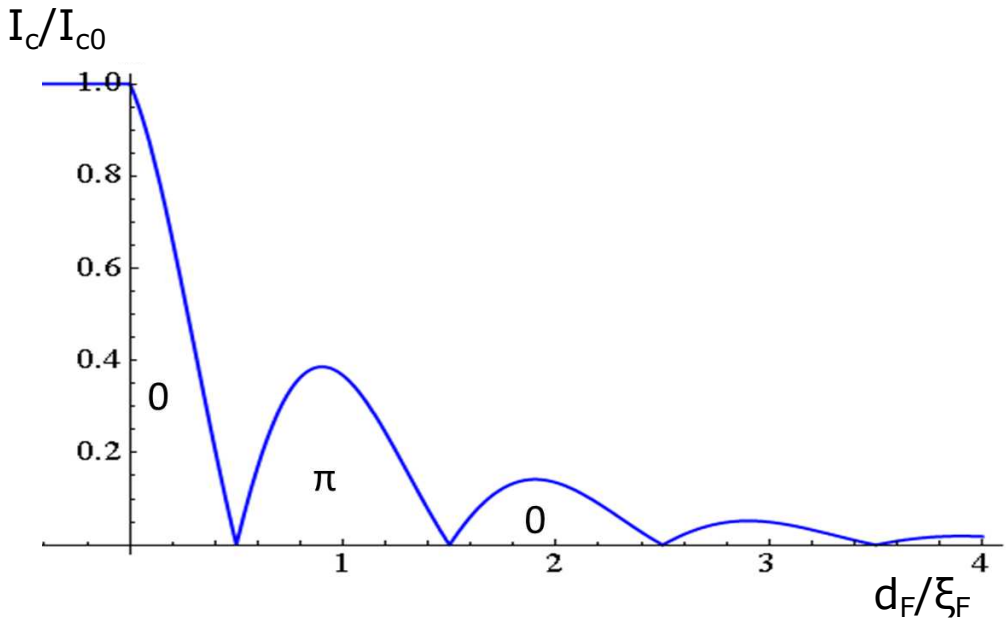


Figure 2.11 **Critical Current Oscillations in S/F/S Junction** The oscillation and decay of the pair correlation function into the ferromagnet manifests itself in similar behavior of the critical current. Regions where the current drops to zero indicates a phase transition of the ground state by $\pi$.

oscillation can be modeled by

$$I_c = I_{c0} e^{-d_F \xi_{F1}} * cos(d_F/\xi_{F2} - \theta) \tag{2.34}$$

where $\xi_{F1}$ and $\xi_{F2}$ are the length scales governing the decay and oscillation of the critical current respectively and $\theta$ is a phase shift [17]. This is plotted in Figure 2.11. These 0-$\pi$ phase oscillations has now been demonstrated by many groups, including my own, using both weak and strong ferromagnetic materials including PdNi, Ni, CuNi, Co, Fe, NiFe, NiFeMo, PdFe, and NiFeCo [68, 11, 46, 69, 58, 66, 70, 83, 67, 6, 1, 57, 30, 29].

With a single ferromagnetic layer, the ground state phase difference $\phi$ can be made either 0 or $\pi$ depending on the choice of ferromagnetic layer thickness. In order to have a junction whose phase can be controllably switched between 0 and $\pi$, a second ferromagnetic layer is required. In this case, the ground state phase difference $\phi$ will depend on the phase accumulation $\phi_{ac}$ of the transport electrons that travel through the junction according to equations 2.30 and 2.32. The phase accumulation through a single F layer $\phi_{ac} = d_F/\xi_F$, so the phase accumulated across $F_1$ is $\phi_1 =$

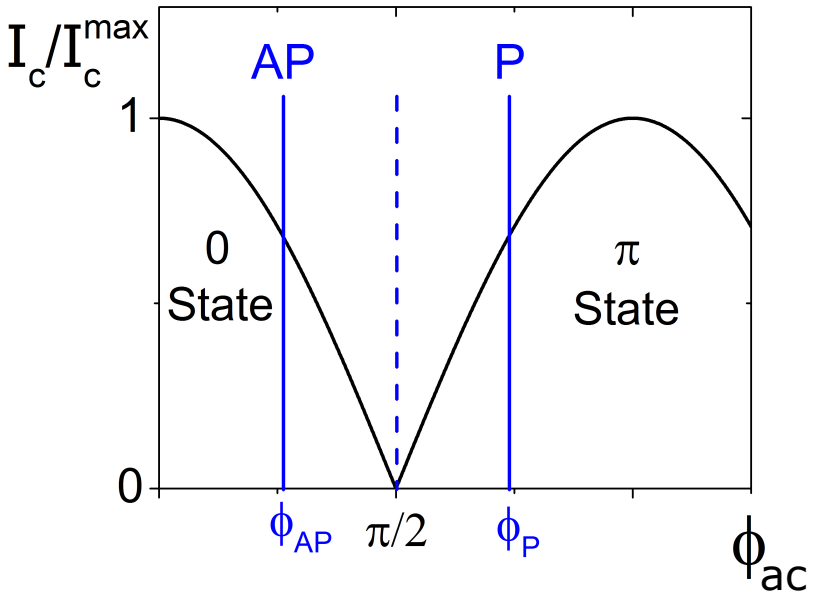


Figure 2.12 **Critical Current Oscillations in S/$F_1$/$F_2$/S Junction** The phase accumulation of the electrons across the junction determines whether the ground state phase difference of the superconductors will be 0 or $\pi$. When the two F layers have parallel magnetization directions, the total phase accumulation across the junction is the sum of the contribution from each layer. Similarly, if the two F layers are antiparallel, the total phase accumulation will be the difference of the contribution from each layer. So one scheme to produce a junction capable of switching it's ground state phase difference from 0 to $\pi$ would be to have one F layer at it's 0-$\pi$ transition thickness (indicated by the blue dotted line) and the other F layer thinner than it's 0-$\pi$ transition thickness. Then when the contributions add in the parallel (P) state, the junction will be in the $\pi$ state and when the contributions subtract in the antiparallel (AP) state, the junction will be in the 0 state.

$d_{F1}/\xi_{F1}$ and the phase accumulated across $F_2$ is $\phi_2 = d_{F2}/\xi_{F2}$. In the case that the magnetization directions of the two F layers are parallel (P), both layers will have the same minority and majority spin-bands for the entire transport process, so the total phase accumulation will be $\phi_P = \phi_1 + \phi_2$. Similarly, in the case that the two layers have magnetizations pointing antiparallel (AP) to each other, the spin-bands will interchange relative to each other, so the total phase accumulation will be $\phi_{AP} = \phi_1 - \phi_2$. If the F layer thicknesses are chosen correctly, this result can be used to create a junction that can be switched between the 0 and $\pi$ phase states. This is represented pictorially in Figure 2.12. One F layer is chosen to be at its 0-$\pi$ transition thickness, represented by the blue dashed line in the figure. The other layer is chosen to be thinner than its 0-$\pi$ transition

thickness. Then, when the two layers are parallel, the junction will be in the $\pi$ state and when the two layers are antiparallel, the junction will be in the 0 state. So, by changing the relative magnetization direction of the F layers in a Josephson junction with two F layers between the parallel and antiparallel configurations, the junction can be switched between the $\pi$ and 0 phase states [28].

## 2.3 DC SQUIDs

To measure the phase state of a junction, one must perform an interference experiment, e.g. by using a "dc SQUID." The Supercondcutcing QUantum Interference Device or SQUID was first invented in 1964 by Robert Jaklevic, John J. Lambe, James Mercereau, and Arnold Silver at Ford Research Labs [39]. Since then, it has found many uses, including for magnetic measurements and phase sensitive measurements, as in this work. A schematic configuration of a dc SQUID is shown in Figure 2.13. It consists of a superconducting loop with a Josephson junction incorporated into each arm. The ring is biased with a current I. The current in each arm of the loop can be characterized by $I_1 = I_{c1}\sin\phi_1$ and $I_2 = I_{c2}\sin\phi_2$ from the Josephson relations where $I_{c1/2}$ are the critical currents of the two junctions and $\phi_{1/2}$ are the phase differences across the junctions. The two junctions limit the total current that can flow through the ring. To determine the behavior of a dc SQUID, we will follow the framework of several references [9, 32, 18].

As we have seen, the Cooper pairs in the superconductor have a single wavefunction. In order for the wavefunction to have physical meaning, it must be single-valued, implying that the phase can only change by $2\pi$n over a closed loop. This implies that

$$2\pi n = \oint \nabla\theta \cdot d\boldsymbol{l} = \phi_{ab} + \phi_{bc} + \phi_{cd} + \phi_{da} \tag{2.35}$$

where the integral is divided up into four terms based on the phase difference across the paths from Figure 2.13 as denoted in the subscripts. Using the relationship between the phase $\phi$, the

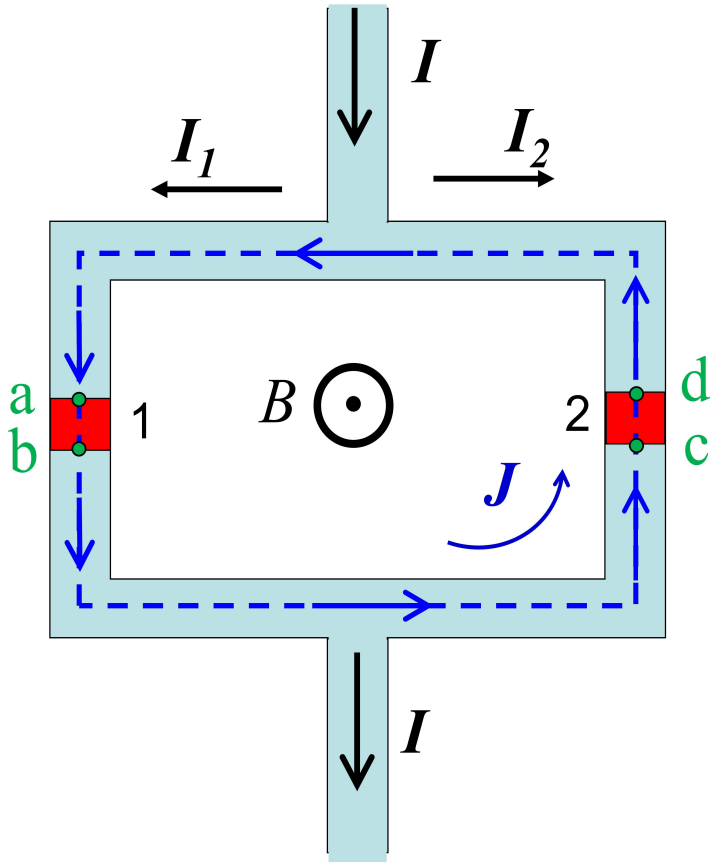


Figure 2.13 **Schematic view of a dc SQUID** Schematic view of a dc SQUID formed by two Josephson junctions in a superconducting loop driven by a current I. This current will split into $I_1$ and $I_2$, or can equivalently be thought of as a circulating current around the loop J. The blue dotted line indicates the closed contour integration path described in the text.

supercurrent densities $\boldsymbol{J_s}$, and the vector potential $\boldsymbol{A}$,

$$\nabla\phi = \frac{2\pi}{\Phi_0}\left(\boldsymbol{A} + \frac{1}{\mu_0\lambda_L^2}\boldsymbol{J_s}\right), \tag{2.36}$$

we find that

$$\phi_{ab} = \phi_1 + \frac{2\pi}{\Phi_0}\int_a^b \boldsymbol{A}\cdot dl \tag{2.37}$$

$$\phi_{bc} = \int_b^c \frac{2\pi}{\Phi_0}\left(\frac{1}{\mu_0\lambda_L^2}\boldsymbol{J_s} + \boldsymbol{A}\right)\cdot dl \tag{2.38}$$

$$\phi_{cd} = -\phi_2 + \frac{2\pi}{\Phi_0}\int_c^d \boldsymbol{A}\cdot dl \tag{2.39}$$

$$\phi_{da} = \int_d^a \frac{2\pi}{\Phi_0}\left(\frac{1}{\mu_0\lambda_L^2}\boldsymbol{J_s} + \boldsymbol{A}\right)\cdot dl \tag{2.40}$$

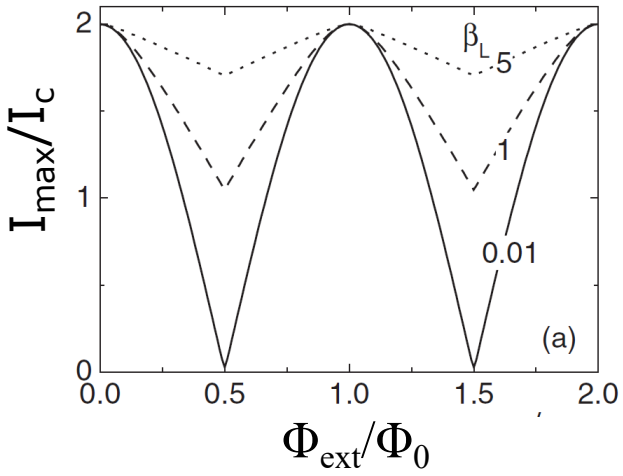


Figure 2.14 **Critical current vs applied flux for symmetric dc SQUID** Critical current vs applied flux for symmetric dc SQUID shown for three values of $\beta_L$. When $\beta_L \ll 1$, the SQUID critical current oscillates between $2I_c$ and 0. This modulation depth decreases as $\beta_L$ increases in value [18].

If the superconducting loop is wider than the London penetration depth, then the integration path can be taken deep inside the superconductor where $\boldsymbol{J_s}$ is zero, so those terms will not contribute to the final result. Additionally, the integral of the vector potential around a closed contour will equal the total flux $\Phi$ enclosed by the contour. Using this with equation 2.35, we find that

$$2\pi n = \phi_1 - \phi_2 + \frac{2\pi}{\Phi_0}\oint_C \boldsymbol{A}\cdot dl \tag{2.41}$$

or equivalently

$$\phi_2 - \phi_1 = \frac{2\pi\Phi}{\Phi_0} - 2\pi n \tag{2.42}$$

In the case of a superconducting loop with no Josephson junctions, this formalism shows that the flux enclosed by a superconducting loop in quantized. The total flux $\Phi$ in the loop is given as the sum of the geometric flux inside the loop from an external field $\Phi_{ext}$ and the contribution from the screening currents J as

$$\Phi = \Phi_{ext} + LJ \tag{2.43}$$

where L is the inductance of the loop and the screening current is given by

$$2J = I_1 - I_2 = I_{c1}sin\phi_1 - I_{c2}sin\phi_2. \tag{2.44}$$

and

$$\Phi_{ext} = BA_{eff} \tag{2.45}$$

$A_{eff}$ is the effective area of the loop, including the penetration depth of the superconductors. The total current flowing through the device is given by

$$I = I_1 + I_2 = I_{c1} sin\phi_1 + I_{c2} sin\phi_2. \tag{2.46}$$

Theorists like to eliminate one of the variables above by inserting equation 2.42 into equations 2.43 and 2.46 to get

$$I = 2I_c cos\left(\frac{\pi\Phi}{\Phi_0}\right) sin\left(\phi_1 + \frac{\pi\Phi}{\Phi_0}\right) \tag{2.47}$$

$$\Phi = \Phi_e - LI_c sin\left(\frac{\pi\Phi}{\Phi_0}\right) cos\left(\phi_1 + \frac{\pi\Phi}{\Phi_0}\right) \tag{2.48}$$

assuming that both junctions have the same critical current $I_c$. These two equations can be solved self-consistently to determine the behavior of the dc SQUID. The maximum current allowed through the SQUID for a given external flux can be found by maximizing 2.47 with respect to $\phi_1$ with the constraint of equation 2.48, which was first solved by de Bruyn Ouboter and de Waele [20].

Let us now introduce the screening parameter $\beta_L \equiv \frac{2LI_c}{\Phi_0}$ which is defined as the ratio between the magnetic flux generated by the maximum circulating current $I_c$ and half a flux quantum $\frac{\Phi_0}{2}$. In the case that $\beta_L \ll 1$, the flux produced by the screening currents is small compared to the flux quantum so the maximum current through the SQUID is found to be

$$I = 2I_c \left| cos\left(\frac{\pi\Phi}{\Phi_0}\right) \right| \tag{2.49}$$

from the method described above. So in this case of identical $I_c$ junctions and low $\beta_L$, the dc SQUID modulates between $2I_c$ and 0. As $\beta_L$ increases, there is a reduction in the modulation depth as shown in Figure 2.14.

### 2.3.1 Asymmetric dc SQUID

Since they will be experimentally measured in this work, we now turn our attention to the case of the asymmetric dc SQUID. We will specifically consider SQUIDs with asymmetries in the critical currents of the two Josephson junctions and in the inductance of each path. This is shown schematically in Figure 2.15. In this case, the flux induced by the shielding current J is

$$LJ = L_1 I_1 - L_2 I_2 = L_1 I_1 sin\phi_1 - L_2 I_2 sin\phi_2 \tag{2.50}$$

where the total inductance of the loop L = $L_1$ + $L_2$ [9, 27]. From equation 2.42 and using equations 2.50 and 2.43 we find that

$$2\pi n = \phi_1 - \phi_2 + 2\pi\frac{\Phi_{ext}}{\Phi_0} + 2\pi\frac{L_1 I_{c1}}{\Phi_0} sin\phi_1 - 2\pi\frac{L_2 I_{c2}}{\Phi_0} sin\phi_2. \tag{2.51}$$

Using the parameters $\beta_1 = 2\pi\frac{L_1 I_{c1}}{\Phi_0}$, $\beta_2 = 2\pi\frac{L_2 I_{c2}}{\Phi_0}$, and $\phi_{ext} = \frac{\Phi_{ext}}{\Phi_0}$, the last equation can be re-written as

$$2\pi n = \phi_1 - \phi_2 + 2\pi\phi_{ext} + \beta_1 sin\phi_1 - \beta_2 sin\phi_2. \tag{2.52}$$

The current flowing through the SQUID is the same as equation 2.46, rewritten here for convenience

$$I = I_{c1} sin\phi_1 + I_{c2} sin\phi_2. \tag{2.53}$$

These two equations form a non-linear set in variables $\phi_1$ and $\phi_2$ with $\phi_{ext}$ and I as external parameters. We want to know the critical current of the loop as a function of the external flux $\phi_{ext}$ so we need to find the maximum value of I($\phi_1$, $\phi_2$) with $\phi_1$ and $\phi_2$ subject to the constraint of equation 2.52. Several methods have been proposed to solve this problem, but we will follow the method of Lagrange multipliers used by Tsang and Van Duzer [49, 80]. So, we introduce the Lagrange multiplier $\lambda$ and form the new function

$$I' = I_1 sin\phi_1 + I_2 sin\phi_2 + \lambda(\phi_1 - \phi_2 + 2\pi\phi_{ext} + \beta_1 sin\phi_1 - \beta_2 sin\phi_2 - 2\pi n). \tag{2.54}$$

Then, finding the critical points of I$'$ as a function of $\phi_1$, $\phi_2$, and $\lambda$ and eliminating $\lambda$ gives these two equations:

$$\phi_{ext} = \frac{1}{2\pi}(\phi_{c2} - \phi_{c1} + \beta_2 sin\phi_{c2} - \beta_1 sin\phi_{c1}) \tag{2.55}$$

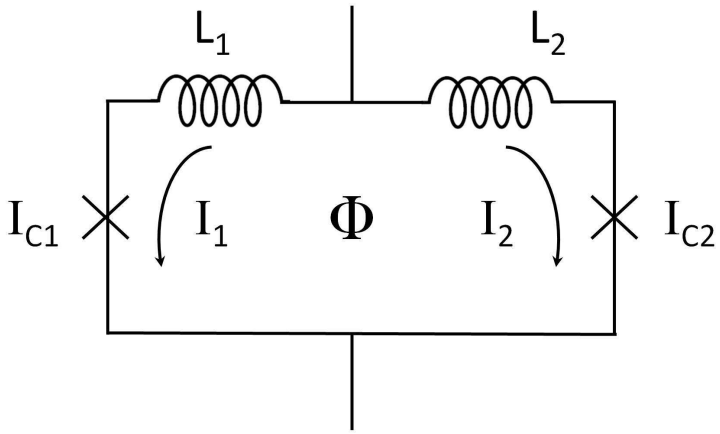


Figure 2.15 **Schematic of an Asymmetric SQUID** In this case, the critical currents of the two junctions and the inductances of each path can have different values.

$$\phi_{c2} = cos^{-1} \frac{-1}{I_2/(I_1 cos\phi_{c1}) + \beta_T} \tag{2.56}$$

where the subscript 'c' added to $\phi_1$ and $\phi_2$ indicate the phase values when the critical current of the device is $I_c$ (the maximized value of $I'$) and the parameter $\beta_T = \beta_2 + \beta_1 \left(\frac{I_2}{I_1}\right)$. Now, we can find all the pairs $\phi_{c1}$, $\phi_{c2}$ that satisfy equation 2.56, which will form a locus in the $\phi_1$, $\phi_2$ plane. Subsequently, each pair on that locus can be used in equation 2.53 to find I and in equation 2.55 to find $\phi_{ext}$. These can be used to find the $I_c(\phi_{ext})$ dependence for all values of $\phi_{ext}$. Once these relationships are known, the individual critical currents of the junctions can also be easily calculated.

The $I_c(\Phi_{ext})$ curve for the general case of $I_1 \neq I_2$ and $L_1 \neq L_2$ is shown in Figure 2.16. In this case, the curves take on an asymmetric sawtooth shape with the peaks of the positive and negative critical current polarities shifted off of zero along the flux axis by the same amount but in opposite directions. At the peak positions, the current through each junction is the critical current so $I_1 = I_{c1}$ and $I_2 = I_{c2}$. Comparing with equation 2.50, we find that $\phi_1 = \phi_2 = \pi/2$. Those currents induce a flux through the SQUID loop, $\Phi_{int} = LJ = L_1 I_{c1} - L_2 I_{c2}$, satisfying equation 2.42. That must be balanced by the externally applied flux, so the peak in the critical current vs flux curve occurs at a flux of $\Phi_{peak} = -\Phi_{int} = L_2 I_{c2} - L_1 I_{c1}$. This can be re-arranged as $1/2\beta_L(\alpha_I + \alpha_L)$ where $\alpha_I$ and

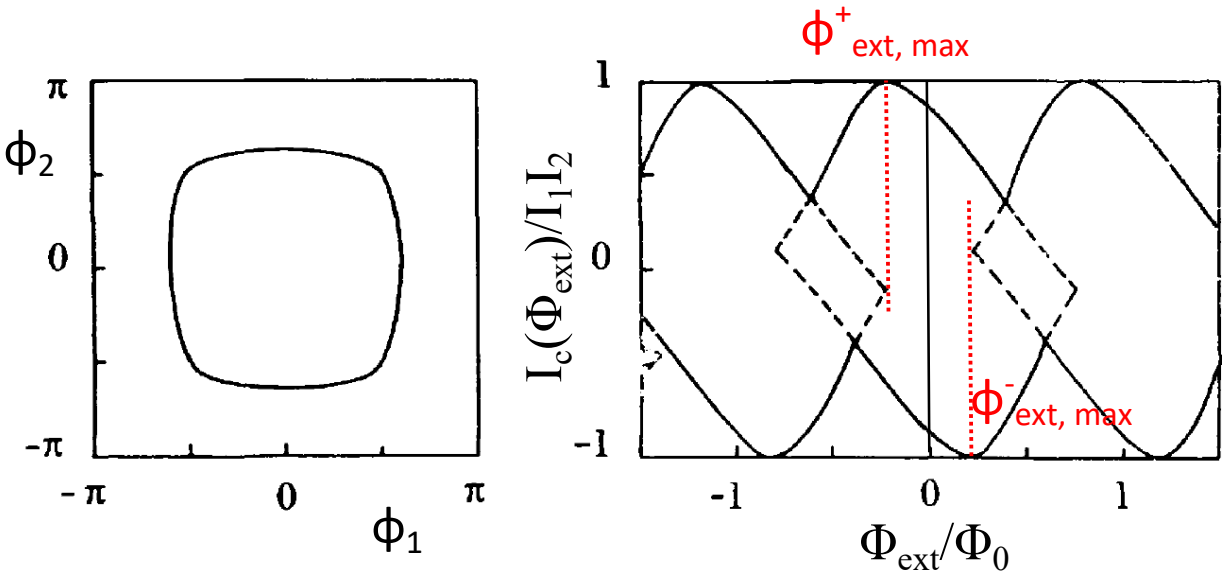


Figure 2.16 **Theoretical Magnetic Flux Dependence of the Critical Current of an Asymmetric SQUID** The device considered here has both Josephson junction critical current and inductance asymmetries. The left-hand plot shows the locus of $\phi_1$,$\phi_2$ solutions described in the text and the right-hand plot shows the resulting oscillation of the critical current of the device with the applied external flux. The values of the characteristic parameters used are $\beta_1 = 0.5\pi$, $\beta_2 = 0.1\pi$, $\beta_T = 0.5\pi$ and $I_2 = 0.8I_1$ [9].

$\alpha_L$ characterize the asymmetry of the junction critical currents and inductance as

$$\alpha_I = \frac{I_{c2} - I_{c1}}{I_{c1} + I_{c2}} \tag{2.57}$$

$$\alpha_L = \frac{L_2 - L_1}{L_1 + L_2}. \tag{2.58}$$

This means that the difference between the peak locations of the positive and negative critical current branches $\Delta\Phi$ is given by

$$\Delta\Phi = \beta_L(\alpha_I + \alpha_L). \tag{2.59}$$

Calculations for various values of $\alpha_I$ and $\alpha_L$ show that with increasing $\alpha_I$ there is a reduction in the modulation depth of the critical current. $\alpha_L$ has no effect on the modulation depth but increases the skewness of the curves. This framework will be used to analyze and and fit data collected from asymmetric SQUID devices in Chapter 8.

# CHAPTER 3

# SAMPLE FABRICATION

Sample fabrication is an involved process with many steps. In this chapter, I will detail the main equipment used in sample fabrication and the steps for the fabrication of sub-micron Josephson junctions.

## 3.1 Fabrication Equipment

### 3.1.1 Sputtering System

All deposition of superconducting, magnetic, and normal metal materials is done by sputtering in this work. The sputtering system can hold four 2.25-inch diameter triode sputtering guns, three 1-inch diameter magnetron sputtering guns, and an ion mill. Each gun is topped with a foil-wrapped

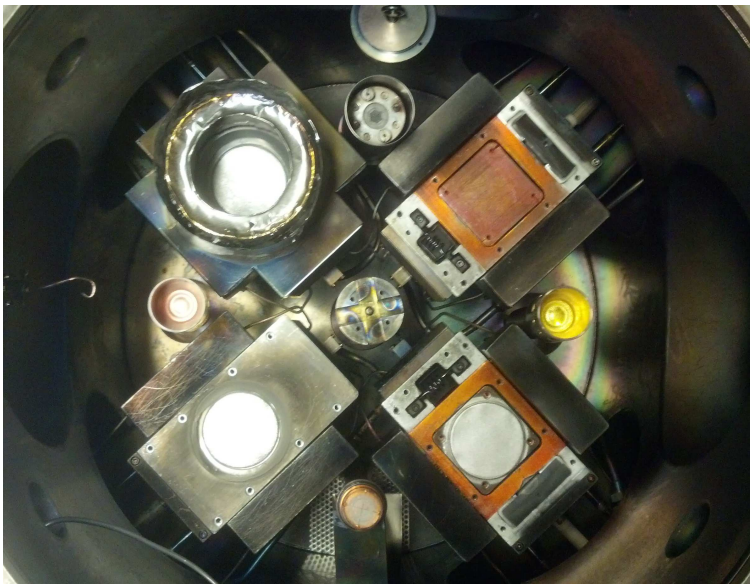

Figure 3.1 **Top-down view of the sputtering system** Shown are the four triode sputtering guns, three magnetron sputtering guns, ion-mill, and wobble stick on the far left. The large guns are shown at various stages of installation. Starting in the northeast corner and rotating clockwise, the four large guns are shown empty, with the target installed, with the gun housing installed, and finally with the magnetic cover plate and chimney installed.

chimney to avoid cross contamination. A top-down view of the sputtering chamber can be seen in Figure 3.1. Each gun will sputter a different material from the installed target. Up to 16 samples are held on the sample positioning and masking (SPAMA) plate about four inches above the gun targets. The samples are separated from the guns by the shutter plate, which has four equally spaced openings that will either open the samples to the large or small diameter guns. Both the SPAMA plate and shutter plate are automatically controlled by Labview computer software.

The deposition process occurs through momentum transfer between an argon plasma and the target material. I will now describe the function of the triode gun. To start, argon gas is flowed into the system. The guns produce a uniform magnetic field from a pair of magnets and an electric field between the gun's cathode and anode. The cathode is created by a hot filament that emits electrons. The electric and magnetic fields intersect above the target and create a plasma of ionized argon and electrons. The target is biased with a negative voltage, so this plasma interacts with the target material and knocks off atoms which travel up towards the sample substrate. The deposition rate of the material can be measured with a film thickness monitor (FTM) and is typically very stable throughout a sputtering run if the target voltage and current are kept constant. The desired sample deposition stack is entered into a sequence file by the user and the Labview software will calculate how long the sample must remain over each gun using the measured deposition rate. Then the sample will be fabricated through automatic movement of the SPAMA and shutter plates.

Up to 16 chips can be loaded into the sputtering chamber in each run. To protect the other chips when one is being sputtered, each chip is loaded into a holder with a rotating window. There are prongs on the bottom of this window that can be hooked with the wobble stick and rotated to reveal a sample or shut it away. Proper alignment of this window is needed to ensure the whole chip area will see the sputtered material if material deposition is desired, and that no additional material will be deposited when subsequent chips are being sputtered.

The tables below shows the gun settings for each material used in this study.

| Material | Voltage (V) | Current (A) | Rate (Å/s) |
|---|---|---|---|
| Nb | 600 | 0.60 | 4.1 - 5.4 |
| Al | 400 | 0.50 | 1.9 - 2.4 |
| Ni | 350 | 0.30 | 1.7 - 1.9 |
| NiFe | 450-500 | 0.45 - 0.50 | 3.2 - 4.6 |
| NiFeCo | 470-500 | 0.47 - 0.50 | 3.7 - 4.3 |
| NiFeMo | 500 | 0.50 | 3.9 - 4.7 |
| CoFeB | 550 | 0.55 | 4.1 - 4.5 |

Table 3.1 **Target voltage and filament current settings for large gun sputtered materials** The NiFe voltage and current values started at 500 V and 0.50 A and were gradually turned down as the group started using thinner and thinner NiFe layers. Material deposition rates vary with applied current/voltage, chamber pressure, and target thickness.

| Material | Power (W) | Rate (Å/s) |
|---|---|---|
| Au | 17 - 20 | 4.5 - 5.5 |
| Cu | 19 - 30 | 2.6 - 4.5 |
| Ru | 18 | 0.9 - 1.3 |
| FeMn | 37 - 44 | 2.3 - 2.7 |

Table 3.2 **Power settings for small gun sputtered materials** Power values are selected to obtain the desired deposition rate based on the amount of material that will be deposited. Material deposition rates vary with applied current/voltage, chamber pressure, and target thickness.

### 3.1.2 Electron-Beam Lithographer

Electron-beam lithography was used to pattern the submicron junctions. Much of this work was done using the JEOL 840 Scanning Electron Microscope (SEM). Midway through 2016, we were fortunate to be able to upgrade that piece of equipment to the Hitachi SU5000 Schottky Field-Emission SEM with Electron-beam Lithography (EBL) capabilities. Since this new system will be the only one used by future students, I will detail it's operation here and attempt to avoid complaining about how much more user effort was required to use the JEOL.

Chips to be patterned with EBL must first be coated with a suitable resist. We use ma-N 2401 which is a negative-tone resist from Micro Resist Technology. After spinning and baking, about a 100 nm film rests on top of the chip. This resist is rated for pattern resolutions below 50 nm. After development, we want a pillar of resist of the desired junction size to remain. Since the ma-N is a negative resist, this means that the resist that is exposed to the electron beam will harden and

remain on the chip after development, so we want to expose only the pillar area. The write patterns are drawn using designCAD software and converted to patterns that the SEM can recognize using the Nanometer Pattern Generation System (NPGS) developed by Dr. Joe Nabity. It is convenient to be able to draw your own patterns in the computer software so you can try out many different junction sizes and shapes on a project-by-project basis without having to buy a new mask every time, as is the case for photolithography. Based on dose tests, our patterns are written with an area dose of 550 $\mu C/cm^2$.

The electron beam is created using a field emission gun of the Schottky type. The emitter tip is made of tungsten coated with zirconium oxide. The purpose of this oxide is to reduce the work function of the cathode. The Schottky effect, or field-enhanced thermionic emission is a process in electron emission devices where the emitter is biased negatively, creating an electric field at the surface of the emitter. This field reduces the electron barrier and increases the emission current of the emitter. This process is maintained in the head of the SEM under high vacuum ( $7 * 10^{-10}$ Torr) even when the system is not in use to ensure a stable beam current.

After a series of magnetic lenses focus and guide the beam down through the column, the beam arrives at the sample surface. The electrons interact with the resist to harden the areas that are exposed so that they will remain after development. The sample chamber has a variable pressure option, but since our samples are conducting, the high vacuum option is used to enhance the resolution.

### 3.1.3 Ion-Mill and Thermal Evaporation

Ion milling is a subtractive process used to pattern the bottom lead of the sample into a series of junctions. The schematic layout can be seen in figure 3.2. In general, ionized argon gas is accelerated towards the sample. When the gas collides with the sample, it chips away at the sample surface, removing a relatively constant amount of material each second. The chamber contains a 3-inch Commonwealth Scientific Argon Ion beam source, a gold sputtering gun, SiO for thermal evaporation, a sample plate containing slots for five samples and the FTM, and a separation plate

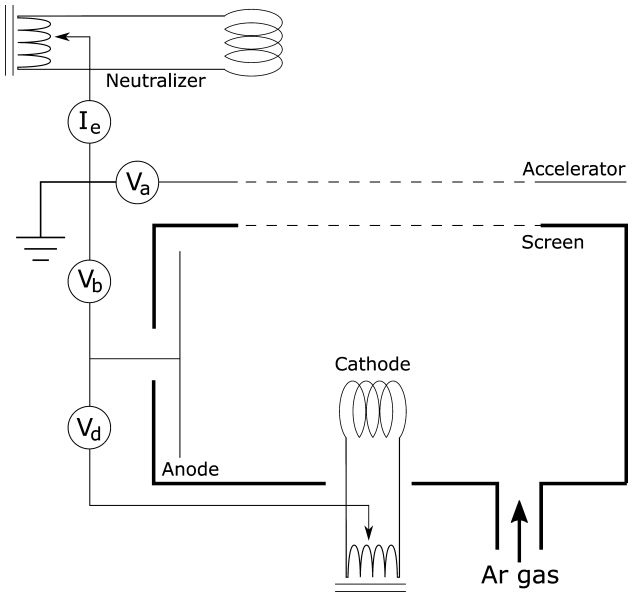


Figure 3.2 **Schematic view of the Ion Mill** The dashed lines represent the ion-mill grid while the solid bold lines represent the ion-mill housing. The accelerating, beam, and discharge voltages are labeled $V_a, V_b$, and $V_d$ respectively, and the neutralizer current is labeled $I_e$.

with one opening between the samples and the deposition sources.

After loading the samples into the chamber and waiting for the excess water and gas to pump out, Argon gas is introduced into the chamber. Then, a voltage difference is applied between the cathode and anode of 39 V. Also, a current is applied to the cathode filament to generate an electron beam and ionize the argon gas. Above the cathode and anode are two carbon grids. The first grid is a screen that collimates the beam and acts to avoid direct collisions between the ionized gas and the second grid. The second grid is the accelerator. While most of the acceleration comes from the +300 V beam voltage, the accelerator grid receives a negative voltage of about -30 V to enhance the acceleration of the positively charged argon ions up towards the sample. Last, the beam passes by the neutralizer filament which adds electrons to the beam and acts to reduce the repulsion of the like-charged argon ions. Typical ion mill settings can be seen in Table 3.3 below.

These ions then collide with the sample surface. These collisions cause atoms from the sample surface to be knocked off and deposited elsewhere in the chamber. The rate of material removal is measured with an FTM that is coated in gold. The milling rates of all other materials relative to the

| | Figure Label | Small Chamber Ion Mill | Large Chamber Ion Mill |
|---|---|---|---|
| Beam Voltage (V) | $V_b$ | 300 | 175 |
| Beam Current (mA) | $I_b$ | $\sim$ 9.0 | $\sim$ 1.0 |
| Discharge Voltage (V) | $V_d$ | 39 | 40 |
| Accelerator Voltage (V) | $V_a$ | -30 | -50 |
| Neutralizer Current (mA) | $I_e$ | $\sim$ 0.5 higher than $I_e$ | $\sim$0.5 higher than $I_e$ |

Table 3.3 **Ion mill settings for the small and large milling chambers** The beam current values shown are starting values. They will drift upwards during the milling process but the milling rate remains constant if they are not adjusted.

gold milling rate is called the k factor. These multiplicative factors are measured for each material by milling each material and measuring the milled depth in the atomic force microscope. The gold milling rate can only be measured before and after a sample is milled, but luckily, this rate is quite stable through the milling of all samples in the chamber. These values are used to calculate the milling time needed for each sample, then the user must manually open and close the separation plate with the sample positioned above the ion mill for the correct amount of time. This process mills through the desired amount of material to define the size and shape of the junction which will be the same as the size and shape of the electron-beam resist above.

Following ion-milling, the sample is coated in SiO *in situ* to electrically isolate the junction. This is done by thermal evaporation. The SiO granules are placed in one side of a baffle boat in the ion-milling chamber. The boat is heated by the application of a current to the resistive boat, which heats the SiO. When the SiO is sufficiently heated, it will begin to evaporate SiO molecules. These will be released from the other side of the boat, where they will travel up towards the sample and adhere to the sample surface. A magnetic arm holds the sample above the evaporating SiO, which can be spun to obtain a more uniform material distribution. The FTM in the chamber is used to determine the SiO deposition rate.

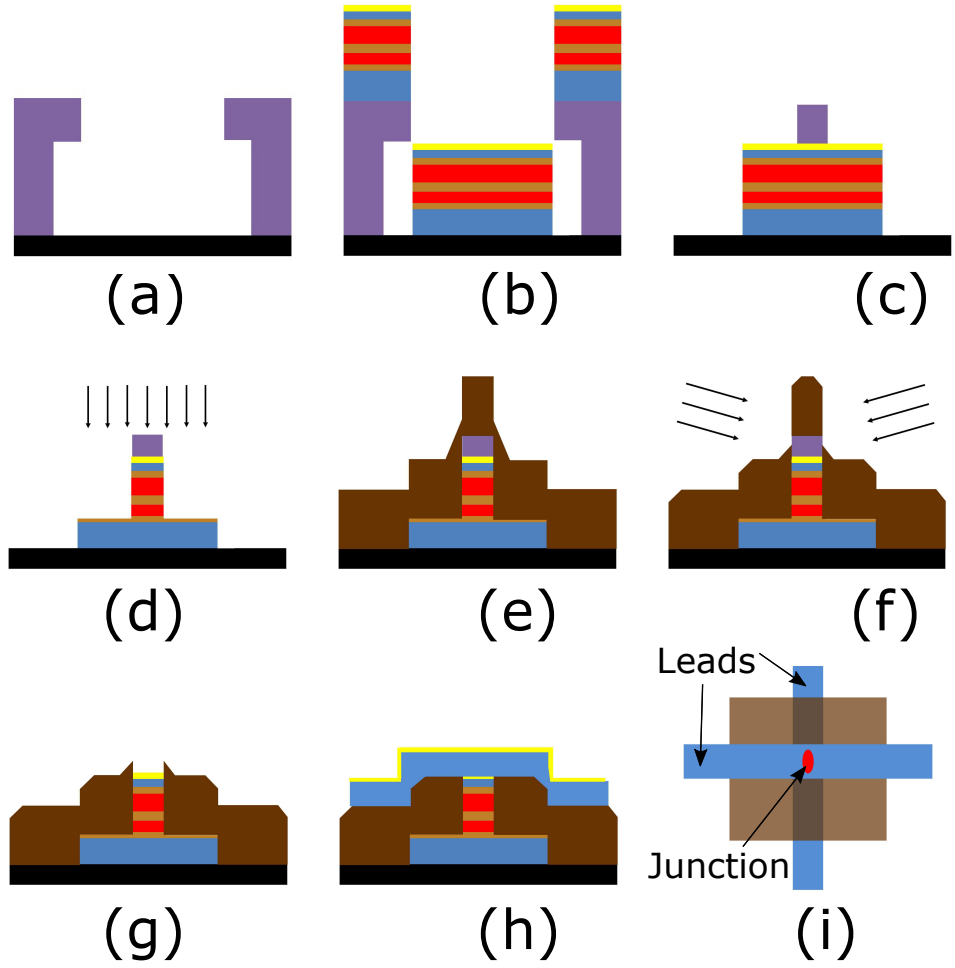


Figure 3.3 **Schematic drawing of the sample fabrication process** The vertical scale is greatly magnified and relative material thicknesses are altered to better show the process steps. Color code: purple = resist, blue = superconductor, red = ferromagnetic material, orange = normal metal,yellow = gold, brown = SiO, arrows show ion-milling direction a) Bottom lead photolithography on cleaned Si substrate b) Material deposition through sputtering c) Bottom lead lift-off and electron-beam lithography for junction definition d) Vertical ion-milling to define pillar dimensions e) SiO thermal evapotation to electrically isolate the junction f) Horizontal side ion-mill to break through SiO side-wall build-up to reveal resist g) Electron-beam resist lift-off h) Top lead photolithography and top lead deposition through sputtering i) Top down view of final junction

## 3.2 Fabrication Process

A cartoon of the entire process flow can be seen in figure 3.3. Starting with a blank silicon chip, photolithography defines the bottom lead pattern which is filled with sputtered material. Josephson junctions are patterned with electron-beam lithography, defined with ion milling, and electrically isolated with SiO thermal evaporation. After lift-off, a second round of photolithography defines the top leads which are also sputter deposited. This process has seen several variations in the past few years and I will make note of past variants for completeness.

### 3.2.1 Bottom Lead Photolithography

Fabrication is performed on half-inch square silicon chips with native oxide. These chips were diced from a wafer while protected with photoresist, so the first step is to clean these substrates. It is important to start with a clean substrate surface to ensure good adhesion between the substrate and subsequent sputtered materials. To clean the chips, place each chip in a test tube with acetone, and the test tube in a beaker of water on a hot-plate set to 100°C for about five minutes. Then, move beaker to the ultrasonic for 5-10 minutes. After this, replace the acetone in the test-tubes with IPA and wait two minutes. Then, rinse the chip with IPA over the waste beaker and blow dry with the nitrogen blower.

Now take your clean chips over to the spin-coater. For ease of clean-up, wrap the bottom of the coater in aluminum foil. Choose an appropriate sized chuck based on your sample size. The chuck should be slightly smaller than the substrate chip. After you make sure the chuck and pipette are clean, apply four to five drops of S1813 photoresist to the center of the chip and spin for 50 seconds at 5,000 RPM. Then, bake the chips on the vacuum hot-plate on the PR-VAC program (110°C for 120 seconds). We used to use this program for only 60 seconds but increased the time as the heating surface became less effective with age and use.

S1813 is a positive resist, meaning when it is exposed to UV light, the parts that are exposed become weakened and will be removed from the chip during development. So, the photomasks

we design are primarily chrome with openings that define the bottom leads of the pattern. The bottom lead is typically a long wire from which the pillars will be defined as well as alignment marks to properly line up subsequent masks. Alignment of the chip with the bottom-lead mask does not need to be precise. Once the chip is roughly aligned with the mask, bring the chip into contact with the mask and expose for ten seconds. For small scale features, you want the contact to be as close as possible. For single pillars the "smalloverlapGMR" mask is primarily used and the "BIRGE SQUID TRIPLET" mask is used for asymmetric SQUID samples. These masks are four-inch square and were designed at MSU for measurement at MSU, meaning they have large pads for pressed In wire connections. This process is slightly different for the symmetric SQUID samples and will be discussed in the next subsection.

After exposure, the chips are soaked in chlorobenzene for five minutes, agitating the sample for the first 10 seconds and the last 30 seconds of this time period. This creates an artificial bi-layer where the top of the resist is harder to remove then the bottom. After the chip is developed in 352 developer for 45 seconds and rinsed in DI water for 30 seconds, the pattern created will have an undercut profile, as shown in part (a) of figure 3.3. This profile aids in separating the deposited material from the resist for an easier lift-off process. Always check each sample in the microscope after development to ensure that all mask features were properly copied to the chip.

#### 3.2.1.1 Small Feature Size Variant

When MSU fabricates chips for measurement at Northrop Grumman, there are several variants to the above outlined photolithography process to ensure that the small features are properly replicated on the chip. This technique is also used on MSU chips with many small features or long, straight, thin lines that don't develop properly in the above outlined process. The NGC mask design has a two-by-two array of half-centimeter NGC chips that fit on our standard half inch square substrate with a small amount of extra space on the edges for handling the chip with tweezers. The contact pads are all located around the edges of the chip so it is important not to damage those regions. The four NGC chips have similar layouts with an identifying mark in the center to break

the symmetry.

The substrate cleaning process is the same as above. Next place the chips in the oven set to 100°C for at least 10 minutes to remove any water residue from the chip surface. In this time, cut out a circle the same size as the largest sized wafer chuck from the blue semiconductor processing tape. Place the tape sticky-side up on the largest wafer chuck and center the baked chip on the chuck, lightly tapping down the corners of the chip with the tweezers. When the chuck spins, the vacuum will hold down the tape and the sticky side of the tape will hold on the chip.

First, use the pipette to load up the chip with an unreasonable amount of HMSD primer. The primer should completely cover the chip and spill down over the entire perimeter of the chip making a large mound. By using this process, the surface tension of the primer is broken and the edge-bead effect, where the material builds up around the edges of the chip, is highly reduced. Additionally, the HMDS primer increases the adhesion of the subsequent S1813 resist to the chip. This is important for patterns with stand-alone long, thin lines which can otherwise detach from the chip during development or become wavy or broken. Then, spin the chip at 5,000 RPM for 50 seconds. Immediately after, cover the chip with S1813 photoresist using the same surface tension reducing method and spin again at 5,000 RPM for 50 seconds. Now, carefully peel the chip off of the semiconductor tape and bake it on the programmable hot-plate for 2 minutes at 110°C (also the PR-VAC program).

The 5-inch "Anacostia" mask is used for symmetric SQUIDs. The chip is aligned in the mask-aligner the same way as above, but because the edge-bead is much smaller, it should be possible to make better contact between the chip and the mask. Once contact has been made, expose the chip for 6 seconds and develop in cholorobenzene for 5 minutes (same as above), then 352 developer for 35 seconds, followed by a rinse in DI water for 20 seconds. Carefully check the chip in the microscope to make sure that all the pads and wires developed properly. Since there are so many small, important features, it is helpful to have the mask coated in Teflon by the manufacturer to reduce residue build-up which can cause pattern distortion.

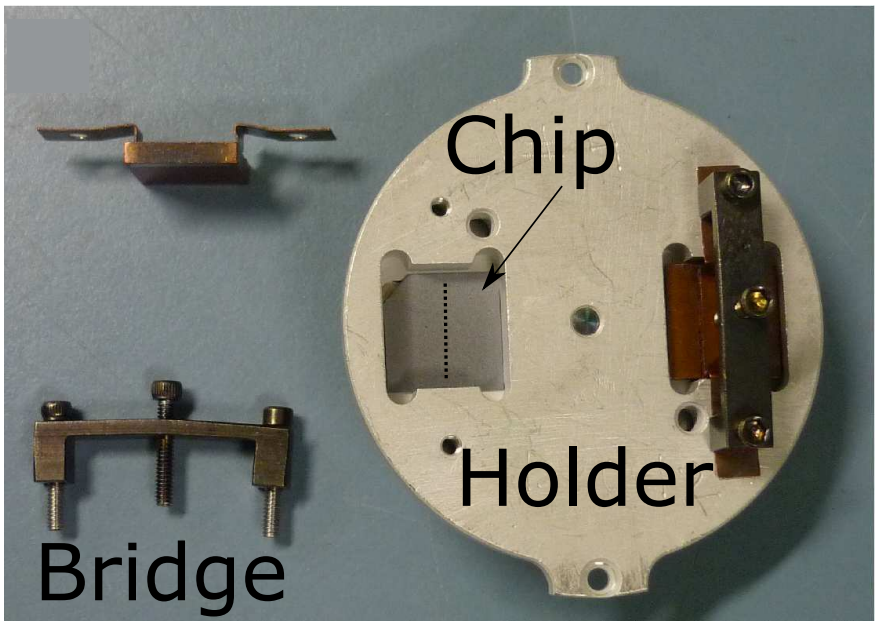


Figure 3.4 **Picture of Sputtering System Sample Holder** The sample chip is placed face-down into the holder and is held in place with a heat sink and bridge with screws. The dashed black line through the center of the chip represents the orientation of the bottom leads on the front side of the chip. They are aligned parallel to the bridge orientation.

### 3.2.2 Bottom Lead Material Deposition

Once the chips are developed, they are ready to be loaded into the sputtering system for material deposition. To prepare the sputtering system, both the sample holders and gun parts must be properly cleaned and assembled. Clean the sample holders and cover plates in a 3:1 mixture of Nitric Acid and DI water for 30-60 minutes. Leaving the parts in this mixture longer than 60 minutes can damage the screw holes in the holder so avoid doing that. Rinse the parts in DI water and scrub each piece with a wire brush to remove any metal depositions from previous sputtering runs. Put the parts in the ultrasonic bath in a glass beaker of acetone, then ethanol, then DI water for 5 minutes each. After this, lay the parts out on a large kimwipe and blow them dry with the heat gun set between 900 and 950°F until the parts are hot and the paper underneath them begins to toast. Allow the parts to cool and bring them to the clean room to load the samples.

Load the samples into the holders with the long axis of the bottom leads oriented parallel to the bridge that holds the heat sink against the sample as shown in Figure 3.4. This reduces non-

uniformity in sputtered material from rotating onto or away from active sputter guns. If in-plane magnetic material is being deposited, it is important to grow the material in a magnetic field by placing a half-inch square magnet directly behind the sample substrate. Typically, the magnetic field is oriented parallel to the long axis of the bottom leads. Then, cover the sample with a copper heat-sink and affix it with a bridge and screws. Do not over-tighten the center screw that pushes down on the sample as it can cause the sample to crack. Up to sixteen samples in eight sample holders can be loaded into the sputtering system each run.

The sputtering system can support the use of up to four 2.25-inch-diameter triode sputtering guns and up to three 1-inch-diameter magnetron sputtering guns, and an ion mill. For proper use, scrape all the gun parts and target bases with a razor blade to remove any metal flakes that can cause electrical shorts. Their slots in the chamber must be vacuumed out and blown with nitrogen gas for the same reason. Once the large guns have been installed, it can save a lot of heartache to check the resistance between the target and base to make sure they are not shorting. Lastly, install the chimneys and shutter plate into the system. They must be wrapped in aluminum foil that is changed between runs to avoid contamination.

Once all the guns and samples are in the system, pump down below $8x10^{-6}$ Torr then test the guns. If the testing goes well, close the gate valve so that it is only open 10 turns, then set it to bake for eight hours with the small gun water running on a low setting. After the system has cooled back down to room temperature, open the gate valve completely and wait until the pressure has decreased to about $3x10^{-8}$ Torr before starting the sputtering run.

When ready to begin the run, cool down the system so that the substrate plate remains around -30 to -20°C. Turn on all the guns and wait for a stable plasma. Each gun must be run at a specific current and voltage setting based on the material. A list of materials used in this thesis work along with their run values can be found in Tables 3.1 and 3.2. Once set, the deposition rates of each gun are measured with the FTM. From there, a run file is made which details the materials and deposition amounts desired by the user. The automated system will then move the sample through the sequence to make the proper material stack. Josephson junction bottom leads include

deposition of a base Nb electrode, all magnetic layers with normal metal spacers, and a cap of Nb and Au. Depositing all these materials *in situ* ensures clean interfaces between the layers. Several base superconducting electrodes and spacer layers have been used in this group over the past few years. The various options that we tried out are detailed in Chapter 5. The current "best" stack uses a base electrode of $[Nb(25)/Al(2.4)]_3/Nb(20)$, a thin spacer layer of Cu(2) and a thick spacer layer of Cu(4). We also use Nb(5) for the capping layer while previously Nb(20) was used so that this cap would be superconducting on its own instead of only by proximity. Part (b) of Figure 3.3 shows a cross section of the chip after material deposition.

After sputtering is completed, bring the samples in their holders into the clean room for lift-off of the bottom-lead photolithography. This is done by putting each chip in a labeled test tube of acetone, each placed in a beaker of water on a hot plate that is set to 100°C. Wait until the material deposited over the resist regions begins to wrinkle and start to peel up. This should take about five to ten minutes. Then place the beaker into the ultrasonic until all the excess material and resist has been removed from the sample surface, revealing just the material in the bottom lead pattern. This should take several minutes or less. Rinse each chip in acetone, IPA, and DI water, being careful not to allow the lifted off material to redeposit onto the sample surface. Finally blow dry with the nitrogen blower and inspect in the microscope to ensure that all the bottom lead features are present on the chip.

#### 3.2.2.1 Tips and Tricks

After thousands of sputtering runs, a user sees many failure mechanisms and learns a few tips and tricks in troubleshooting. A common issue is failure for a sequence file to open in the sputtering program. This is more frequent when creating the sequence using the set-up program since, if not entered perfectly on the first try, many hidden errors can occur. These errors include hidden spaces both at the start and end of a command line, extra carriage returns, and merged command lines. If writing the sequence file from scratch or modifying an existing file, be sure to check for typos and proper capitalization of commands. Even if the sequence file is written properly, attempting

to load the sequence file will give the same unhelpful error message if there are not deposition rates measured for all the materials used in the sequence file. The program calculates the sequence timing upon opening the file and has obvious issue calculating a deposition time for a material with a rate of 0, which is the default value upon opening the program.

If a gun has a very large current (> 0.7 A) at usual voltage values, it probably has a short. If the short is from a flake, it is possible to burn the flake off by leaving the gun on at low voltage values for several minutes. If that does not work, you must open the system to clean off the flake.

If the motors will not connect when the sputtering program starts up, reset the motor controller box located behind the computer screen.

Always check that the shutter plate is tightly screwed down when closing the system. This can be checked by using the program to open and close the shutter several times and making sure the positioning over the guns does not change. Also check this positioning after testing the guns during the actual run.

### 3.2.3 Pillar Definition

Now that the bottom leads have been deposited, they must be shaped into a series of junctions. This is done by patterning the desired junction shape onto the bottom lead using electron-beam lithography, then milling away the unwanted material with a vertical ion mill, and electrically isolating the junctions with a blanket SiO deposition. The SiO can block the electron-beam resist removal, so a horizontal side-ion-mill is used to break through to the resist before lift-off. These steps are shown in sections (c)-(g) of figure 3.3.

#### 3.2.3.1 Electron-Beam Lithography

Pillar definition of the bottom lead is done by electron-beam lithography. First, the chip must be coated in an appropriate electron-beam resist. We use the negative tone resist ma-N 2401. Spin the resist onto the chip at 3,000 RPM for 40 seconds to produce a 100 nm layer on the chip. The

resist is very thin compared to the S1813 photoresist so only 2-3 drops are needed to completely cover the chip. Then, bake the chip on the small hot plate in the fume hood for 120 seconds at 90 °C. Place the chip directly on the ceramic plate for the best heat exchange. After baking, the chip should look blue in color.

Now, load the chips and stigmation sample into the SEM for writing. As mentioned above, much of this work used a JEOL 840A SEM for writing, but since all future group members will use the new Hitachi SU5000 SEM, I will focus on the use of this system. After logging into the Hitachi system and opening the SEM software, choose the electron-beam lithography option and vent the system. Choose a sample holder based on the number of samples you would like to load at a time. The current maximum is a double-sided tray which can hold a total of eight half-inch square chips. Enter the sample holder size and sample height into the SEM software. The double-sided tray size is not built into the software, so choose the 51 mm circular holder for the closest size approximation. Our samples are also usually so flat that they measure less than 0 mm above the height baseline. In this case, enter the height as 0 mm. You will then have the option to take a picture of your samples in the holder with the external camera. This is helpful for quick movement from chip to chip and keeping track of which samples you have already written when writing many chips at a time.

When the main chamber is vented, pull the door open as far back as possible. Then, the 'move stage' button will become active. Pressing this button will raise the sample stage based on the sample height you entered into the software. If you can close the door without your sample hitting the height guard, then your sample will not be in the way of any microscope elements inside the chamber. If your sample would hit the height guard, adjust the sample height setting in the software.

After closing the door, click the button to evacuate the system on high-vacuum mode. Low-vacuum mode can be used for non-conducting samples, but gives worse image resolution. While the system pumps down, open the NPGS software and prepare the pattern write files if needed. This new SEM has been calibrated to write pillars with an area dose of 550 $\mu C/cm^2$ and line-

based features, such as the stigmation pinwheels, with a line dose of 2.5 $nC/cm$. These values should be reflected in the run file, as well as the beam current of 68 pA.

Now, turn on the beam with the default settings of spot size 1 and intensity 30. Move the field of view to the stigmation sample and bring the center of the chip into focus. It is very important to then change the z-height in order to obtain the desired working distance of 15 mm. The current working distance is stamped on the bottom of the SEM image on the screen. Increasing the z-height will proportionally increase the working distance. When the image is perfectly in focus, the working distance should read 15 mm. This must be done before stigmation or beam alignment as the working distance has an effect on these properties.

Any small feature on the stigmation sample can be used for stigmation. Zoom in on the small feature to about 200,000x magnification or more and quickly blur the feature in and out of focus. If the beam is properly stigmated, you will see a the feature blur uniformly in all directions as the focus is changed. Improper stigmation will lead to the feature stretching along a preferred axis as the focus is changed. To correct this, adjust the two stigmation knobs while the feature is in focus. The image will look sharper with more distinct features when the stigmation knobs are closer to the ideal settings, so cycle through adjusting the focus and both stigmation knobs until the image is as clear as possible and the feature blurs uniformly when the focus is changed.

Next, adjust the beam alignment by pressing the alignment button and working through several phases of alignment. In each case, use the alignment knobs, which are the same ones previously used for stigmation, to reduce the shaking of the image on the screen. It is easier to start this task at low magnification and work your way higher if the alignment begins far off.

After stigmation and beam alignment, move to the first chip for pillar writing. Before writing each chip, make sure that the chip is aligned vertically on the screen without any tilt. The tilt tool can be used to draw a line along a known vertical surface, such as the edge of the bottom lead or contact pad, and the software will automatically match that tilt. Then, move to the first write area and focus on one of the outer alignment crosses. Typically, an extra feature can be found at the inner corners of the crosses, which make an excellent feature to focus on. Focusing at 30,000x

magnification or greater is preferred. Then, zoom into the write area and center the inner L-shaped alignment marks on the screen. Do not zoom to a magnification higher than 1000x or image the write area for longer than needed as the electron-beam used to image can begin to develop the resist in that area and lead to improper feature size after development. After centering, reduce the magnification to 200x.

Switch the SEM to EBL mode in the NPGS software and run the alignment file. The alignment mini-game consists of matching up the outlined alignment pattern with the scan of the chip, which will show a similar pattern if the centering was done correctly. The outer alignment crosses are aligned at a magnification of 200x and the inner alignment L's are aligned at an increased magnification of 1000x. After alignment is complete, select the desired run file and run with alignment. This will write the DesignCAD pattern from the run file onto the chip using the previous alignment to determine where the center of the pattern should be placed on the chip. Continue to focus, align, and write the pattern at each write area on the chip. It can be helpful to keep a list of write areas to check off as they are completed if a large number will be written. Since the films are grown in field pointing parallel to the bottom lead, ellipses tend to be written with the long axis of the ellipse parallel to the bottom lead as well, so that this long axis is also the easy axis for any magnetic layers.

Once all chips are written, shut off the beam and vent the sample chamber. Then, develop the chips by wafting in AZ 300 MIF for 30 seconds followed by DI water for 20 seconds, and blowing dry with the nitrogen gun. The ma-N is a single layer of resist so it will not have an undercut profile. In fact, the resist profile has the opposite effect with broadening at the base of the resist. This, as well as the fact that the resist hardens with heating, can cause the ma-N to be difficult to remove in the later lift-off step.

Figure 3.5 shows two write areas on the same chip after development of the ma-N electron beam resist. The right image shows a pinwheel with the proper circular shape and equal line weights, indicating good focus and stigmation. Since the stigmation is set once while setting up the SEM writing, all chips written in that batch should also have proper stigmation. As the pinwheel on the

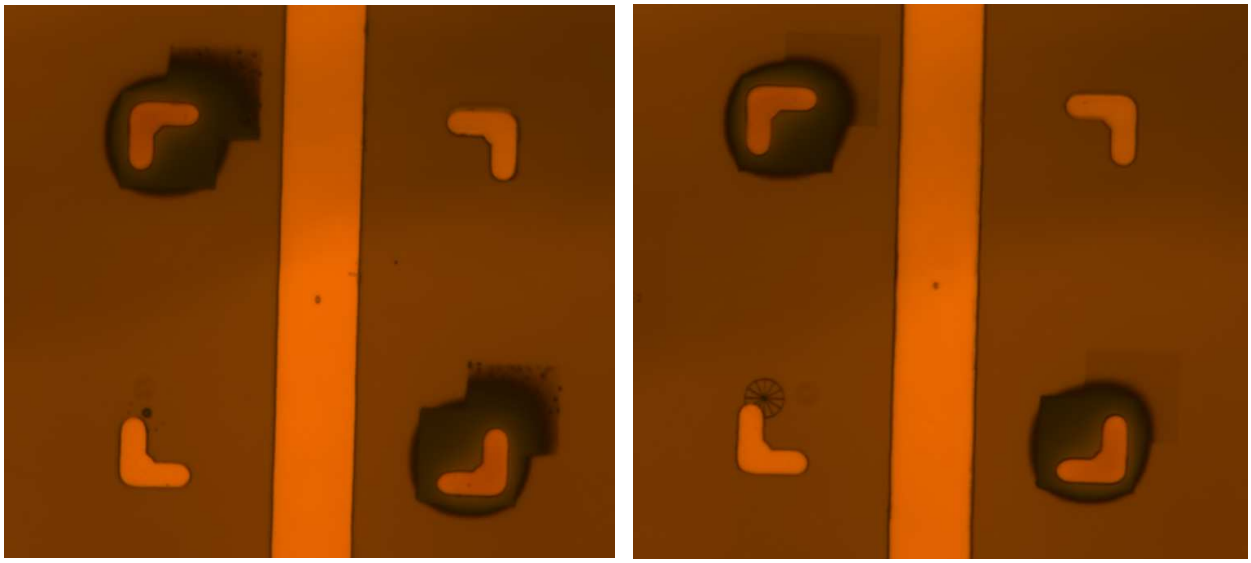

Figure 3.5 **SEM image of patterned ma-N resist** These SEM images show the ma-N resist patterned into the junction shape after electron-beam lithography and development. The small ellipse centered on the vertical bottom lead is the ma-N pillar. The pinwheel marker can be seen touching the lower left L shaped alignment mark. The left image shows a poorly formed pinwheel while the right image shows a properly formed pinwheel. Only the overlap areas of the pinwheel developed in the left image, indicating that the focus was off. The circular shape and equally weighted lines in the right image indicate proper focus and stigmation.

left shows, if the focus is off, only the overlap regions of the pinwheel shape will develop. Since the resist pillars are very small and difficult to see well in the optical microscope, the quality of the pinwheel gives confidence in the focus and stigmation of the SEM, and hence size and shape of the resist pillar.

#### 3.2.3.2 Ion Milling and SiO Deposition

Next, the junction is defined by ion milling. To begin, place the chip in a vertical ion mill holder. The face of the ion mill holder has a square opening to fit the 1/2 inch square chips with a smaller circular opening through which the mill reaches the sample. Only the junctions need to be milled, and they are clustered in the center of the chip, so, place a metal mask with a smaller 5 mm by 5 mm square opening in front of the chip to block the rest of the bottom leads from milling and SiO deposition. Next, place a copper heat-sink behind the chip with silver paste in between. You should

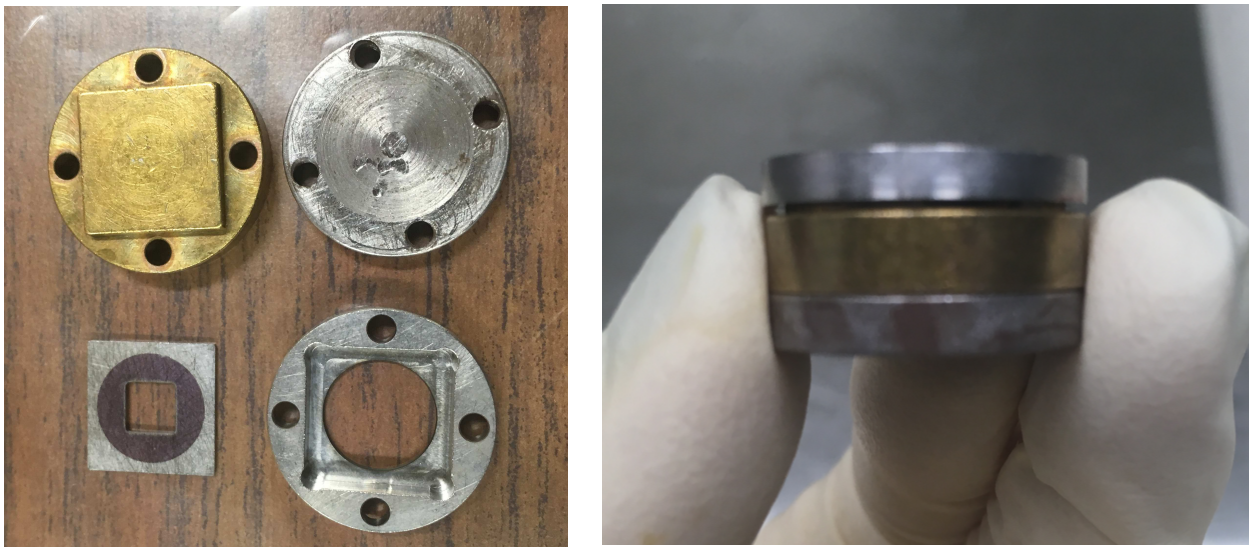

Figure 3.6 **Vertical ion mill holders** The left image shows the individual ion mill holder parts. The lower right corner is the holder face, and going clockwise are the metal mask, copper heat-sink, and magnetic piece. The right image shows a fully assembled holder showcasing the gap desired between the mask face and the copper heat sink.

see a gap between the holder face and the heat-sink indicating that the sink is in good contact with the chip. This is especially important since heating of the ma-N resist makes it more difficult to remove. Lastly, place a magnetic piece behind the heat sink and screw the three pieces together. Make sure that the screws are not so long as to protrude out the back of the holder. The parts of the ion mill holder and the desired gap between the holder face and heat-sink are shown in Figure 3.6.

Five samples can be loaded into the ion mill at one time. After loading the samples, wait for the pressure in the chamber to drop below $3 * 10^{-}8$ torr before beginning the milling process. The amount of material to be milled from the sample must first be converted into the equivalent thickness of Au since that is the only milling rate that can be measured in the chamber. Do this by adding up each material's thickness multiplied by the k factor, which converts a material's milling rate to that of Au. These k factors are all determined experimentally. Then, calculate the milling time by dividing the effective Au thickness by the measured Au milling rate in the chamber. To reduce heating of the ma-N, milling processes that take more than three minutes are split into 2-3 minute sections. Run the mill with the settings specified in Table 3.3 for the small chamber. The

beam current value will drift with time, but the rate remains stable if you do not correct for this drift. The cathode current will start around 5 mA when the filaments are freshly changed, and will decrease with use until it eventually breaks. It would be a good idea to preemptively change the filaments when the cathode current drops below 3 mA. The ma-N resist mills at a much slower rate than the bottom lead material, so after milling is complete, the whole bottom lead that was exposed has been milled down to the desired layer and the whole stack remains under the ma-N mimicking its shape and size as seen in part (d) of Figure 3.3.

After milling, wait until the wall of the chamber is cool to the touch before moving on to deposit the SiO. This will be used to electrically isolate the top and bottom leads as well as the edges of the pillar. It is important to turn up the voltage on the SiO boat slowly to increase chances of a stable deposition rate. 50 nm of SiO are deposited on each sample. The SiO deposition rate is measured by the FTM in the chamber and the desired SiO thickness is divided by this value to obtain the SiO deposition time required. During deposition, spin the sample with the chamber's magnetic arm to increase the uniformity of the layer and reduce the chance of pin-holes through the SiO. If the correct thickness was deposited, the SiO should look a maroon/brown color.

The SiO deposition is somewhat collimated and forms a uniform layer on top of the milled samples surfaces and the ma-N resist. Because of the sloped sidewall of the ma-N, it is possible for the SiO on the sample surface to creep up the sides of the pillar and connect to the SiO on top of the resist, forming a complete blanket on top of the chip. This is shown in part (e) of figure 3.3. This would make lift-off impossible, so an additional side-mill step is needed.

#### 3.2.3.3 Side-Milling and Pillar Lift-off

To break through the sidewall build-up, a side-mill is performed. Since the mill direction can't be changed in our chamber, place the sample in a holder that rotates it 87 °relative to the vertical ion-mill holder, so that the pillar is sticking out horizontally from the substrate and rotated 3 °down towards the ion mill. Perform a two minute mill on two sides of the pillar to break through the SiO sidewall and allow a gap for remover to affect the ma-N resist. Choose the two short edges

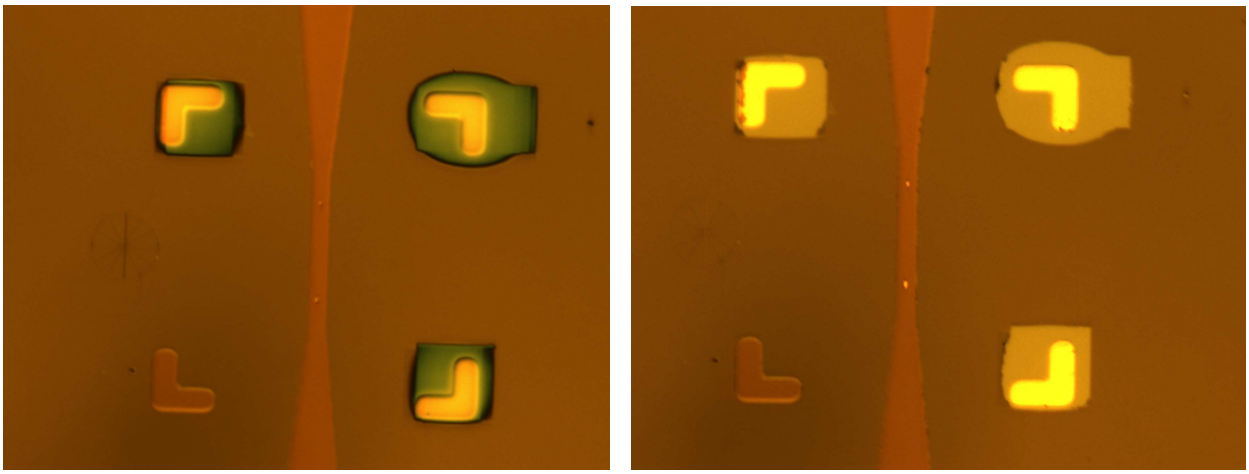

Figure 3.7 **SEM image comparison of write area before and after the lift-off process** The left hand image shows the sample before lift-off and the right hand image shows the sample after lift-off.

of the pillars to prevent the edges of the bottom leads from poking through and shorting to the subsequently sputtered top lead. This step is depicted in part (f) of figure 3.3.

Now, it is theoretically possible to lift-off the ma-N resist with its SiO cap to reveal a top contact for the junction below. It can be difficult to tell if the junction has lifted off with just the optical microscope. The best method is to directly compare the coloration of the pillar before and after the lift-off process. The microscope current and voltage settings and picture exposure time must remain the same in the before and after pictures for an accurate comparison.

After imaging the junctions, place each chip in a small beaker of Remover PG on a hot plate set to 110 °C. Let the chip sit in the remover for 10 minutes, then gently scrub the junction region of the chip with a q-tip from all angles and cover the beaker with an aluminum foil cap to better hold in the heat of the hot plate. Let the chips sit on the hot plate for an additional 30 minutes, then waft in DI water for 30 seconds and blow dry with the nitrogen blower. Image the junctions again in the optical microscope and compare with the before pictures. It should be very obvious that the L shaped inner alignment marks have lifted off and the junctions should look brighter in color. An example of a set of two junctions before and after lift-off can be seen in figure 3.7. A cartoon of successful liftoff is shown in part (g) of figure 3.3. If all junctions do not look lifted off, repeat the

whole lift-off process. Successful lift-off has taken as many as three full iterations of the process, but usually works on the first try when the samples were properly heat sunk in the ion milling and SiO deposition step.

Previous variants of this lift-off process included more vigorous scrubbing and 30 minutes in the ultrasonic after being on the hot plate. These steps were found to be unnecessary after the above heat sinking process was implemented. Previously, heat sinking was done with Santovac oil instead of the silver paste and it was not required to have a gap between the holder face and the heat sink. Either the Santovac oil or silver paste is probably a fine heat-sinking aid, but I prefer to use the silver paste since the Santovac oil can squish around to the front side of the chip and cause problems if too much is applied. The silver paste has more tolerance in the amount that can be used since it is thicker. The ma-N sometimes became so difficult to remove that the ultrasonic and q-tip scrubbing would remove the bottom leads from the substrate before the ma-N would lift off. The heat-sinking method above has a higher success rate, but it would be preferable in the future to have a process that does not require a side-mill step or q-tip assisted lift-off.

### 3.2.4 Top Lead Photolithography and Material Deposition

The last step in the fabrication process is to deposit the top lead superconductor material. First, oxygen plasma etch the chips to clean the surface of any residual ma-N. Clean the system by running at the resist stripping setting of 300 W and 500 mTorr for five minutes. Then, clean the chips in the system at the residual resist clearing setting of 100 W and 500 mTorr for 90 seconds.

The top lead photolithography is very similar to the bottom lead process described in section 3.2.1. Spin and bake the S1813 resist in the same way. Now, however, the alignment process is more involved since the 4 $\mu$m wide horizontal top lead must fully overlap the junction on the vertical bottom lead as shown in part (i) of figure 3.3. To aid in this more complicated alignment process, vernier alignment marks were implemented. The base set is included on the bottom lead mask, and they can be lined up with the outline on the top lead mask. The single pillar and SQUID masks use these same vernier alignment marks in three sizes. The alignment marks look like

fingers that become successively more spread out as they get farther from the center so that the white space between the marks on the chip and on the mask increase farther from the center of the marks. Several sets of these marks are stamped across the chip to more accurately align the position and rotation of the chip relative to the top lead mask. After alignment, the exposure and development process are the same as section 3.2.1.

In order to ensure a clean interface, oxygen plasma etch the developed chips again with the same process described above. Then, load the samples into cleaned sputtering holders and place them in the sputtering system. Bake the system for eight hours. The top leads require a less stringent starting pressure of only $6 * 10^{-8}$ Torr so they can usually be sputtered the day after baking without requiring an additional full day of pumping.

As an extra precaution for a clean interface, first ion mill 2 nm of Au from the surface of the chip. Run the mill at the large chamber settings from Table 3.3. Then, immediately sputter the top lead of 150 nm Nb and a capping layer of 10 nm Au to prevent oxidation. In the past, all samples were ion milled first, then all received the 150 nm Nb and 10 nm Au. This left the samples sitting around in the chamber for quite a while between being milled and having the Nb deposited, possibly leading to a less reliable interface.

After sputtering, the S1813 resist is lifted off in the same way as section 3.2.2. Now, fabrication is complete, and it's time to hope and pray that the samples are measurable.

#### 3.2.4.1 Small Feature Size Variant

Patterns with small feature sizes use the same bilayer resist spinning method, and exposure and development times as the bottom leads in section 3.2.2.1. As in the above top lead instructions, the small feature top lead patterns will also have a more involved alignment process with vernier alignment marks.

# CHAPTER 4

# NON-MAGNETIC MATERIAL OPTIMIZATION

The quality of data obtained from Josephson junctions depends on how the magnetic layers behave, but all the layers and interfaces in the junction stack can affect these magnetic properties. In this chapter, I will detail the characterization and optimization of the junctions' base superconducting electrode and normal metal spacer layers using Atomic Force Microscopy (AFM) to analyze surface roughness and SQUID Magnetometry to analyze the switching properties of a NiFe magnetic layer grown between different spacers.

## 4.1 Base Superconducting Electrode

The Birge group has been concerned about the surface roughness of the base superconducting electrode since before I joined the group. Any roughness introduced in this layer will be transmitted to the whole stack, which adversely affects the magnetic layers, especially as they become thin. The most common base layer for standard junction use was 150 nm of Nb. A previous student, Dr. Yixing Wang, worked to improve the roughness of this layer by introducing thin Al spacers within the Nb stack. He studied a base electrode with the structure [Nb(40)/Al(2.4)]$_3$/Nb(40), which he found to have a surface roughness of 2.3 Å compared to 5.3 Å found for Nb(150) [82, 72, 78].

To further characterize the multilayer base electrodes, I grew several new multilayer stacks and measured their surface roughness with AFM. The films were created by blanket sputtering on a cleaned Si chip with no post-processing. The nine sample stacks measured were Nb(150), Nb(100), [Nb(40)/Al(2.4)]$_3$/Nb(20)/Au(5), [Nb(25)/Al(2.4)]$_3$/Nb(20), [Nb(25)/Al(2.4)]$_4$/Nb(20), [Nb(40)/Au(2.4)]$_3$/Nb(20)/Au(5), [Nb(25)/Au(2.4)]$_3$/Nb(20), [Nb(25)/Au(2.4)]$_4$/Nb(20), and

[Nb(40)/Ru(2.4)]$_3$/Nb(20)/Au(5). Figure 4.1 shows a representative AFM image of each sample type and Table 4.1 below summarizes the surface roughness results.

This study found [Nb(25)/Al(2.4)]$_3$/Nb(20) to be the smoothest layer for use in Josephson junc-

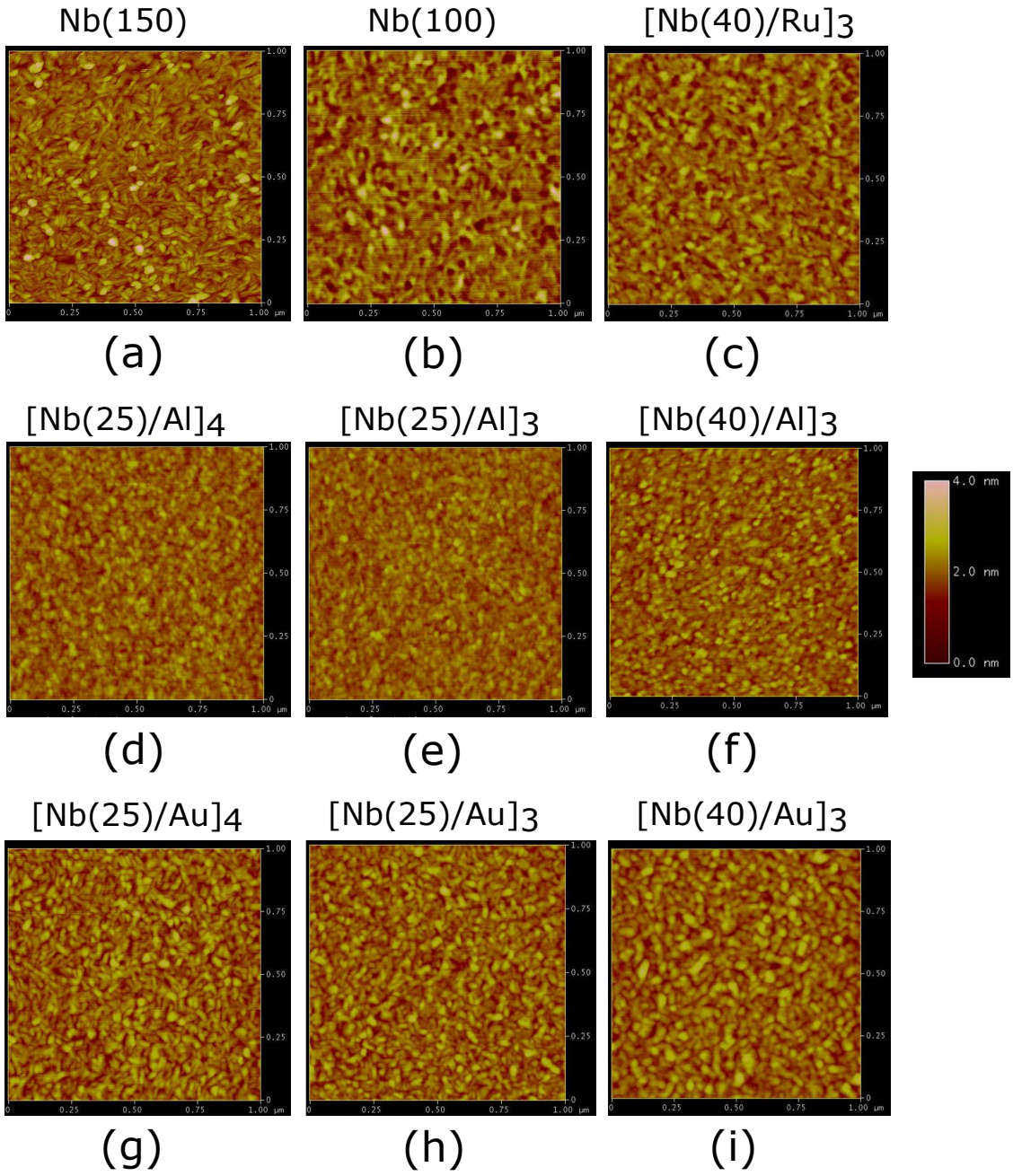


Figure 4.1 **AFM surface roughness comparison for nine base superconducting base layers** All the AFM scans use the same scale bar shown on the right and are 1 $\mu$m by 1 $\mu$m in size. The material stacks are (a) Nb(150), (b) Nb(100), (c) $[Nb(40)/Ru(2.4)]_3/Nb(20)/Au(5)$, (d) $[Nb(25)/Al(2.4)]_4/Nb(20)$, (e) $[Nb(25)/Al(2.4)]_3/Nb(20)$, (f) $[Nb(40)/Al(2.4)]_3/Nb(20)/Au(5)$, (g) $[Nb(25)/Au(2.4)]_4/Nb(20)$, (h) $[Nb(25)/Au(2.4)]_3/Nb(20)$, and (i) $[Nb(40)/Au(2.4)]_3/Nb(20)/Au(5)$.

| Material Stack | RMS Roughness (Å) | Figure Part |
|---|---|---|
| $[Nb(25)/Al(2.4)]_3/Nb(20)$ | 2.3 | (e) |
| $[Nb(25)/Al(2.4)]_4/Nb(20)$ | 2.5 | (d) |
| $[Nb(25)/Au(2.4)]_3/Nb(20)$ | 3.2 | (h) |
| $[Nb(25)/Au(2.4)]_4/Nb(20)$ | 3.4 | (g) |
| $[Nb(40)/Al(2.4)]_3/Nb(20)/Au(5)$ | 3.6 | (f) |
| Nb(100) | 4.0 | (b) |
| $[Nb(40)/Au(2.4)]_3/Nb(20)/Au(5)$ | 4.1 | (i) |
| $[Nb(40)/Ru(2.4)]_3/Nb(20)/Au(5)$ | 4.3 | (c) |
| Nb(150) | 8.3 | (a) |

Table 4.1 **RMS roughness values for superconducting base layers** The table shows AFM surface roughness values for the nine superconducting base layers listed in order of increasing roughness. $[Nb(25)/Al(2.4)]_3/Nb(20)$ has the smoothest surface with 2.3 Å of RMS roughness.

tions, showing about a 3.6 times reduction in RMS roughness compared to the standard Nb(150). $[Nb(25)/Au(2.4)]_3/Nb(20)$ would also be a good choice if the samples require more guns and there is not room for the Al gun in the sputtering chamber. The frequency of the roughness is also important for the growth of subsequent magnetic layers. Ideally, we would like to have low frequency roughness, but these nine base electrode options have little variation in the roughness frequency. Plain Nb has a rice grain structure, while introducing the Al layers seems to round them out and produce smaller grains. All the stacks with Nb(40) showed significantly increased roughness from their Nb(25) counterparts, but it is also possible that the Au capping layer is playing a part. Going from 3 to 4 repeats of the Nb(25)/Al(2.4) stack only affects the RMS roughness by a small fraction of an angstrom. If thicker bottom leads were needed, attempting a larger number of these repeats could provide a smoother solution. Judging by the highly improved RMS roughness of these layers compared to Nb(150), all junctions made with sensitive magnetic layers should use one of those smoother base electrodes.

An increased roughness was measured in the $[Nb(40)/Al(2.4)]_3/Nb(20)/Au(5)$ compared to Dr. Wang's previous results. This could be due to the Au capping layer or just different AFM tip morphology or instrument settings. The roughness of Nb(150) was also measured to be larger than Dr. Wang's.

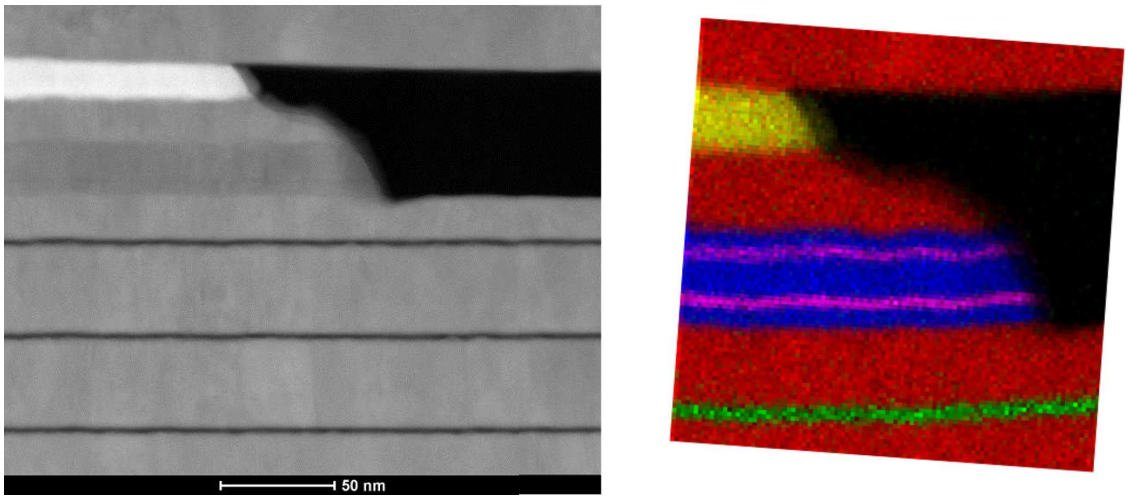


Figure 4.2 **TEM image of spin-valve Josephson junction with X-ray elemental analysis** This sample had the structure Nb(40)/Al(2.4)]$_3$/Nb(20)/Cu(5)/NiFe(1.5)/Cu(10)/Ni(1.2)/Cu(5)/Nb(20)/Au(15)/Nb(150)/Au(10). In the elemental analysis, red shows Nb, green shows Al, magenta shows Ni and NiFe, and yellow shows Au. This analysis shows that the layers are well defined. These images were collected by Nancy Missert and Paul Kotula at Sandia National Laboratory.

Our group was fortunate to be able to send several samples to Sandia National Laboratory to be measured in their TEM to see sample cross-sections with elemental analysis. One of their images, collected by Nancy Missert and Paul Kotula, is shown in Figure 4.2. The sample structure was Nb(40)/Al(2.4)]$_3$/Nb(20)/Cu(5)/NiFe(1.5)/Cu(10)/Ni(1.2)/Cu(5)/Nb(20)/Au(15)/Nb(150)/Au(10). In the elemental analysis, red shows Nb, green shows Al, blue shows Cu, magenta shows Ni and NiFe, and yellow shows Au. From this scan, we saw that our Nb/Al multilayer is indeed quite smooth and provides an ideal template for magnetic material growth. However, comparing the roughness of the two magnetic layers, even over this short distance scale, it is clear that the upper magnetic layer has increased roughness and lateral variation. This is likely due to the spacer and buffer layers of Cu(10) and Cu(5), respectively. In the next section, I will discuss our work to optimize the properties of these layers.

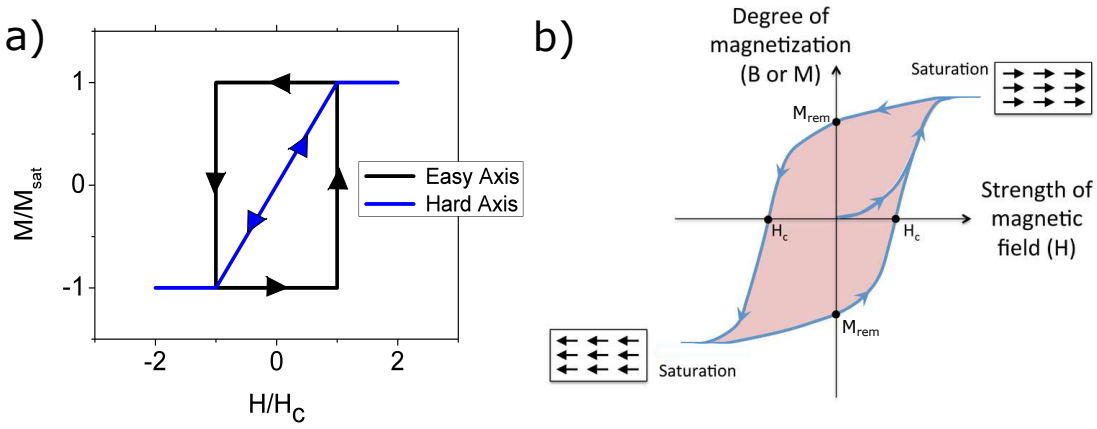


Figure 4.3 **Easy and Hard Axis Moment vs Applied Field Plots** Moment vs Field plots for a) an ideal permanent magnet with the applied field aligned along either the easy or hard axis and b) a typical real material. $M_{sat}$ represents the total or saturation magnetization of the material, $M_{rem}$ is the remanent magnetization that is left at zero applied field, and $H_c$ is the coercive field or the amount of field required to return the material's magnetization to zero after being saturated.

## 4.2 Normal Metal Buffer and Spacer Layers

The TEM images in figure 4.2 opened our eyes to the detrimental effect that our Cu spacer and buffer layers could have on the magnetics of a Josephson junction. It became obvious that we needed to characterize our normal metal layers and compare with some alternatives. This comparison was done by measuring the switching properties of a 1.5 nm NiFe layer surrounded by the various test spacer and buffer layers. Our general interest in NiFe will be discussed in the next chapter. Here we focus on the infered properties of the normal metal materials determined by changes in the switching properties of the NiFe. These switching properties were measured using a SQUID magnetometer to plot the Magnetization vs Applied Field of the samples. At high applied field values, the sample's magnetization will be fully saturated in the direction of the applied field. The direction that requires the least amount of applied field to saturate the magnetization is called the easy axis of the material. This is the energetically favorable direction for the magnetization to point. Typically perpendicular to this axis is the hard axis, which requires the most applied field to saturate. In single-crystal ferromagnets, there will be well defined easy and hard axes that point along certain crystallographic axes of the ferromagnet. The samples grown in this work are all

polycrystalline, so this magneto-crystalline anisotroly is washed out. In order to induce an easy and hard axis in polycrystalline films, they can be grown in the presence of an external field, which induces the easy axis parallel to the field direction. The expected response of the material's magnetization will be different when an applied field is oriented along the easy or hard axis, as depicted in Figure 4.3a. This ideal easy axis response has $M_{rem} = M_{sat}$ and perfect squareness. The values of $H_c$ will determine if the material is hard (high $H_c$) or soft (low $H_c$). A typical material, such as is shown in Figure 4.3b, will have $M_{rem} < M_{sat}$ and lower squareness characterized by the material's magnetization switching over a range of fields surrounding $H_c$ [71, 42].

Magnetization vs Applied Field plots were measured using SQUID magnetometry to compare the effect on the NiFe switching field, squareness, and saturation magnetization when surrounded by different normal metal materials. We tested the thin buffer layers Cu(2), Ru(2), and Cu(5), and thick spacer layers of Cu(10), Ru(2)/Al(7)/Ru(2), and Cu(2)/Al(6)/Cu(2). The additional layers were chosen based on those being used by our collaborators at Arizona State University and Northrop Grumman. All of the SQUID magnetometry measurements in this chapter were taken at a temperature of 10 K.

These samples were sputtered as a blanket film over the whole Si chip. The sample structure was $[Nb(25)/Al(2.4)]_3$/Nb(20)/Spacer/NiFe(1.5)/Spacer/Nb(5). The full base electrode was used to simulate the structure of a real Josephson junction. A magnet was placed behind the sample during deposition to create an easy axis in the NiFe switching along the field direction. The chips were snapped in half along the easy axis and both halves were loaded into the measurement straw, so the sample areas should be approximately the same for all samples. All measurements were performed with the field oriented along the easy axis and at 10 K.

Figure 4.4 shows the comparison of the three thin buffer layers. Both alternative buffer layers to the Cu(5) that has historically been used improved the magnetic properties of the NiFe, but the Cu(2) buffer gave the NiFe the lowest switching field and the most squareness. Figure 4.5 shows a similar comparison of the three thick spacer layers. Again, both alternatives to the conventionally used Cu(10) spacer improved the NiFe's magnetic properties. In fact, the multilayer spacers have

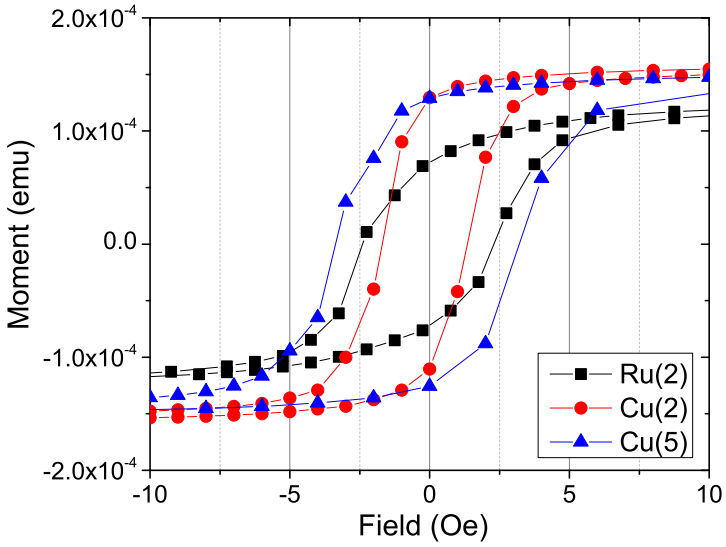


Figure 4.4 **Moment vs Field measurement for thin spacer (buffer) layers** The samples consist of NiFe(1.5) sandwiched by either Cu(2), Ru(2) or Cu(5). Based on this data, Cu(2) has the lowest NiFe switching field and loop squareness.

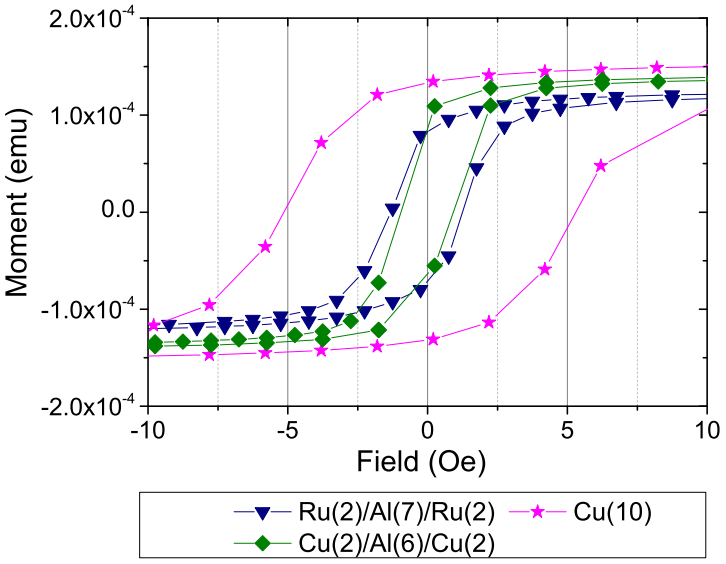


Figure 4.5 **Moment vs Field measurement for thick spacer layers** The samples consist of NiFe(1.5) sandwiched by either Cu(10), Ru(2)/Al(7)/Ru(2) or Cu(2)/Al(6)/Cu(2). Based on this data, both multilayer samples show highly reduced NiFe switching fields and improved squareness over Cu(10).

similar properties to the Cu(2) despite being 5 times thicker. In both spacers with Ru, the total moment was reduced in comparison with the Cu spacers. This suggests an increased dead layer at the Ru/NiFe interface.

The table below shows the coercive field for the six spacer layers. Based on these results, we planned to use Cu(2) as the buffer layer and Cu(2)/Al(6)/Cu(2) as the spacer layer in future Josephson junction studies to improve the magnetic layer quality. However, as you will see in later chapters, devices fabricated with this spacer, as well as the Ru(2)/Al(7)/Ru(2) spacer, showed highly reduced critical current values. The effect was so large that we decided to explore other spacer layer options of thinner Cu.

| Spacer or Buffer | Coercive Field (Oe) |
|---|---|
| Cu(2)/Al(6)/Cu(2) | 1.0 |
| Ru(2)/Al(7)/Ru(2) | 1.2 |
| Cu(2) | 1.5 |
| Ru(2) | 2.2 |
| Cu(5) | 3 |
| Cu(10) | 5 |

Table 4.2 **Coercive field values for six buffer and spacer layers**

The spacer layer is used to magnetically decouple the two ferromagnetic layers in the Josephson junction. We are interested in pursuing thinner spacer layers to improve the surface roughness of the spacer and subsequent magnetic layer, but if it is too thin, the magnetic layers in one device will couple and we will not be able to independently switch the magnetization directions of the individual layers. So, to fully test the effect of a spacer layer on the stack, a spin-valve structure was needed.

The samples had the form $[Nb(25)/Al(2.4)]_3$/Nb(20)/Buffer1/NiFe(1.5)/Spacer/Ni(2)/ Buffer2/ Nb(5). Buffer1 was either Cu(2) or Ru(2), Spacer was Cu(2), Cu(3), Cu(4), or Cu(5), and Buffer2 was always Cu(2). The full Nb/Al base electrode was used to recreate real Josephson junction conditions as far as roughness is concerned. The samples were sputtered as a blanket film on the Si chips with magnets on the backs of the sample during growth. No post-processing was per-

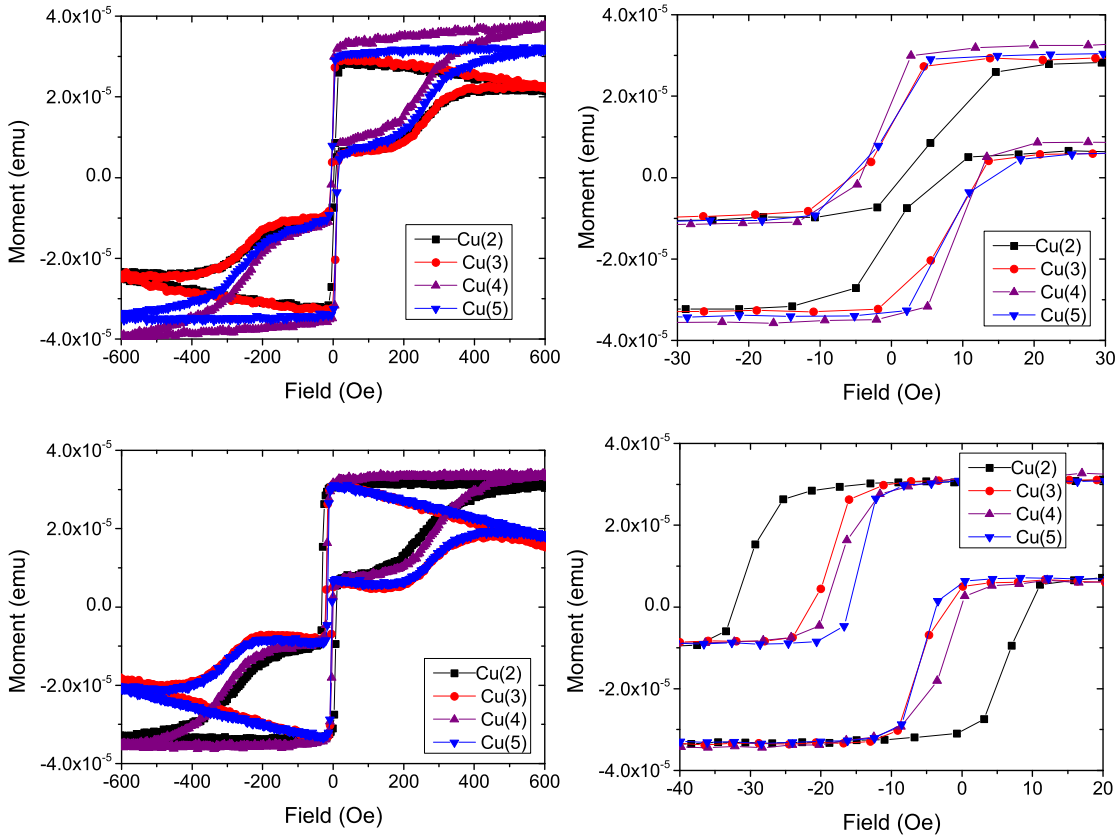


Figure 4.6 **Moment vs Field measurement for spin-valves with either Cu or Ru buffer layers** Moment vs Field measurement for spin-valves with either Cu(2) (upper plots) or Ru(2) (lower plots) as the bottom buffer layer and between 2 and 5 nm Cu for the central spacer layer. The magnetic layers are NiFe(1.5) and Ni(2). All plots show major loop data of both magnetic layers switching. The plots on the right side are zoomed in on the x-axis to show the NiFe switching. Ignore the horizontal shift of the data in the lower plot. This is an artifact of the measurement system.

formed. The samples were sent to Arizona State University where our collaborators measured Moment vs Applied Field loops both in the hard and easy axis directions. Our chips were diced to fit in their system and all chips were diced to the same size, so the total area should be comparable. The spin-valves were measured both along the easy and hard axis, though there was almost negligible difference between these two loops in all samples except for the sample with Cu(2)/NiFe(1/5)/Cu(2)/Ni(2)/Cu(2).

Figure 4.6 shows the results of these measurements. The upper plots have the Cu(2) bottom buffer layer and the lower plots have the Ru(2) bottom buffer layer. The different colors in the plot

represent the four Cu spacer layers at 2, 3, 4, and 5 nm. Both plots on the left side show the major loop of both the NiFe and Ni switching. All spacer thicknesses showed distinct switching between the two magnetic layers, indicating that they are not coupled. The NiFe was soft and switched at low field while the Ni switched slowly over a large field range from about 200 Oe to 500 Oe in both directions. Ignore the overall slope of the saturation magnetization; that is an artifact of the measurement apparatus. This slope could be subtracted, but we are not interested in a quantitative analysis of the Ni switching as real devices will operate at low fields that will (hopefully) not affect the Ni layer. Qualitatively, the Ni switching appears very similar as the spacer layer thickness is changed.

Both plots on the right-hand side of figure 4.6 are zoomed-in to the low-field region of the same major loop that is shown on the left. They are plotted over the same total field range for direct comparison. While the Cu(2) buffer layer samples show slightly lower switching fields of the NiFe, the samples with the Ru(2) buffer have increased squareness and a smaller switching field range. Unlike the previous results, a decreased saturation magnetization is not seen in the Ru(2) buffer layer samples. Later Josephson junction results revealed that even just one Ru buffer layer, like in the structure here, has a large negative effect on the critical current of the sample. So although the sharper switching of the NiFe is desirable, most future devices will rely on a Cu buffer layer. From the samples with a Cu buffer, the optimal spacer layer thickness was chosen to be 4 nm of Cu. Cu(2) was not a good choice due to it's poor squareness and Cu(3), Cu(4), and Cu(5) showed very similar behavior, so Cu(4) was chosen to be sufficiently far in thickness from Cu(2). So, to optimize magnetic layer switching properties and critical current yield, we chose to use the buffer layer Cu(2) and spacer layer Cu(4).

# CHAPTER 5

# MAGNETIC MATERIAL CHARACTERIZATION

The simplest phase-controllable memory device for JMRAM needs two magnetic layers, one free and one fixed. The free layer should switch magnetization directions over a small field range and require low switching fields. The fixed layer should be magnetically harder than the free layer and experience little to no magnetic change at fields that would switch the free layer. The point is for this layer not to switch magnetization directions, so it's switching characteristics are not particularly important, but a relatively low initialization field is desirable. In this chapter, I will detail SQUID magnetometry characterization measurements of free layer material NiFe and fixed layer candidates NiFeCo, NiFe/FeMn (NiFe pinned with FeMn), and Ni. All these measurements were performed on samples grown in our sputtering system and measured in the same SQUID magnetometer at a temperature of 10 K. Proper credit is given when samples were not grown/measured by me.

## 5.1 NiFe

NiFe, known also as permalloy when in 80/20 ratio Ni to Fe, has long been used in the electronics industry. It is desirable as a free layer because of its low coercivity and near zero magnetostriction. It is currently used in commercial MRAM, on which this superconducting analog is loosely based. Though our group has a permalloy target, the sputtered films show a Ni to Fe ratio of 84/16.

The one drawback of this material is its large magnetization. We have measured this value to be on the order of 800 kA/m for bulk films. If all other forms of anisotropy are controlled, the required switching field should be directly proportional to the material's magnetization. The group has investigated other free layer materials with lower magnetization values such as NiFeMo, NiFeNb, NiFeCu, and PdFe, but despite the lower magnetization, many of these materials did not show improved switching characteristics when compared to NiFe, while others require more

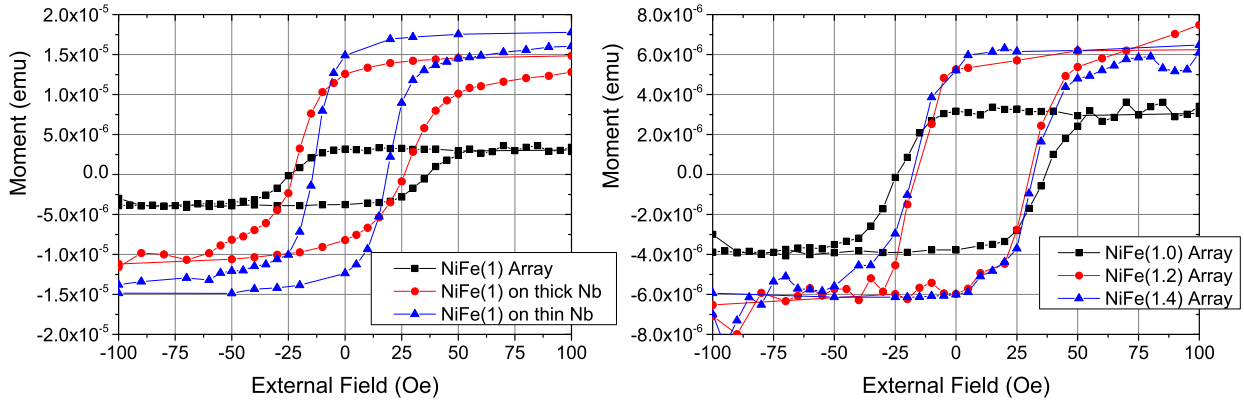


Figure 5.1 **Moment vs Field measurement for NiFe films and arrays** The left-hand plot shows comparison between NiFe(1) patterned into an array of over 9,000,000 0.5 $\mu$m$^2$ elliptical pillars with aspect ratio 2.5 and bulk films grown on 5 nm Nb and 100 nm Nb. The right-hand plot shows the NiFe switching behavior of three arrays with NiFe thickness 1.0, 1.2, and 1.4 nm. For both plots, the in-plane magnetic field was applied along the easy axis of the samples, corresponding to the major axis of the ellipses in the array. These data were measured by Joseph Glick.

evaluation. All the spin-valve devices featured in this work used NiFe as the free layer material.

Figure 5.1 shows 10 K SQUID magnetometry M vs H curves for NiFe thin films and arrays. All these samples were fabricated and measured by Joseph Glick. The 1 nm NiFe films had structure Nb(5)/Cu(5)/NiFe(1)/Cu(5)/Nb(5) for the sample grown on thin Nb. The thick Nb samples began with 100 nm Nb instead of only 5 nm. Data for these samples are shown on the left-hand plot in comparison to an array of 2.5 aspect ratio, 0.5 $\mu$m$^2$ elliptical pillars. Shaping these polycrystalline ferromagnetic films into small ellipses is done to induce the magnetic easy axis along the major axis of the ellipse. The arrays were grown on the thin Nb(5) base layer to clearly see the magnetic properties of the films unaltered by the roughness of a thicker Nb base layer. The pillars were defined by electron-beam lithography which stamped rectangles of 99 x 39 bits onto the chip over 2,400 times to fill an area of about 0.45 cm by 0.55 cm with over 9,000,000 pillars. These are then ion milled down through the ferromagnetic layer and halfway into the bottom Cu layer. The total moment of the NiFe(1) array is reduced compared to the extended thin films since there is proportionally less magnetic material in the arrays, but the switching fields and ranges can still be compared. The NiFe(1) grown on thin Nb has the smallest coercive field, which increases by 5-10

Oe when grown on thick Nb. The NiFe(1) array shows an even larger increase in coercive field from the extended film grown on the same thin Nb of about 15 Oe. The right-hand plot shows a comparison of three NiFe arrays of differing NiFe thickness. It is unclear why the arrays with 1.2 nm NiFe and 1.4 nm NiFe have such a similar moment. Possibly there is some non-uniformity run to run in the writing of the arrays that causes slight variation from the intended pillar size that is compounded due to the large number of pillars in the array. The coercive field decreases for the thicker samples, which has been observed in this and other materials at these low thickness values. The decreased switching field is desirable, but thicker layers will also reduce the critical current in Josephson junctions.

For JMRAM, we would prefer a free layer with a switching field below 10 Oe and with small variations in this value pillar to pillar. So far, these results with NiFe have been about as good as we can get with a switching field around 25 Oe. Ideally, a very soft material would be found for the free layer and NiFe could possibly act as a fixed layer with low initialization field. But, for now, it serves as our free layer in the thickness range from 1-2 nm.

## 5.2 Ni

Historically, Ni has seen a lot of use in the Birge group. It has been found to be quite hard in thin films but allows the most critical current of any material tested to date [44]. For these reasons, it makes a desirable hard layer. Originally, 1.2 nm Ni was used as a hard layer by several group members. But, this layer required a very high initialization field of 2600 Oe in Josephson junctions and did not always initialize into the same magnetic state, indicating non-uniform magnetization. So later, thicker films of 1.6 and 2.0 nm Ni were investigated in search of favorable magnetic characteristics and lower initialization field requirements.

Spin valve films were fabricated to determine the affect of changing Ni thickness in a full sample stack. The structure was $[Nb(25)/Al(2.4)]_3$/Nb(20)/Cu(2)/NiFe(1.5)/Cu(4)/Ni(x)/Cu(2)/Nb(5) with x = 1.2, 1.6 and 2.0 nm. No post-processing was performed, and samples were sent to collab-

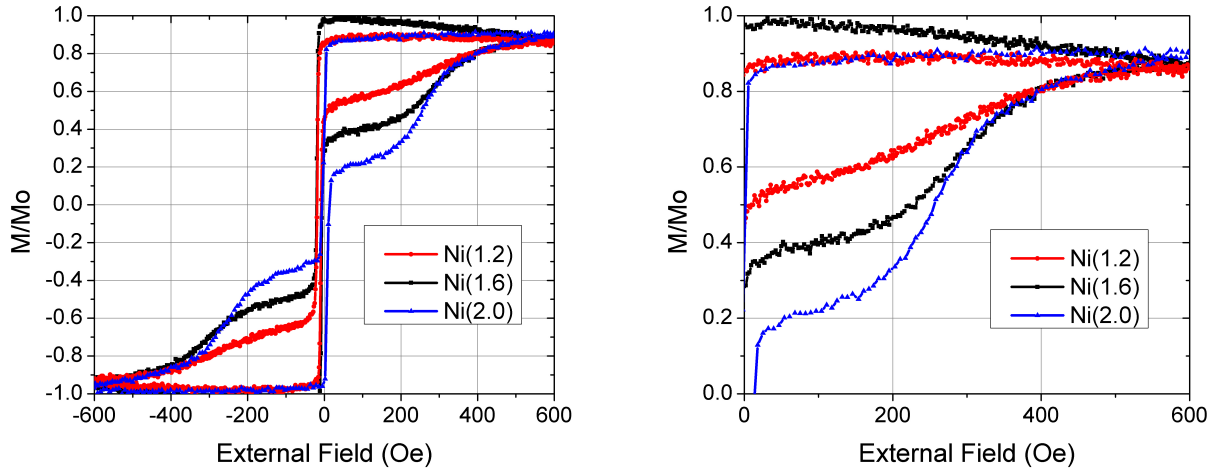


Figure 5.2 **Normalized moment vs applied field for spin valve NiFe/Ni samples** The samples contain 1.5 nm NiFe and Ni varying between 1.2, 1.6, and 2.0 nm. The slight downward slope of the 1.6 nm Ni data as it approaches saturation is an artifact of the measurement system and can be ignored. All the samples show similar behavior in both magnetic layers. The right-hand plot zooms in on the upper right quadrant of the left-hand plot to better show the Ni switching comparison.

orators at Arizona State University for VSM measurement. Figure 5.2 shows the normalized moment vs applied field data comparison for the three samples. No change in the NiFe characteristics were expected, but surprisingly, these thin films showed almost no change in the Ni characteristics either. The left-hand plot shows the whole major loop with the NiFe switching very close to 0 field and the Ni switches more gradually, saturating by 600 Oe in either direction. The right-hand plot zooms in on the upper right quadrant of the left-hand plot, and shows that the switching range and saturation field as well as qualitative shape are incredibly similar between the three samples.

To further investigate thicker Ni as a fixed layer candidate, an array was fabricated with the structure Nb(5)/Cu(5)/Ni(2)/Cu(5)/Nb(5) with the same array fabrication process described above. Figure 5.3 shows the normalized moment vs applied field for this sample compared to an extended thin film of Ni(2) measured by Caroline Klose. The array data has more noise due to the low total moment, but the comparison shows that while the coercive field remains relatively the same, the array has a much longer tail before all the junctions are saturated into the same magnetization direction. This is promising for a lower initialization field requirement for a 2.0 nm (compared to

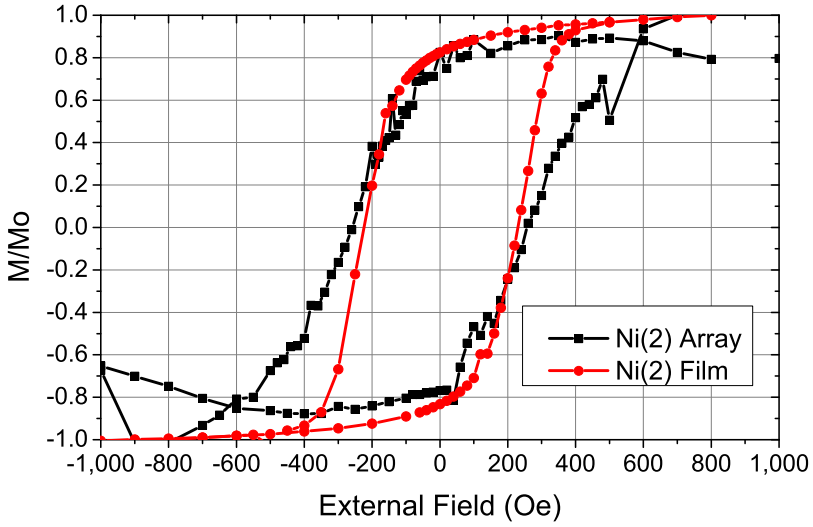


Figure 5.3 **Moment vs applied field measurements of Ni array and extended film** Normalized moment vs applied field for Ni(2) comparing an extended thin film and an array of 0.5 $\mu$m$^2$ elliptical pillars with aspect ratio 2.5.

a 1.2 nm) Ni fixed layer. Josephson junctions with 1.2, 1.6, and 2.0 nm Ni will be further explored later in this work.

## 5.3 NiFeCo

$Ni_{65}Fe_{15}Co_{20}$ was another material that I magnetically characterized and later used in SQUID devices. This material was a fixed layer candidate with it's high magnetization value of about 1000 kA/m. My first study of this material compared SQUID magnetometry measurements of bulk NiFeCo (a 200 nm sample), and extended thin films with thicknesses of 2.5 nm, 5.0 nm, and 7.5 nm NiFeCo. The bulk sample was grown directly on the Si substrate and the thin films were sputtered with the structure Nb(25)/Cu(5)/NiFeCo(x)/Cu(5)/Nb(5) and were measured with no post-processing. All measurements were performed with the applied field in the plane of the film, but applied both in the easy and hard axis directions according to the growth field of the film. These data are shown in Figure 5.4 with the easy axis data shown in black and the hard axis data shown in red. The first obvious observation about these data is that there is a noticeable difference

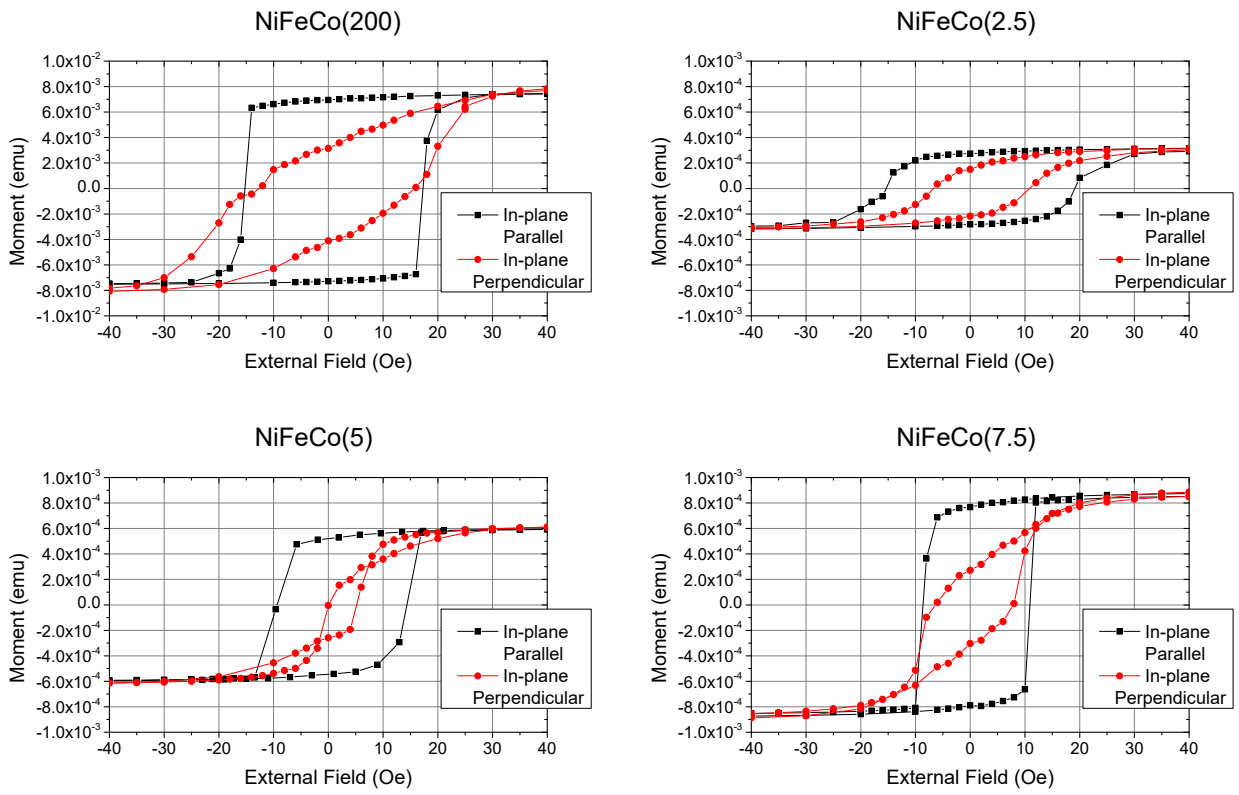


Figure 5.4 **Moment vs Field measurement for NiFeCo films** Bulk (200 nm), 2.5 nm, 5.0 nm, and 7.5 nm films were measured for comparison. The black data in each plot were measured with the external field pointing along the easy axis of the film (in the direction of the magnetic field applied to the film during growth), and the red data were measured with the external field pointing in-plane along the hard axis of the film.

between the easy and hard axis data for all thicknesses measured, so growing this material in a field does set a preferred magnetic direction in the film. The easy and hard axis behavior is more idealized in the thicker films and deteriorates as the thickness decreases. In all samples, the hard axis trend shows a mix of model hard and easy axis behavior.

These initial results showed low switching fields despite the large magnetization value of the material. Joseph Glick made and measured thinner samples in order to compare more directly with the switching properties of NiFe and to investigate material thicknesses closer to the expected range for 0-$\pi$ switching. Figure 5.5 shows the easy axis data above of the thin film samples with NiFeCo thicknesses 2.5 nm, 5.0 nm, and 7.5 nm in comparison to a 1.0 nm sample measured by Joseph.

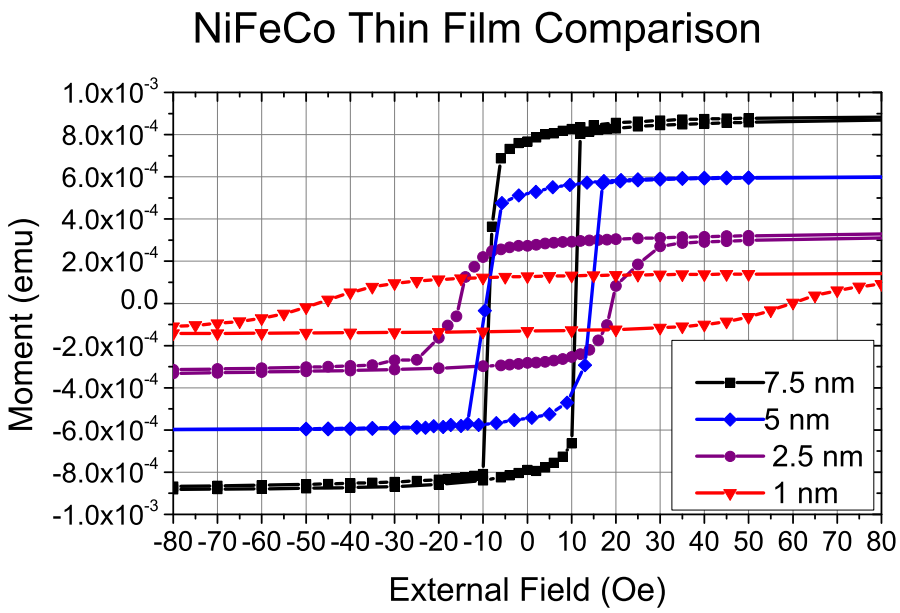


Figure 5.5 **NiFeCo thickness comparison of Moment vs Field measurements** All samples were grown on the same base layer of Nb(25) and all data shown were measured with the field applied in the plane of the film and along the easy axis. Thicknesses of 7.5 nm, 5 nm, 2.5 nm, and 1 nm (fabricated and measured by Joseph Glick) NiFeCo are shown. The total moment decreases with thickness and the film's coercive field increases, with the field increasing by over two times going from the 2.5 nm to 1 nm NiFeCo sample. The saturation moment of the 1 nm samples appears larger than expected in comparison to the other data due to different amounts of the chip being loaded into the system between Joseph and myself.

This new 1.0 nm sample was grown with the same structure as the thicker films. This figure shows that there is a small increase in the coercive field of NiFeCo from 7.5 nm down to 2.5 nm, but the 1.0 nm samples shows a highly increased coercive field. The coercive field value increases by over two times from 2.5 nm NiFeCo to 1.0 nm NiFeCo giving the 1.0 nm film a coercive field of over 50 Oe. This coercive field is large enough to use NiFeCo as a fixed layer in a junction with NiFe as the free layer. NiFeCo's coercive field will also increase when the film is patterned into small junctions. We also want our fixed layer material to have a relatively low initialization field. This plot shows that even the 1.0 nm film is fully saturated before 100 Oe. Though this value will also increase when the film is patterned, it is significantly lower than the saturation field of Ni films, so it will require a much lower initialization field in a spin-valve junction.

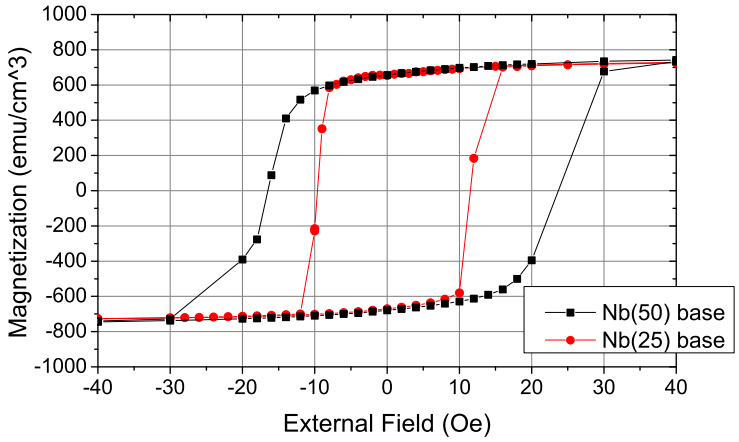


Figure 5.6 **Moment vs Field measurement of 2.5 nm NiFeCo films grown on 25 or 50 nm Nb base** This comparison shows how the magnetic properties of the film are altered because of the surface roughness of the underlying layers.

Lastly, a comparison was made to see the effect of a thicker Nb base layer on the NiFeCo thin film. Samples were fabricated with the structure Nb(25 or 50)/NiFeCo(2.5)/Au(2). The results are shown in Figure 5.6. Comparing with the 2.5 nm data shown in the plots above, these films do not have the Cu buffer layers surrounding the magnetic material. Looking at the NiFeCo 2.5 nm thin film grown on 25 nm Nb with and without the Cu buffers, the film without the buffers shows a reduced coercive field. The switching range is more difficult to compare since the data without the Cu buffer seem to have finer point spacing. The two curves in Figure 5.6 show that the increased thickness (and therefore roughness) of the base Nb layer do have a significant effect on the switching properties of the NiFeCo film.

## 5.4 NiFe/FeMn

The magnetics community has long known that the antiferromanget $Fe_{50}Mn_{50}$ can be used to pin another magnetic layer in a desired direction by "exchange bias" [54]. This trick is commonly used to measure GMR samples but has not been used in Josephson junctions due to the large reduction in critical current the FeMn was believed to cause. We decided that the desirable magnetic properties

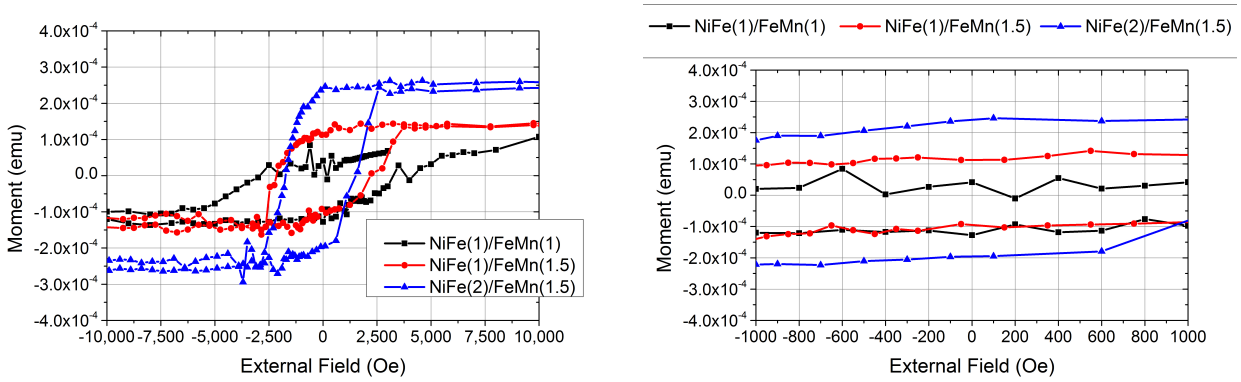


Figure 5.7 **Moment vs Field measurements of NiFe/FeMn pinned bilayer samples** Samples with NiFe(1)/FeMn(1), NiFe(1)/FeMn(1.5), and NiFe(2)/NiFe(1.5) are shown. The left-hand plot shows the full loop. Very large fields are required to unpin the bilayer even at these small thicknesses of FeMn. The right-hand plot zooms in on the field range from -1000 to 1000 Oe where there is very little change in the magnetization in all thickness sets.

of a pinned fixed layer were too advantageous not to investigate. First, magnetometry studies were performed to determine what thicknesses of FeMn and NiFe would produce good pinning and what external field values would be needed to break this pinning. Later chapters will detail the results of Josephson junctions made with these layers.

To reduce the loss of critical current through future Josephson junctions, very thin layers of NiFe and FeMn were investigated. Samples were fabricated with structure Nb(5)/Cu(5)/NiFe(x)/ FeMn(y)/Cu(5)/Nb(5) with x/y combinations of 1.0/1.0, 1.0/1.5, and 2.0/1.5. Extended thin films were grown in a magnetic field and measured after no post-processing. Figure 5.7 shows the comparison of the moment vs applied field for these three combinations. Note that the x axis values are much larger than any shown previously. Even at these very thin values of NiFe and FeMn, the layers remain pinned for several thousand Oersted of field. The right-hand plot shows a zoomed in view of the left-hand plot from -1000 to 1000 Oe. In this large field range, there is little noticeable change in the magnetization of the pinned layers, showing that they would be robust fixed layers at field values far larger than those needed to switch a free layer of NiFe.

Through these SQUID magnetometry measurements, we also learned that the blocking temperature for the thin FeMn system is below room temperature as seen in Figure 5.8. This sample with

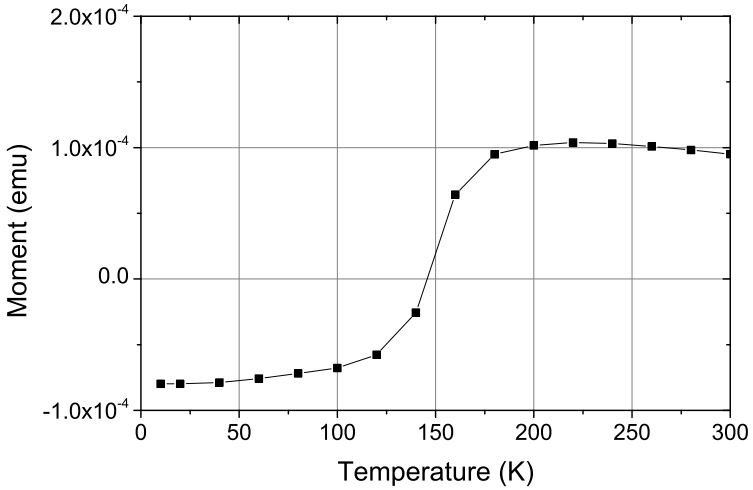


Figure 5.8 **Moment vs Temperature plot for the NiFe(1)/FeMn(1.5) bilayer sample** At low temperature, the sample is initialized with a negative magnetization. Then the temperature is slowly increased with a +100 Oe field applied. The moment of the NiFe/FeMn bilayer transitions from negative to positive between 100 and 200 K, indicating that the blocking temperature is within this range. It is not ideal that this temperature is below room temperature.

NiFe(1)/FeMn(1.5) was initialized to have a negative moment by cooling from room temperature to 10 K in the presence of a -100 field. Then a +100 Oe field was applied while the temperature was slowly increased to 300 K in 20 K steps, while measuring the magnetization at every step. Between 100 and 200 K, the pinning breaks down and the NiFe is able to switch to point its magnetization in the positive direction. This indicates a blocking temperature in this range. It is not ideal that the blocking temperature is below room temperature since growth in a magnetic field will not set an easy and hard axis directions and the sample must be cooled in a field to initialize the magnetization direction. The samples with other thickness combinations showed similar results.

# CHAPTER 6

## SINGLE FERROMAGNETIC LAYER JOSEPHSON JUNCTIONS

SQUID magnetometry measurements give important information about the basic properties of different magnetic materials and how those properties change when grown on different normal metal and superconducting layers. But, there are many other parameters that can only be addressed by transport measurements of Josephson junctions. In this chapter, I will discuss measurements of Josephson junctions that contain a single ferromagnetic layer (or single pinned layer). This type of measurement gives additional information about how a material will behave in a real sample that undergoes all the same processing that will be needed for a JMRAM device.

Sets of samples were fabricated using the steps outlined in Chapter 3 to create chips with micron-sized Josephson junctions containing a single ferromagnetic interlayer. Each chip had a different ferromagnetic layer thickness to cover a range of thickness values. Fraunhofer patterns were measured to learn about the transport properties of these junctions. The critical current and phase state of the junctions depend on the F layer thickness, as discussed in Chapter 2. The amount of critical current that can travel through the junction and how quickly that critical current decays with F layer thickness are important parameters. The thickness where the critical current is completely suppressed indicates the ground state phase of the junction changing between 0 and $\pi$. This is called the 0-$\pi$ transition thickness and tells how much a Cooper pair will dephase as it travels across the junction. Knowing these values about a single magnetic layer is crucial to be able to put together a viable two layer system. Magnetic changes in the junction will also manifest themselves as changes in the shape of the Fraunhofer pattern, so magnetic switching and the fields at which it occurs can be determined from these Fraunhofer patterns as well. These magnetic switching values are more useful than SQUID magnetometry of extended thin films since they include all the roughness and interlayer effects of the whole junction stack and the shape anisotropy and switching mechanism of a patterned bit. They can also give more detailed information than SQUID magnetometry of an array. In array measurements, you can't tell the magnetic state of a

single bit, only the whole array of bits. So if a magnetization of 0 emu is measured, you can't tell if each bit has 0 magnetization or if half are fully magnetized in one direction and the rest are fully magnetized in the opposite direction. By contrast, in single bit measurements, any deviations from the typical Fraunhofer pattern must be directly due to the one magnetic layer in the junction. The trade-off is that fabrication and measurement of a series of Josephson junctions is much more time consuming than SQUID magnetometry.

This chapter will detail my work to measure single junctions with a thickness range of NiFeMo and NiFe/FeMn (pinned NiFe). I will also show results from Joseph Glick's measurements on NiFe and NiFeCo since I used these materials in spin-valve devices.

## 6.1 NiFeMo

The first material that I investigated in single-layer Josephson junctions was $Ni_{0.73}Fe_{0.21}Mo_{0.06}$. This alloy, near the concentration of commercial supermalloy, has low coercivity, like NiFe, but a smaller moment. The Stoner-Wohlfarth model for magnetization switching by coherent rotation of a uniform ellipsoid indicates that the switching field for that material is directly proportional to the total moment of the material [74]. So, a material with good magnetic properties and a moment lower than that of NiFe would likely require a lower switching field and switching energy in that regime, and thus be a better free layer candidate for spin valve devices.

Single-layer junctions were fabricated with the structure Nb(150)/Cu(5)/NiFeMo(x)/Cu(5)/ Nb(20)/Au(20)/Nb(150)/Au(10) where x ranges from 1.0 to 2.7 nm in steps of 0.1 or 0.2 nm. The junctions were patterned into elliptical pillars with nominal axis lengths of 1.26 x 0.5 $\mu m^2$, giving them an area of 0.5 $\mu m^2$ and an aspect ratio of 2.5. The I-V characteristics of each junction were measured using a four-terminal SQUID-based self-balancing potentiometer over a field range of -60 to 60 mT (1 mT = 10 Oe), with the external field applied in the plane of the junctions and parallel to its major axis. The standard I-V characteristic for an overdamped Josephson junction (from equation 2.16) was used to fit the data and extract the critical current value for each field

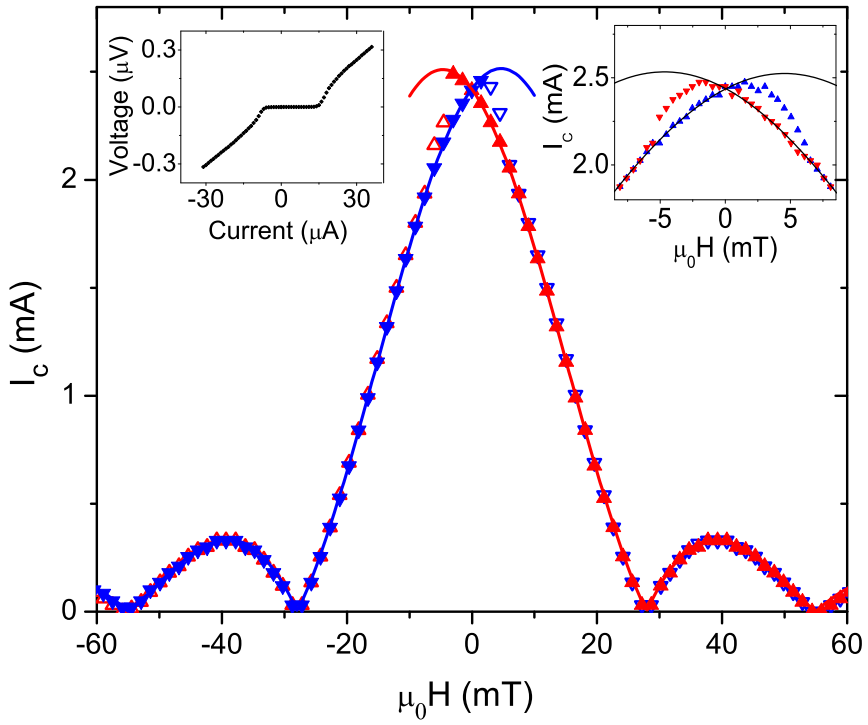


Figure 6.1 **Fraunhofer pattern for S/F/S Josephson junctions with 1 nm NiFeMo** The blue data show the field sweep in the positive direction and the red data show the field sweep in the negative direction. In both cases, the Fraunhofer pattern is shifted horizontally in the opposite direction of the NiFeMo magnetization. The left inset shows a typical I-V curve for the Josephson junctions in this series. The right inset shows the low field behavior of the same junction by taking smaller field steps of 0.5 mT between -8 and 8 mT to more clearly see the range of field values over which the NiFeMo layer changes its magnetization direction. H is an in-plane field pointing along the major axis of the elliptical junction. Figure was taken from [57].

and the normal state resistance of the junction. The latter quantity is determined by the slope of the I–V relation at currents much larger than the critical current, and preferably where the critical current value is as small as possible.

A Fraunhofer pattern was then created by plotting the critical current vs the applied external field. The Fraunhofer pattern and its accompanying equations are more fully described in Chapter 2. For an elliptical junction, the patterns are technically Airy patterns, but I will continue to call them Fraunhofer patterns out of habit. The junctions in this series had thin enough ferromagnetic layers to reproduce the theoretical Fraunhofer patterns, so they could be fit with the functional form $I_c = I_{c0} * [2J_1(\pi\Phi/\Phi_0)/ (\pi\Phi/\Phi_0)$ where $J_1$ is a Bessel function of the first kind, $\Phi = \mu_0$(H-

$H_{shift}$)w($2\lambda_L$+2$d_N$+$d_F$) is the flux through the junction, and $\Phi_0$=h/2e is the flux quantum. H, w, $\lambda_L$, $d_N$, and $d_F$ are the applied field, width of the minor axis of the elliptical pillar, London penetration depth of the Nb electrodes (measured to be 85 nm in our samples), and the thickness of the N and F layers, respectively. [9]. The field shift, y-intercept current $I_{c0}$, and junction width were allowed to vary while the other parameters were set to their nominal values. One Fraunhofer pattern is shown in Figure 6.1 for NiFeMo = 1 nm. The pattern was collected by sweeping the applied field first from -60 mT to 60 mT then back again. The blue data show the positive sweep direction and the red data show the negative sweep direction. A typical Fraunhofer pattern is centered on zero field, but this pattern shows a shift in the central peak position opposite to the NiFeMo magnetization direction, and a sharp transition to a Fraunhofer pattern shifted in the reversed direction. The change from a positively-shifted Fraunhofer pattern to a negatively-shifted Fraunhofer pattern signals the reversal of the NiFeMo magnetization direction which occurs in the field range of 1–6 mT. In Figure 6.1, the solid symbols were fit to the theoretical pattern, while the hollow symbols indicate where the magnetization of the NiFeMo changes direction. The hollow symbols of the positive (negative) sweep direction line up with the solid symbols of the negative (positive) sweep direction showing that the magnetization direction is fully switching. The excellent quality of the Fraunhofer patterns with nodes approaching zero critical current indicate that the current density is uniform at the central peak of the pattern, there are no short circuits in the surrounding oxide, and there is no flux trapped in the junction electrodes. The fact that the data at H = 0 lie on the fitted curve indicates that the remanent magnetic state of the NiFeMo nanomagnet is probably single domain.

The right inset of Figure 6.1 shows the peak of the pattern measured again with finer field point spacing of 0.5 mT over the field range from -8 to 8 mT. This inset shows that the NiFeMo layer does not switch its magnetization direction instantly in one field step, but more slowly over a range of about 5 mT. This doesn't mean that the bit is multidomain. This effect could be due to a curling of the magnetization at the ends of the bit. But either way, it is not a preferable characteristic for a free layer material in JMRAM.

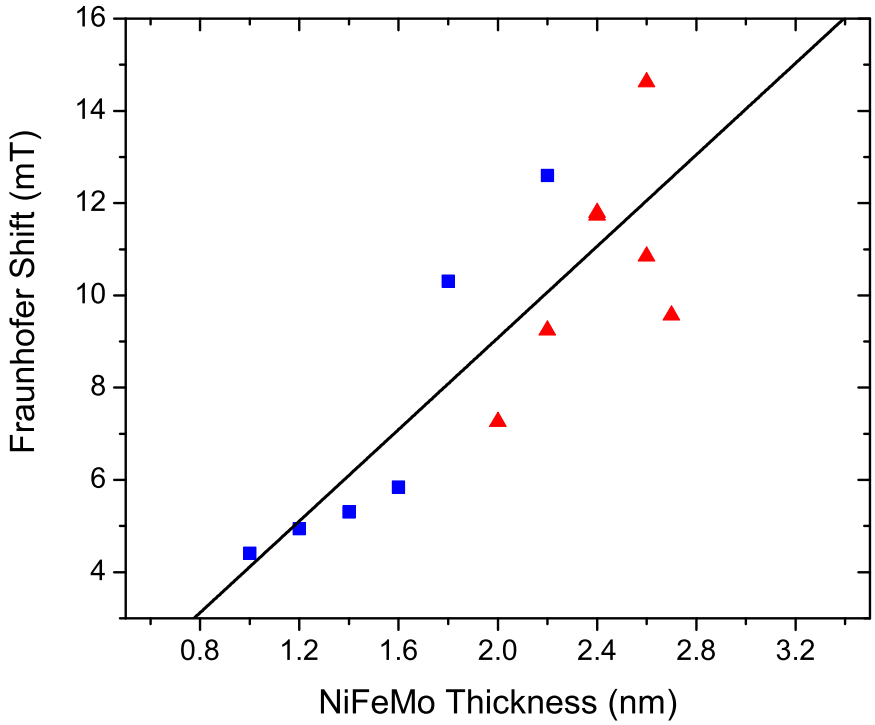


Figure 6.2 **Average Fraunhofer pattern shift vs NiFeMo thickness** The blue and red data represent junctions that were fabricated in two different sputtering runs. The linear fit to the data was used to calculate a magnetization value for NiFeMo of 710 $\pm$ 140 kA/m (1kA/m = 1 emu/cm$^3$) and the dead layer thickness to be 0.14 $\pm$ 0.42 nm.

Figure 6.2 shows the horizontal shift in the Fraunhofer pattern as a function of NiFeMo thickness. The shift value plotted is the average between the positive and negative sweep directions. The amount of shift in each pattern should be proportional to the F-layer magnetization M and should increase with the F layer thickness since the flux in the junction from a uniform magnetization M is equal to $\Phi_M = \mu_0 \mathrm{M w d}_F$. There is significant scatter in the data, but they show a roughly linear trend. The slope and x-intercept of the linear fit was used to calculate the NiFeMo magnetization and dead layer thickness. The magnetization was found to be 710 $\pm$ 140 kA/m (1kA/m = 1 emu/cm$^3$) and the dead layer thickness was 0.14 $\pm$ 0.42 nm. This is consistent with previous SQUID magnetometry measurements indicating a bulk saturation magnetization of 590 $\pm$ 60 kA/m.

Figure 6.3 shows the culmination of this measurement series, the critical current times normal

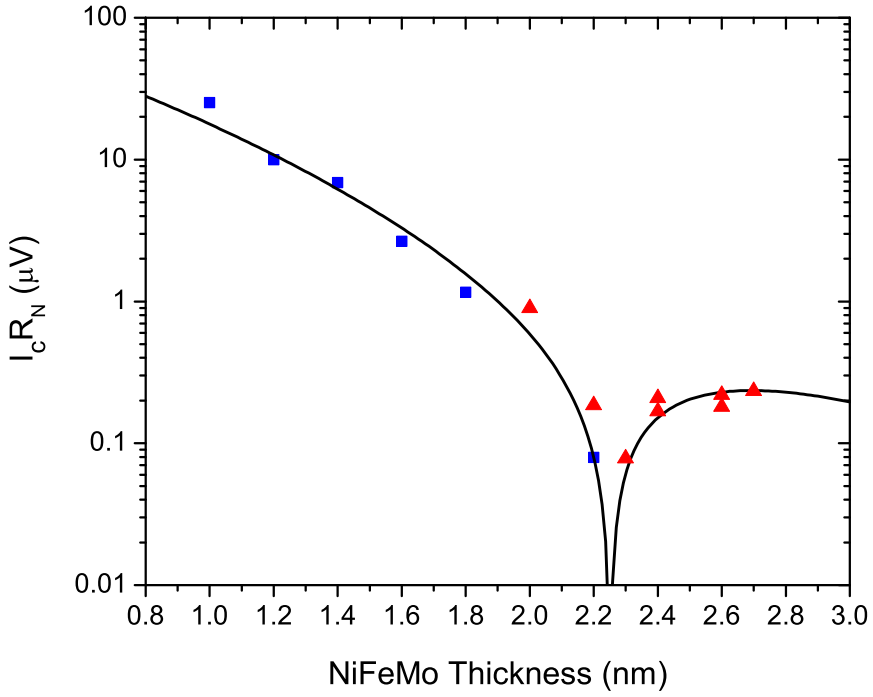


Figure 6.3 **Characteristic junction voltage,$I_cR_N$, vs NiFeMo thickness** The blue and red symbols represent junctions that were fabricated in two separate sputtering runs. The solid line is a fit to the data (further explained in the text) and indicates that the 0-$\pi$ transition for NiFeMo occurs at 2.25 $\pm$ 0.01 nm.

state resistance product ($I_cR_N$) vs the NiFeMo junction thickness. The critical current values used came from the maximum of the Fraunhofer pattern for each thickness. The data was fit with the equation $I_cR_N = V_0 * e^{-d_F/\xi_{F1}} * \cos(d_F/\xi_{F2} - \phi)$ where $\xi_{F1}$ and $\xi_{F2}$ are the length scales governing the decay and oscillation of the critical current, respectively, and $\phi$ is a phase shift [17]. From the fit, we obtained $V_0$ = 150 $\pm$ 50 $\mu$V and $\xi_{F1}$ = 0.48 $\pm$ 0.04 nm. The values for $\phi$ and $\xi_{F2}$ can only be determined unambiguously if more than one 0-$\pi$ transition is observed. That was not possible in this work due to the steep decay of the critical current with NiFeMo thickness. But, if the value of $\phi$ is fixed to the value $\pi/4$, as is suggested for this type of junction in the literature [33], then we obtain $\xi_{F2}$ = 0.955 $\pm$ 0.004 nm, although the true uncertainty is much larger due to our inability to determine the value of $\phi$. Lastly, the fit shows the 0-$\pi$ transition thickness for NiFeMo to be 2.25 $\pm$ 0.1 nm. A more detailed analysis of this sample series and data can be found in [57].

All these properties are informative to determine whether this material should be further pursued for JMRAM devices. The total critical current that can get through the junction must be above 100 $\mu$A. So the "starting height" of the critical current, $V_0$, and the steepness of its decay, $1/\xi_{F1}$, are desired to be large and small respectively. You don't want the 0-$\pi$ transitions to be too close together, which is related to $\xi_{F2}$, or small variation in the material thickness will cause drastic changes in the critical current. The exact value of the 0-$\pi$ transition is also important. If it is too thin, the magnetic properties of the material will likely degrade, but if it's too thick, it might suppress the critical current. It is a hard game to play to try and find materials that fit all these criteria. After careful consideration of NiFeMo, we decided that it's magnetic and superconducting properties were inferior to plain NiFe despite our hopes that the lower magnetization would give NiFeMo the advantage. Table 6.2 presented later in this chapter shows the fit parameter comparisons for these materials.

## 6.2 NiFe/FeMn (pinned NiFe)

Based on the positive SQUID magnetometry results for the NiFe/FeMn (pinned NiFe) discussed in the previous chapter, we decided to investigate this material stack in Josephson junctions to determine how much critical current is lost due to the FeMn layer. Though there are two magnetic layers in this system, I chose to report them here in the single F layer chapter since in a JMRAM device, they would act together as the fixed layer. This junction series had the structure [Nb(25)/Al(2.4)]$_3$/Nb(20)/Cu(5)/NiFe(x)/ FeMn(y)/Cu(5)/Nb(20)/Au(15)/Nb(150)/Au(10). The x/y thickness pairs examined were 2.0/1.0, 1.5/1.0, 1.0/1.5, and 1.5/1.5 with all thicknesses in nm. The junctions were patterned into ellipses with an aspect ratio of 2.5 and an area of 0.5, 1, or 2 $\mu$m$^2$.

Fraunhofer patterns were measured for at least two junctions on each chip in the series with no initialization. Figure 6.4 shows three of these Fraunhofer patterns for junctions with 2.0 nm NiFe and 1.0 nm FeMn. The top left pattern is a 2 $\mu$m$^2$ area junction, the top right pattern is a 1 $\mu$m$^2$ area

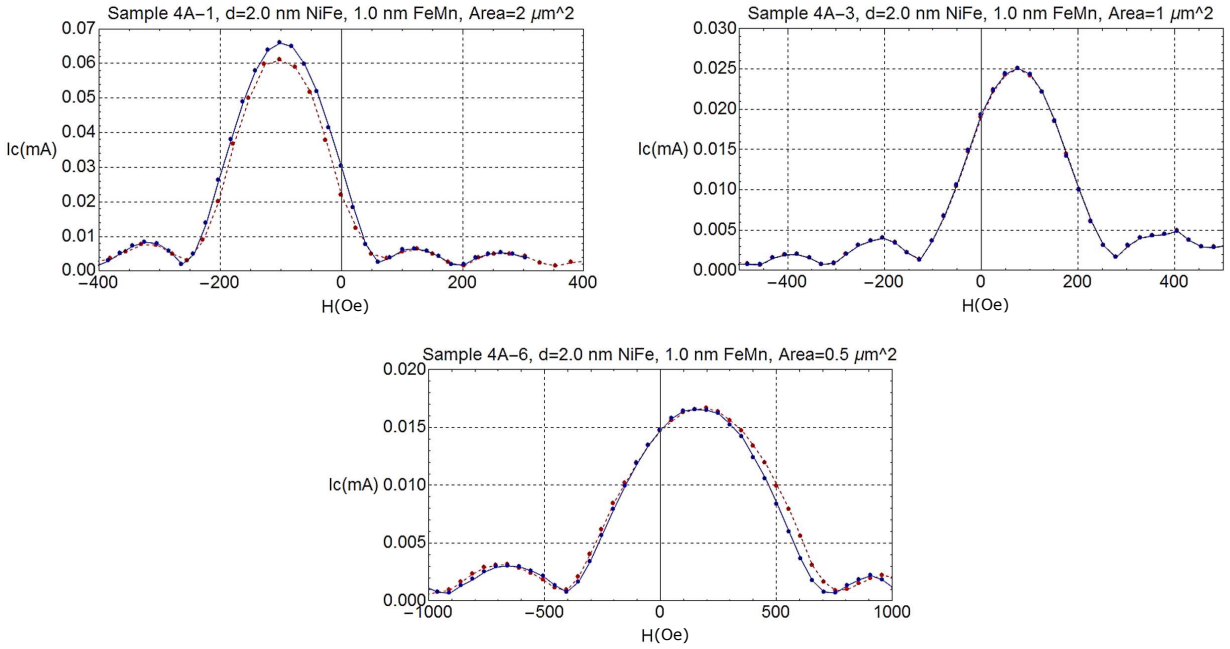


Figure 6.4 **Fraunhofer patterns for NiFe/FeMn Josephson junctions** All three patterns were measured from the same chip which had 2.0 nm NiFe and 1.0 nm FeMn. The upper left pattern is from a junction with 2 $\mu$m$^2$ area, the upper right pattern is from a junction with 1 $\mu$m$^2$ area, and the lower pattern is from a junction with 0.5 $\mu$m$^2$ area. The blue data were collected by sweeping the field in the positive direction and the red data by sweeping in the negative direction. Unlike the NiFeMo Fraunhofer patterns, these show no hysteresis with field sweep direction and the horizontal shift is not consistent from junction to junction in direction or magnitude.

junction, and the lower pattern is a 0.5 $\mu$m$^2$ area junction. In all plots, the blue data is sweeping the field in the positive direction and the red data is sweeping the field in the negative direction. Compared to the Fraunhofer patterns for NiFeMo, there are some clear differences. First, there is no hysteresis in the pattern with sweep direction. The positive and negative sweep Fraunhofer patterns essentially line up with each other. This indicates that there is no magnetic switching of the layers in the junction even up to $\pm$ 1000 Oe. There also seems to be no systematic pattern to the horizontal shift in the Fraunhofer patterns. Though the junction area is changing for each pattern, you would expect at least the sign of the shift to be the same between these three junctions, but because the blocking temperature is below room temperature, this is not the case. Since these junctions were not cooled in a field, the virgin magnetic state was 'frozen' into place when the sample was dipped into the measurement dewar. Hopefully, shape anisotropy would cause the

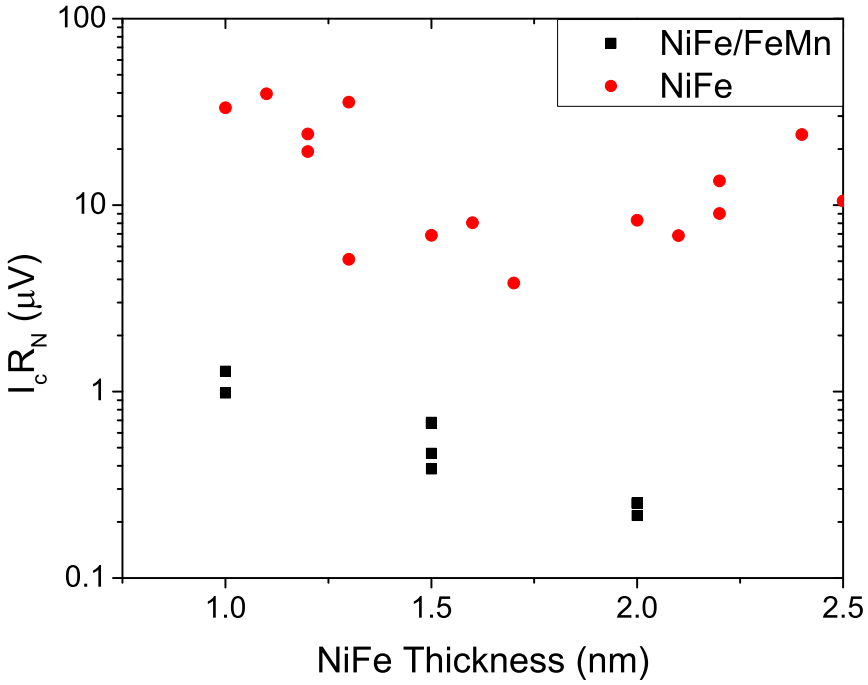


Figure 6.5 **$I_cR_N$ comparison for Josephson junctions with NiFe and NiFe/FeMn**

magnetization to be primarily along the ellipse long axis, but the direction is seemingly arbitrary. The possibility of non-uniform magnetization could also be artificially lowering the peak critical current value in the Fraunhofer pattern, so these values can only be taken as a lower limit.

| FeMn \ NiFe | 1.0 nm | 1.5 nm | 2.0 nm |
|---|---|---|---|
| 1.0 nm | xx | 680 nV | 240 nV |
| 1.5 nm | 1130 nV | 460 nV | xx |

Table 6.1 **Average $I_cR_N$ values for NiFe/FeMn bilayer junctions** This table shows the average $I_cR_N$ values (in nV) for samples with NiFe/FeMn thicknesses of 1.0/1.5, 1.5/1.0, 1.5/1.5, and 2.0/1.0 with all thicknesses reported in nm.

Table 6.1 shows the average $I_cR_N$ values for the different NiFe/FeMn thickness combinations tested. Interestingly, changing the NiFe thickness by 0.5 nm seems to have a larger impact on the total $I_cR_N$ than changing the FeMn thickness by 0.5 nm. But either way, the total $I_cR_N$ for this fixed layer is significantly smaller than that of junctions with only a NiFe layer. Figure 6.5 shows that the separation between the $I_cR_N$ values is over an order of magnitude. Though the NiFe/FeMn

| Material | $V_0$ ($\mu$V) | $\xi_{F1}$ (nm) | $\xi_{F2}$ (nm) | 0-$\pi$ Thickness (nm) | $I_cR_N$ $\pi_{peak}$ ($\mu$V) |
|---|---|---|---|---|---|
| NiFeMo | $150 \pm 50$ | $0.48 \pm 0.04$ | $0.955 \pm 0.01$ | $2.25 \pm 0.1$ | 0.25 |
| NiFe | $70 \pm 20$ | $1.50 \pm 0.38$ | $0.58 \pm 0.10$ | $1.76 \pm 0.05$ | 16.5 |
| NiFeCo | $30 \pm 6$ | $1.10 \pm 0.16$ | $0.48 \pm 0.03$ | $1.16 \pm 0.02$ | 5.9 |

Table 6.2 **Comparison of fit parameters from 0-$\pi$ transition plots for NiFeMo, NiFe, and NiFeCo** Additionally, the last column shows the $I_cR_N$ value for the peak of the $\pi$ state for each material. This serves as a rough comparison of the materials taking into account all three fit parameters. For JMRAM devices, we generally want this value to be maximized.

has great magnetic properties as a fixed layer, this drastic reduction in critical current makes it of little use for the JMRAM project. S/F/S junctions with only NiFe will be further discussed in the next section.

## 6.3 NiFe and NiFeCo

Similar sample fabrication and measurements to those done for NiFeMo and NiFe/FeMn were carried out by Joseph Glick on free layer NiFe and fixed layer NiFeCo (with help from Dr. Mazin Khasawneh, Dr. Eric Gingirch, and myself on the NiFe data). Thicknesses ranging from about 1 - 3.5 nm were explored for both materials. I will not go into detail on the single junction measurements of these materials, but I would like to share a summary plot of the $I_cR_N$ vs thickness for each material as well as a chart of the fit parameters for a comparison of these materials.

Figure 6.6 shows the $I_cR_N$ vs F layer thickness for NiFe and NiFeCo. There is significantly more scatter in the NiFe data, probably due to the fact that many different people were involved in the fabrication and measurement of those samples which spanned several sputtering runs. Nevertheless, fits were performed to both sets of data to determine the 0-$\pi$ transition thicknesses, $V_0$, $\xi_{F1}$, and $\xi_{F2}$ values. These fit parameters are summarized and compared with those from NiFeMo in Table 6.2. Though NiFeMo has the highest $V_0$, it also has the steepest exponential decay, characterized by the lowest $\xi_{F1}$ value, which quickly decreases the critical current through the junction as the NiFeMo thickness increases. NiFeCo shows nicer magnetic properties, but compared with Ni, which has been used historically in many junction stacks measured by the group, it highly

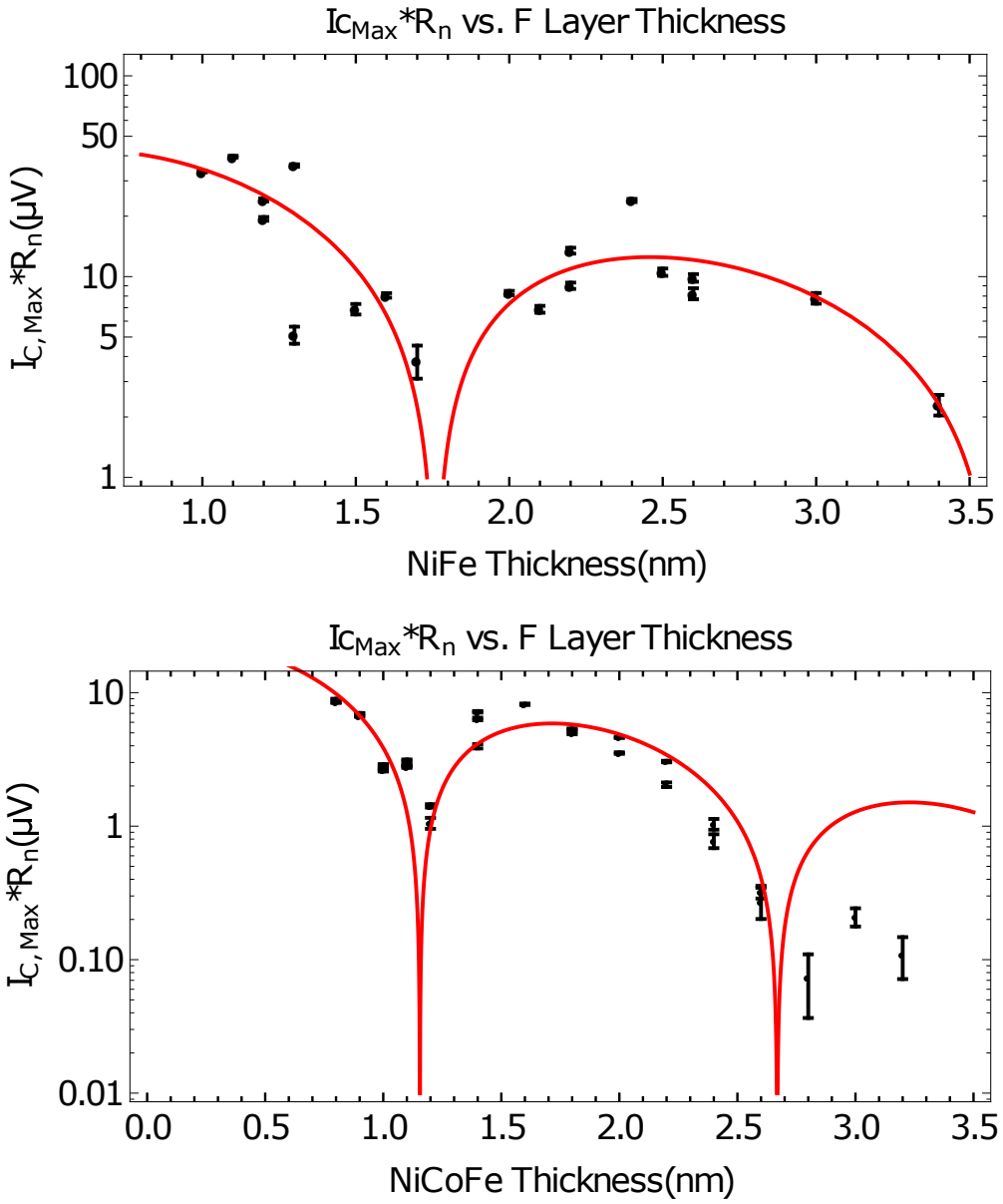


Figure 6.6 **$I_cR_N$ vs material thickness for NiFe and NiFeCo** This plot shows the $I_cR_N$ vs material thickness for NiFe and NiFeCo, primarily measured by Joseph Glick. The $I_cR_N$ values are taken from the peak of the Fraunhofer pattern as extrapolated from fits. The whole plot is fit in red with the same equation as the NiFeMo data in the previous section.

suppresses the critical current with a low $V_0$ value and a relatively steep critical current decay. The fit parameters for these materials can be roughly combined by comparing the $I_c R_N$ value of each material at the peak of the $\pi$ state. For JMRAM devices, we generally want this value to be maximized. By this comparison, you can see that NiFe is highly advantageous compared to the other two materials. Spin-valve junctions using free layers of NiFe and fixed layers of Ni and NiFeCo will be discussed in the next chapter.

# CHAPTER 7

# SINGLE JUNCTION SPIN VALVE DEVICES

This chapter will detail measurements of single pillar Josephson junctions that contain two ferromagnetic layers, making them spin valve devices. A junction such as this will ultimately serve as the phase controllable S/F/S junction in the JMRAM memory cell, but though a single junction is all that is needed to create a phase change, we are not set up to measure phase changes in a single junction. For that, we need to measure the relative phase between two spin valve junctions in a SQUID, which will be discussed in Chapter 8. Many other useful pieces of information can be obtained from transport measurements of single junction spin valves, such as switching field values for the two layers, the amount of critical current that can travel through the junction when the magnetizations of the two layers are oriented parallel and antiparallel, and the field values required to saturate each magnetic layer. Also, since there is only one junction being measured, the results are easier to interpret than those comparing two junctions with a more complex circuit design.

If a series of layer thicknesses is considered, these measurements can also be used to inform future devices on the F layer thickness range that will show 0-$\pi$ phase switching. As is shown in Figure 2.12, we are attempting to control the thicknesses of our F layer materials such that one layer is at its 0-$\pi$ transition thickness and the other is thinner than its 0-$\pi$ transition thickness, leading to a junction whose phase can be changed between 0 and $\pi$ when the magnetizations of the two F layers are oriented antiparallel (AP) or parallel (P) to each other. As the figure shows, this is characterized by equal critical current through the junction in the P vs AP states. Technically, it is the peak critical current of the junction (from the peak of the Fraunhofer pattern) that should be equal, but because of the shifts in the Fraunhofer pattern due to the magnetic material in the junctions, the peak value will be shifted away from zero field in the opposite direction as the net junction magnetization. We hoped that the small size of these junctions, which increases the width of the Fraunhofer pattern, would cause the zero-field and peak critical current values to be similar. This chapter will detail several series of spin valve measurements where one of the F layers is

held at a constant thickness and the other is systematically varied. When the critical current of the junction in the P or AP state dips to zero, this indicates crossing into a new phase lobe on the $I_c$ vs thickness plot, so the thickness region between the two zeros of $I_c^P$ and $I_c^{AP}$ and will support 0-$\pi$ phase transitions. The same types of measurements were performed for all series, but they will only be described in detail in the first section. Systems with NiFe/NiFeCo and NiFe/Ni will be discussed.

## 7.1 NiFe(1)/NiFeCo(x) Spin Valves

The first set of spin valve samples that I studied contained NiFe as the free layer and NiFeCo as the fixed layer. SQUID devices for phase sensitive measurements had already been made and measured using these materials, but nominally the same samples made in different sputtering runs showed different results, as will be discussed in Chapter 8. We decided that our chosen thicknesses must put one of the states very close to a 0-$\pi$ phase transition. This study varying the NiFeCo thickness was intended to determine a better thickness range to use in future SQUID devices.

These samples had the following structure: $[Nb(25)/Al(2.4)]_3$/Nb(20)/Cu(5)/NiFe(1)/Cu(10)/ NiFeCo(x)/Cu(5)/Nb(5)/Au(15)/Nb(150)/Au(10) where x = 0.9 - 1.5 nm in 0.1 nm steps. The samples were grown in a field with a square magnet placed in the center of the sputtering holder, and processed as described in Chapter 3 into ellipses with 0.5 $\mu m^2$ area and an aspect ratio of either 2.2 or 2.8. Major and minor loop zero-field measurements were taken of all samples. In a major loop, both magnetic layers switch (both the NiFe and the NiFeCo) back and forth, whereas in a minor loop only the free layer (NiFe) switches back and forth. To perform these measurements, first the magnetizations of the two layers must be initialized in one direction. I chose to initialize in the negative direction with a -400 to -600 Oe field. The major loop was collected by measuring IV curves starting at zero field, then slowly stepping up this 'set' field and returning to zero field to measure the next IV curve. The IV curves were fit with the standard overdamped relation given in equation 2.16 and the resulting critical current was plotted vs the set field. The goal of these

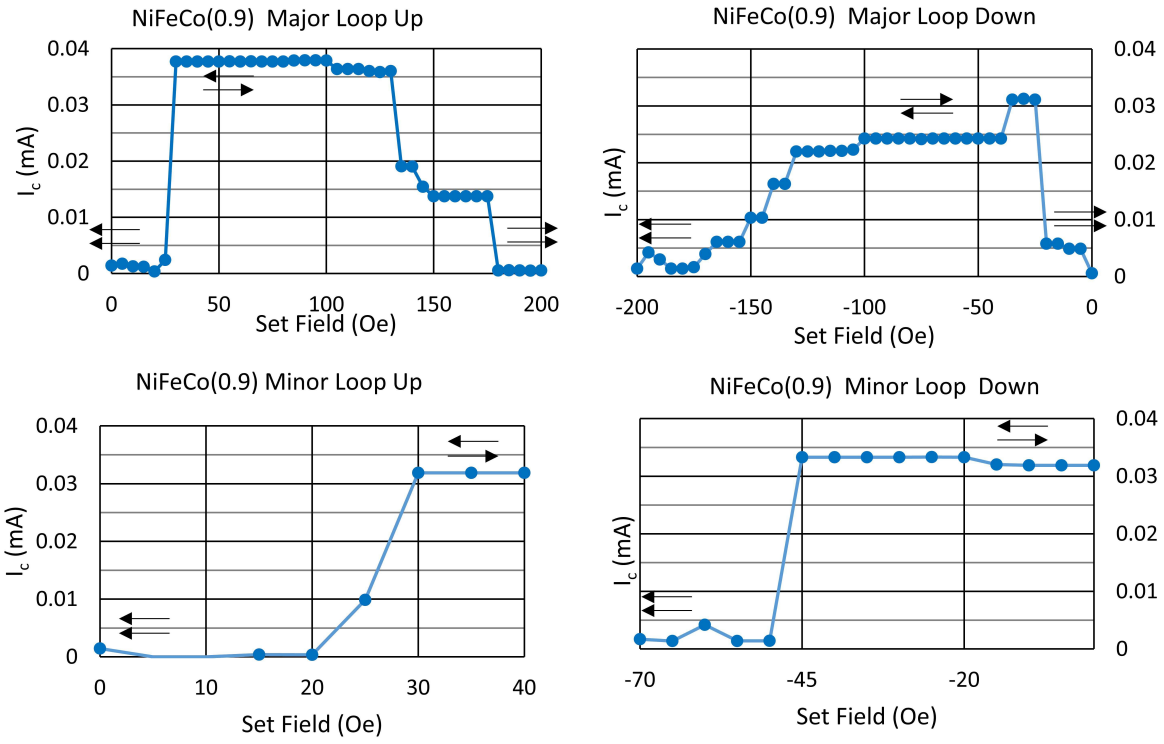


Figure 7.1 **Representative Zero-Field Measurements of NiFe(1)/NiFeCo(x) Spin Valve** Here, x = 0.9 nm NiFeCo. All points are the critical current fit from an IV curve measured at 0 field after the appropriate 'set' field was applied. The black arrows indicate the magnetization direction of the NiFe (lower arrow) and NiFeCo (upper arrow).

measurements was to determine the critical current of the junction at zero field in the P and AP states and to compare their values as the thickness changes and also to see the switching and saturation fields for both F layers. The maximum magnitude of the 'set' field before measuring in the opposite field direction determines whether a major or minor loop is collected. A typical minor loop extended to $\pm$ 50 Oe taking 5 Oe steps, and a typical major loop continued until the hard magnetic layer was fully saturated (up to about $\pm$ 200 Oe for this NiFeCo series). After measuring several of the thinner NiFeCo samples which showed very low critical current in the P state, I started to also measure the Fraunhofer pattern for each sample to get a better feel for the shift of the central peak and to observe any deviations in its shape from what was expected.

Figure 7.1 shows a representative zero-Field measurement. The upper plots show the major loop and the lower plots show the minor loop. In the two right hand plots, labeled as the 'up'

sweep, the sample was initialized fully in the negative direction and the field was swept in the positive (right) direction. In the right hand plots, the field sweeps in the negative (left) direction and follows directly after the 'up' sweep. These are labeled as 'down' sweeps. The black arrows indicate the magnetization direction of the NiFe (lower arrow) and NiFeCo (upper arrow). The major loop data indicate the switching of both magnetic layers. The "Major Loop Up" plot shows the NiFe switching from a low critical current in the P state to a higher critical current in the AP state in the field range of 20-30 Oe. The critical current and therefore the magnetic configuration remain stable until 100 Oe when we see the NiFeCo begin to switch over a range of field values ending at 185 Oe and including several intermediate switching states. Continuing this major loop by sweeping the field in the negative direction, as shown in the "Major Loop Down" plot, we see that the NiFe switching is now less abrupt and settles to a stable AP state with a lower critical current then seen during the 'up' sweep. The NiFeCo still switches over a wide range of fields including many intermediate states.

The minor loop plots on the lower half of the figure show that the NiFe switches over a small field range with asymmetry in the switching field with the field sweep direction. Features from these zero-field measurements that repeated themselves sample to sample include the presence of intermediate switching states, switching fields for the NiFe below 50 Oe, saturation of the NiFeCo by around 200 Oe, and larger critical current values when the sample was in the AP state vs the P state. This last point may be due to magnetic changes suppressing the critical current near zero field and will be discussed momentarily. There was also no discernible difference between measurements of junctions with an aspect ratio of 2.2 compared with those with an aspect ratio of 2.8. It was expected that the lower aspect ratio junction would show lower NiFe switching fields but the data showed no clear trend between aspect ratio and switching field.

The low critical current values observed in several P state zero-field measurements led to additionally measuring the Fraunhofer patterns for subsequent junctions. We expect some horizontal shift in the Frauhnofer pattern due to the magnetization of the F layers themselves, and this effect will cause larger shift amounts in the P state. However, given the small size of these junctions and

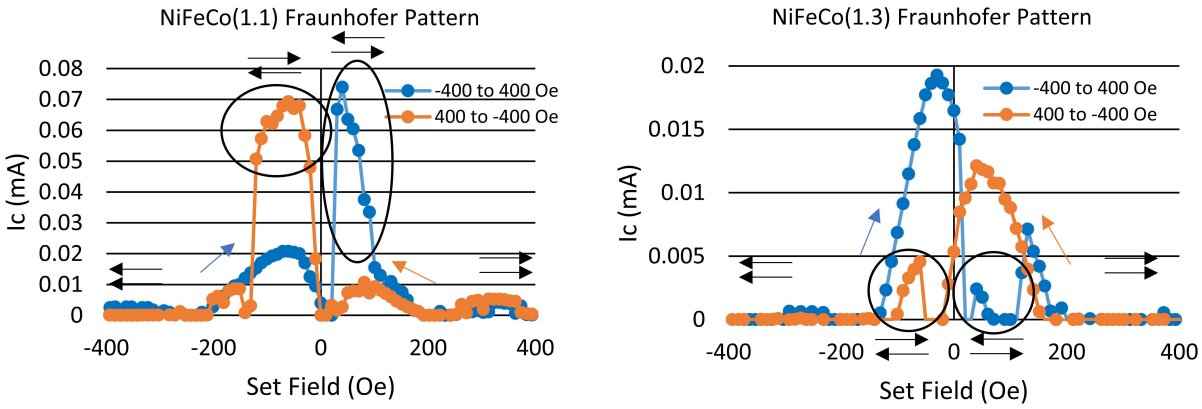


Figure 7.2 **Representative Fraunhofer Patterns for NiFe(1)/NiFeCo(x) Spin Valve** The blue data sweep from negative to positive field values and the orange data sweep from positive to negative field values. The circled regions indicate where the junction is switching into and out of the antiparallel magnetic configuration. The black arrows indicate the magnetization direction of the NiFe (lower arrow) and NiFeCo (upper arrow).

taking into account the shift amounts observed in single F layer junctions, we thought that even in the P state, the zero-field measurement would be close to the Fraunhofer pattern's central peak value. As can be seen in Figure 7.2, this is not always the case. This figure shows two Fraunhofer patterns collected from samples with NiFeCo thicknesses of 1.1 and 1.3 nm. The blue data is collected by sweeping the external 'set' field from negative to positive values and the orange data is collected subsequently by sweeping the magnetic field from positive to negative field values. The black arrows indicate the magnetization direction of the NiFe (lower arrow) and NiFeCo (upper arrow). The circled part of the pattern indicates the portion where the junction is suspected to be in the AP state. The data here are measured in the presence of the 'set' field. The ending field values of $\pm$400 Oe are sufficient to saturate the NiFe and NiFeCo layers as can be seen from the zero-field measurements. Because of this, we expect the Fraunhofer shift to always be larger in the P vs AP state and for the P state pattern to always have its central peak occur at a field opposite in sign from the layers' magnetization direction. It is, therefore, curious to see that the blue (orange) data, which should have initially negatively (positively) magnetized layers, appears to have a peak Fraunhofer pattern value also at negative (positive) field. This indicates that there is some magnetic change

in the junctions before zero field is reached that causes a downturn in the junction critical current and a dramatic suppression of the critical current for the "P" state from zero-field measurements (P is now in quotes because if there is a magnetic change, the magnetizations of the two layers are no longer parallel). This critical current suppression of the "P" state is observed in all Fraunhofer pattern measurements and means that our zero-field measurements of the "P" state do not convey information about the peak Fraunhofer pattern value. A possible culprit is magnetostatic coupling between the two magnetic layers which favors the AP state and could cause the magnetic state to begin to change before zero field is reached. Some patterns also showed strange rapid oscillations of the critical current with H near zero field indicating magnetic instability within the junction. If the downward turn of the critical current is neglected and the peak of the Fraunhofer is projected to the proper side of zero field, it appears that the P state has a lower maximum critical current than the AP state in the 1.1 nm NiFeCo sample where as the opposite is seen in the 1.3 nm NiFeCo sample. Though some Fraunhofer patterns are difficult to interpret, overall this switch in P vs AP critical current ratio occurs nominally at 1.3 nm NiFeCo indicating a 0-$\pi$ transition thickness around this value.

The summary plot of zero-field $I_cR_N$ values in the "P" and AP state vs NiFeCo thickness is shown in Figure 7.3. As stated previously, the "P" state values represent a suppressed critical current, not the peak value, so solid conclusions cannot be drawn from this plot. However, even looking at the AP state $I_cR_N$ values, they are significantly lower than those needed for JMRAM applications, which on top of the other magnetic issues make this system undesirable for future study. Additionally, these samples used rougher spacer and buffer layers of Cu(5) and Cu(10). If this system was transitioned to use smoother normal metal layers, the switching field of the NiFeCo might begin to overlap with that of the NiFe. A fixed layer with a larger switching field and lower magnetization are desired to give tolerance to the allowed switching fields and reduce low field magnetic issues caused by dipolar coupling. This led us back to studying the NiFe/Ni system further, now utilizing smoother spacer and buffer layers and investigating thicker Ni layers than used in previous studies.

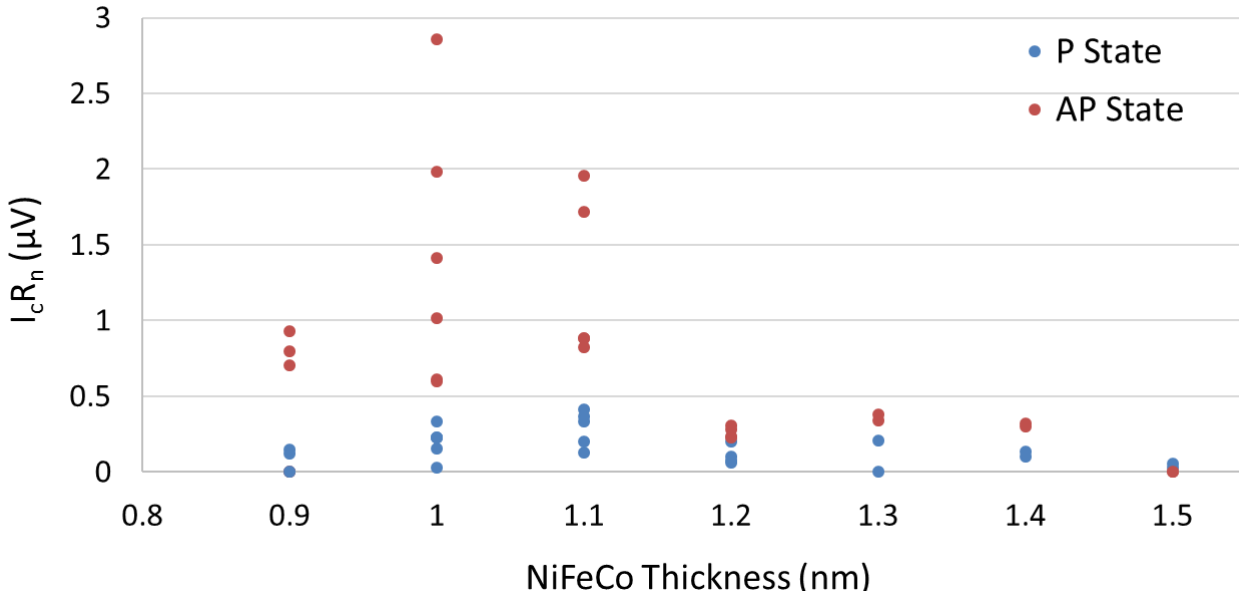


Figure 7.3 **Zero-Field $I_cR_N$ in "P" vs AP State for NiFe(1)/NiFeCo(x) Spin Valves** The AP state data somewhat follow the expected trend, but in comparison, the "P" state has a considerable smaller critical current and is possibly being artificially reduced at zero field as discussed in the text.

## 7.2 NiFe(x)/Ni(2) Spin Valves

Our group has historically used Ni in Josephson junctions due to the high critical current obtained through junctions containing this material compared with all other materials that have been investigated by the group. Ni layers between 1.0 and 1.5 nm thickness were found to require 1000 - 2000 Oe switching fields, making it a hard layer candidate [45]. In Chapter 8, phase-sensitive measurements will be discussed from a system using NiFe(1.5)/Ni(1.2). To improve that system we wanted to investigate thicker Ni layers in hopes of improving the Ni magnetic properties. Since we were unable to measure the 0-$\pi$ transition thickness of Ni, this spin valve study with NiFe(x)/Ni(2) was carried out to determine the range of thicknesses that should give 0-$\pi$ phase transitions.

The first version of this study used a Cu(2)/Al(7)/Cu(2) spacer layer between the NiFe and Ni layers. SQUID magnetometry results showed that this spacer layer was very smooth, as seen in Figure 4.5. Unfortunately, transport measurements revealed that the critical current is highly suppressed through this spacer layer and the majority of spin valve samples showed almost zero

critical current in either the P or AP states (depending on the NiFe thickness). In order to view systematic trends, a new set of samples was fabricated using our current "best" buffer and spacer layers of Cu(2) and Cu(4) respectively. These layers were found to show the best magnetometry results of spin valve samples.

The spin valve samples in this series had the following structure: $[Nb(25)/Al(2.4)]_3$/Nb(20)/ Cu(2)/NiFe(x)/Cu(4)/Ni(2)/Cu(2)/Nb(5)/Au(15)/Nb(150)/Au(10) where x = 1.1 - 1.8 nm in 0.1 nm steps. Three additional samples were also made with the bottom Cu(2) replaced with Ru(2) and NiFe thicknesses of 1.3, 1.5, and 1.7 nm. The samples were patterned into ellipses with a 0.5 $\mu m^2$ area and an aspect ratio of 2.5. Fraunhofer patterns and zero-field measurements were performed to determine the relative P vs AP critical currents for this series, to investigate the switching properties of the thicker Ni and NiFe, and to compare the results for the Cu vs Ru seed samples.

Figure 7.4 shows a representative Fraunhofer pattern and set of zero-field measurements for a sample with 1.3 nm NiFe. This junction was intialized with a positive field. Part a) shows the Fraunhofer pattern, b) and c) show the major loop zero-field measurements, and d) and e) show the minor loop zero-field measurements. The black arrows indicate the magnetization direction of the NiFe (lower arrow) and Ni (upper arrow). The blue data in the Fraunhofer pattern sweep in the positive direction and the orange data sweep in the negative direction, as indicated by the blue and orange arrows. The black circles enclose the data where the junction is assumed to be in the AP state. In parts b) and d) the field sweeps in the negative direction and in parts c) and e) the field sweeps in the positive direction. Looking at all the minor loop data, the NiFe was found to switch its magnetization direction over a range of fields about 5 - 10 Oe wide, typically completing the switching process before 50 Oe. We would expect the NiFe to have a lower switching field when switching from the P to AP state than when switching from the AP to P state since the dipolar coupling should make the AP state more stable. However, while this set of samples did show some switching field asymmetry between the two switching directions, the AP to P switch did not show systematically lower switching fields for all samples. The major loop data show that the Ni switches over a much larger field range starting between 300 and 400 Oersted and completely

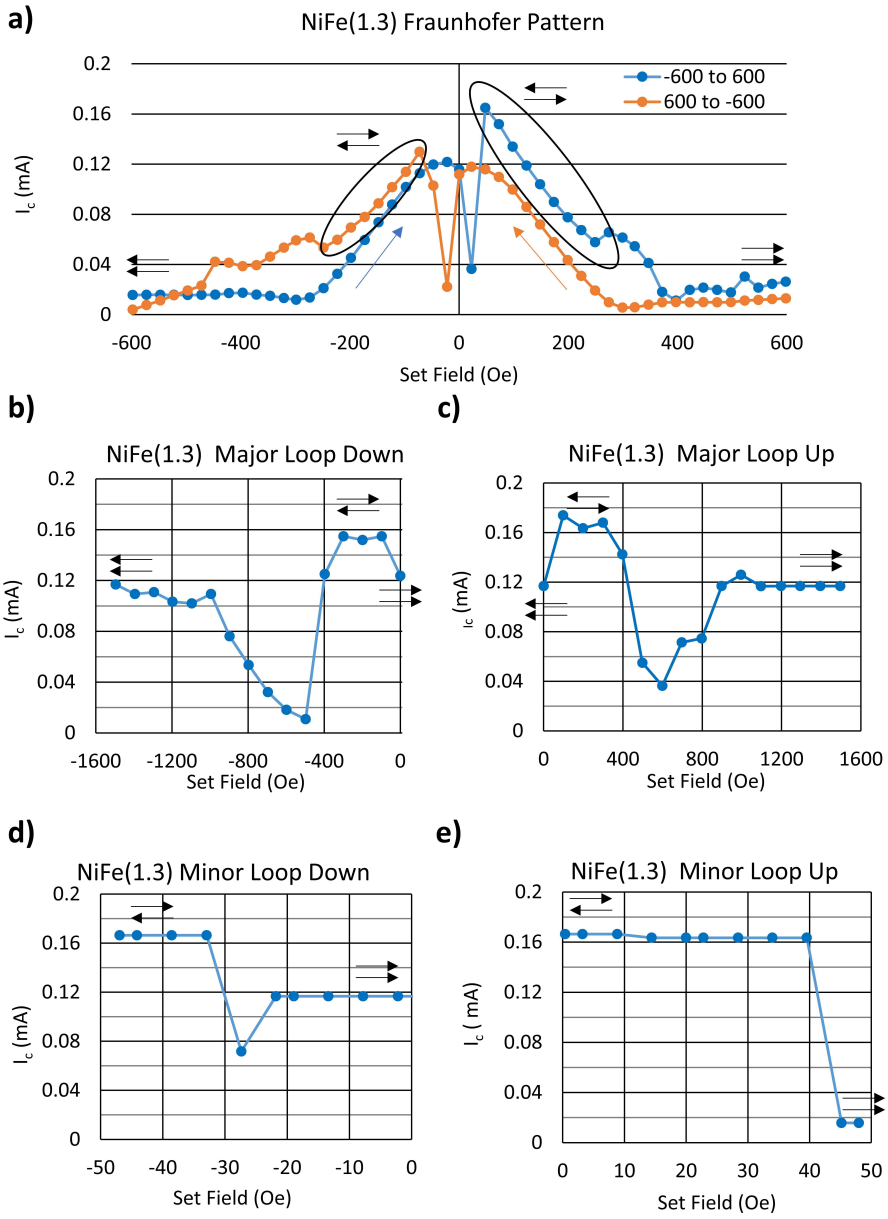


Figure 7.4 **Representative Fraunhofer Pattern and Zero-Field Measurement for NiFe(x)/Ni(2) Spin Valve Series** The black arrows indicate the magnetization direction of the NiFe (lower arrow) and Ni (upper arrow). This sample was initialized with a positive field. Part a) shows the Fraunhofer pattern with blue data advancing in the positive field direction and orange data advancing in the negative field direction, as indicated by the blue and orange arrows. The black circled regions indicate where the junction is believed to be in the AP state. Previous to this region, the junction was in the P state, and after, the Ni is switching over a large field range. Parts b) and c) show a major loop zero-field measurement with both magnetic layers switching and parts d) and e) show a minor loop zero-field measurement where only the NiFe layer switches back and forth.

saturating by 1000 - 1500 Oe. This saturation field is much lower than the $\pm$2600 Oe that we used to initialize the 1.2 nm Ni layers in the past, which is an advantage of this 2.0 nm Ni layer.

The Fraunhofer pattern in Figure 7.4 part a) shows several distinctive features. These features appear symmetrically in both sweep directions. The P state part of the pattern should have its peak value at a field with the opposite sign as the layers' magnetizations. Similarly to the NiFeCo samples, this is not the case and there is a premature downturn of the junction critical current when approaching zero field. Additionally, many patterns measured in this series showed one point with a significantly lower critical current while the NiFe was switching. This feature is occasionally captured in the zero field measurements, such as in the P state minor loop critical current shown in Figure 7.4 part e). Here, a critical current of about 0.12 mA is expected from the Fraunhoffer pattern but the junction locks into a state with much lower critical current. The Ni was not fully saturated by the $\pm$600 Oe used to measure the Fraunhofer pattern, so the sample needed to be initialized with a $\pm$1500 Oe field before each sweep.

The $I_cR_N$ values in the P vs AP states for NiFe(x)/Ni(2) series are shown in Figure 7.5. These values are taken from the zero-field measurements and cross-checked with the Fraunhofer pattern data. The blue data show the AP state zero-field values for the Cu seed samples, the red data show the P state zero-field values for the Cu seed samples, the purple data show the P state zero-field values for the Ru seed samples, and the black data show the AP state zero-field values for the Ru seed samples. Two samples were measured for each thickness with the P and AP state data from the same junction sharing the same symbol (either circles or triangles). There is no significance to which junctions were assigned to be circles vs triangles. There is a clear systematic trend in the $I_cR_N$ values with the changing NiFe thickness. The Cu seed data show that $I_c^{AP}$ was continually rising while $I_c^P$ decreased to a minimum at 1.5 nm NiFe before rising again. These follow the expected trends given the simplified picture in Figure 2.12 where the pair phase accumulation $\phi^P = \phi_1 + \phi_2 = \frac{d_{F1}}{\xi_{F1}} + \frac{d_{F2}}{\xi_{F2}}$, $\phi^{AP} = \phi_1 - \phi_2 = \frac{d_{F1}}{\xi_{F1}} - \frac{d_{F2}}{\xi_{F2}}$, $d_F$ is the ferromagnetic layer thickness and $\xi_F$ is the coherence length in the ferromagnetic material. The theory of this system was further detailed in Chapter 2, but the case describing this data shown pictorially in Figure 7.6.

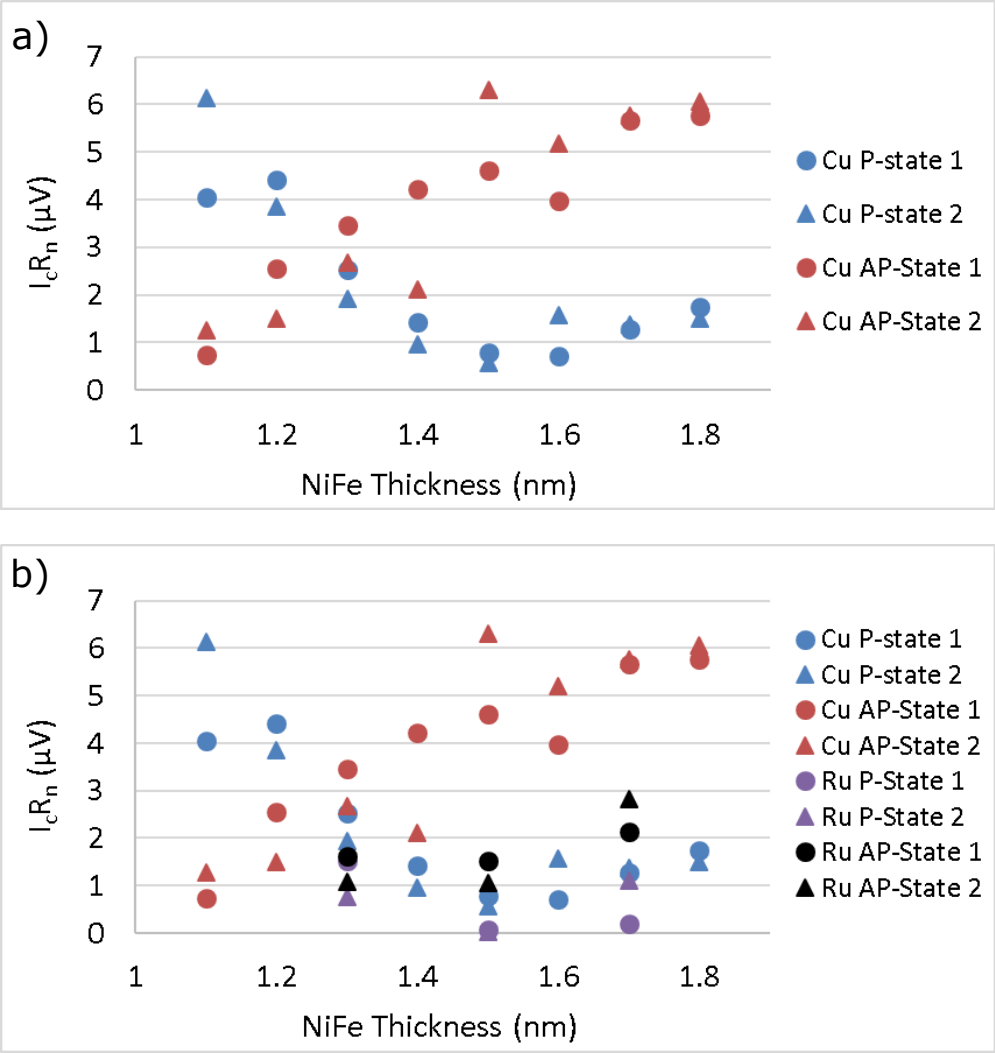


Figure 7.5 **Zero-Field $I_cR_N$ in P vs AP State for NiFe(x)/Ni(2) Spin Valves** Part a) shows only the samples with all Cu spacer and buffer layers while part b) includes the data from the samples with the Ru seed layer. The blue data show the AP state zero-field values for the Cu seed samples, the red data show the P state zero-field values for the Cu seed samples, the purple data show the P state zero-field values for the Ru seed samples, and the black data show the AP state zero-field values for the Ru seed samples. Red and blue circles or triangles of the same thickness represent the P and AP state data from the same junction. Two junctions were measured for each thickness. The data show a clear trend with the changing NiFe thickness. $I_c^P$ and $I_c^{AP}$ are closest to being equal between 1.2 and 1.3 nm NiFe indicating the optimal thickness for 0-$\pi$ switching, though anywhere between the minimum of $I_c^P$ and $I_c^{AP}$ should also produce a 0-$\pi$ phase change. Part b) shows that the Ru seed layer causes a drastic reduction of the P state critical currents as well as a difference in trend compared to the Cu seed samples.

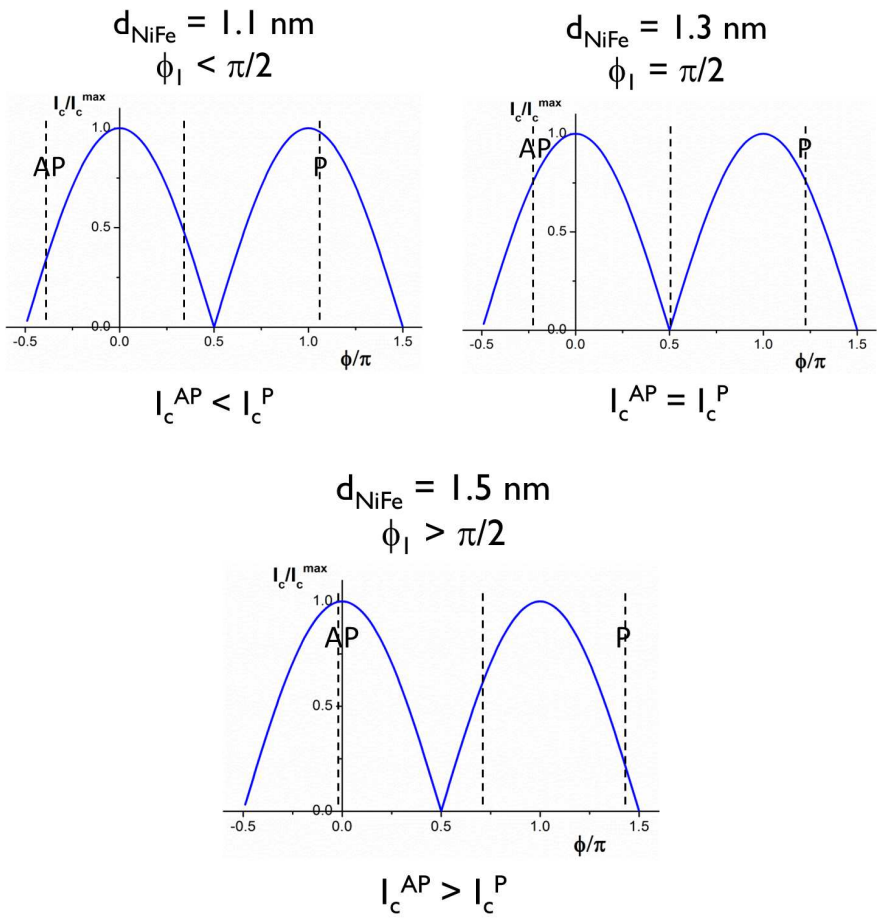


Figure 7.6 **Theoretical Description of $I_c^P$ and $I_c^{AP}$ Trends for NiFe(x)/Ni(2) Spin Valves** The data show that at low NiFe thicknesses $I_c^{AP} < I_c^P$ and at larger NiFe thicknesses $I_c^{AP} > I_c^P$. As shown in the figure, this picture is consistent with the case where the pair phase accumulation across the Ni, $\phi_2 = d_{F2}/\xi_{F2}$ is greater than half of the oscillation period.

In this figure, $\phi_1$ and $\phi_2$ represents the pair phase accumulation through the NiFe and Ni layers, respectively. In Figure 7.6, the location of $\phi_1$ is denoted by the unlabeled central dotted line and $\phi_2$ is the distance between this line and and the outer dashed lines, labeled P and AP. The data are explained by this picture where $\frac{d_{F2}}{\xi_{F2}} > \frac{\pi}{2}$ or the Ni thickness is greater than its 0-$\pi$ transition thickness. This gives $I_c^P > I_c^{AP}$ for smaller $d_F$ values and $I_c^{AP} > I_c^P$ for larger $d_F$ values. $I_c^{AP} = I_c^P$ around 1.25 nm NiFe so that is the desired thickness to use in 0-$\pi$ switching experiments, but samples with 1.1 -1.5 nm NiFe and 2.0 nm Ni should show 0-$\pi$ phase switching between the P and AP magnetic configurations. However, the theory is based on the maximum Fraunhofer pattern

values. The AP state data seems to have a small enough horizontal shift for the zero-field value to be a good estimate of the peak value, but this is not always the case for the P state data, so this analysis must be taken with a grain of salt. SQUID measurements are taken at zero field, so it is still very useful to know what kinds of critical currents we will see and balanced critical currents in the P and AP state will reduce asymmetries in the system. Part b) of Figure 7.5 includes the three sample thicknesses with the Ru seed on plotted together with the full series of Cu seed data. There was a dramatic reduction of the P state critical currents as well as a difference in trend compared to the Cu seed samples. To understand the full trend, more samples of different thicknesses would be needed, but since the critical current is so reduced, it is unlikely that this spacer layer will be pursued further.

## 7.3 NiFe(x)/Ni(1.6) Spin Valves

The analysis of the pair phase accumulation pointed to the Ni(2) layer being thicker than its 0-$\pi$ transition thickness. Thinner Ni would then increase the critical current at the crossover point where $I_c^P = I_c^{AP}$ since positioning on the theoretical curves shown in Figure 7.6 would be closer to the peaks. Having less ferromagnetic material in the junction should increase the critical current as well. To test this theory, and additional set of spin valve samples were fabricated and measured with NiFe(x)/Ni(1.6) where x = 1.1 - 1.8 nm. These samples had the same structure as those in the previous section, except Ni(1.6) instead of Ni(2.0): $[Nb(25)/Al(2.4)]_3$/Nb(20)/Cu(2)/NiFe(x)/Cu(4)/Ni(1.6)/Cu(2)/Nb(5)/Au(15)/Nb(150)/Au(10) where x = 1.1 - 1.8 nm in 0.1 nm steps. The sample with 1.2 nm NiFe had fabrication issues and was not able to be measured. Like the Ni(2) series, these junctions were patterned into ellipses with an area of 0.5 $\mu m^2$ and an aspect ratio of 2.5.

Fraunhofer patterns and zero-field measurements were performed on two junctions of every NiFe thickness. The overall shapes and features were very similar to those of the Ni(2) series. zero-field measurements showed NiFe switching below 50 Oe but with a bit more symmetry in minor loop switching fields from one sweep direction to the other. This thinner Ni did require a

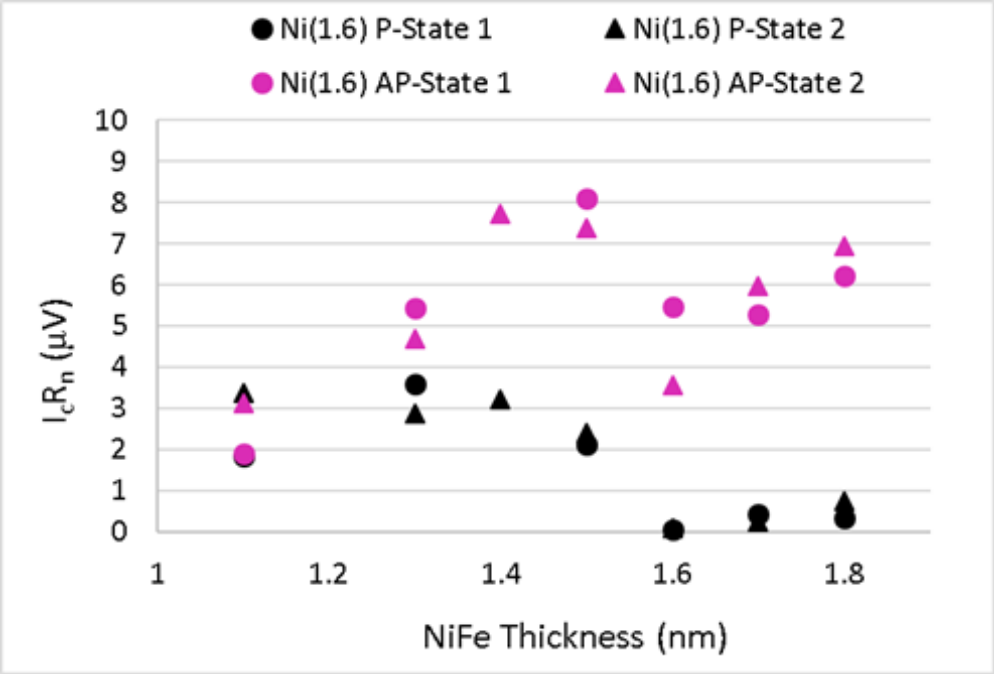


Figure 7.7 **Zero-Field $I_cR_N$ in P vs AP State for NiFe(x)/Ni(1.6) Spin Valves** The pink data show the AP state zero-field values and the black data show the P state zero-field values. Two junctions were measured for each thickness. Circles or triangles of the same thickness represent the P and AP state data from the same junction. Compared with the Ni(2) series, the critical current values are generally quite similar. Above 1.3 nm NiFe, the trend of $I_c^P < I_c^{AP}$ matches with the Ni(2) data, but both P and AP states have low critical current for the 1.1 nm sample. The 1.2 nm NiFe sample did not survive the fabrication process.

larger saturation field. The majority of the samples were saturated between 1300 and 1700 Oe but a couple samples took as much as 2500 Oe or as little as 1000 Oe to fully saturate. The Fraunhofer patterns were all of good quality with symmetric behavior with field sweep direction. They continued to exhibit the behavior of critical current reduction when approaching zero field during the NiFe switching process.

Figure 7.7 shows the summary for this series with the zero-field values of the $I_cR_N$ for the P and AP state vs the NiFe thickness. The pink data show the AP state zero-field values and the black data show the P state zero-field values. Two junctions were measured for each thickness. Circles or triangles of the same thickness represent the P and AP state data from the same junction. The trend of the data where the AP state has a higher critical current than the P state is reproduced

between the two series above 1.3 nm NiFe, though the trend is not as smooth in this Ni(1.6) series. Below 1.3 nm NiFe, it is difficult to tell what is happening since the 1.2 nm NiFe sample could not be measured and the 1.1 nm sample does not meet our expected values for $I_c^P$ and $I_c^{AP}$. From the Ni(2) series, we would expect that $I_c^P > I_c^{AP}$ at these low NiFe thicknesses. But in this series, they show very similar critical current values between the P and AP states with satisfactory Fraunhofer patterns and zero-field measurements indicating no issues with the junction.

Generally, the critical currents were not much higher than those in the Ni(2) series. There, the maximum $I_cR_N$ is about 6 $\mu$V and here it only gets up to about 8 $\mu$V. Additionally, though it is unclear exactly where $I_c^P = I_c^{AP}$, the $I_cR_N$ appears to be similar in value at this crossover point in both series. This means that if this system was used in SQUID devices where $I_c^P = I_c^{AP}$ for optimum 0-$\pi$ phase switching measurements, then there would not be an appreciable gain in the critical current of the devices. Since the saturation field for Ni(1.6) is also larger and the trend of the data for this series is not as nice as the Ni(2) series, SQUID devices were subsequently made with NiFe(1.25)/Ni(2). All SQUID device data will be detailed in the following chapter.

# CHAPTER 8

## SPIN VALVE SQUIDS

The ultimate goal of this work was to create a spin valve Josephson junction with two magnetic layers where the phase across the junction could be controllably changed between 0 and $\pi$ by changing the relative magnetization directions of the two magnetic layers from the antiparallel (AP) to parallel (P) state. Only a single junction is needed for this effect, but in order to make a phase-sensitive measurement to experimentally verify the phase change, we utilized a Superconducting QUantum Interference Device (SQUID) to measure the relative phase between two such junctions in a superconducting loop. In order to obtain a phase change in a single junction, the magnetic material switching fields and thicknesses must be carefully chosen. As described in Chapter 2, a free layer with a low switching field and a fixed layer with a larger switching field are needed. After initializing both magnetic layers in the same direction, only the free layer will switch its magnetization direction back and forth by 180° to put the junction in the P or AP state. These magnetic configurations alone, however, are not sufficient to produce phase switching. The magnetic materials must have the proper thicknesses relative to their 0-$\pi$ transition thicknesses. In our design, we wanted one layer close to its 0-$\pi$ transition thickness and the other layer thinner than its 0-$\pi$ transition thickness. Our initial results yielded from devices with NiFe(1.5)/Ni(1.2) and much of the discussion of that result in the following section comes from our publication of that work [28]. The experimental design and data analysis discussed in the following section will be applicable to all the devices detailed in this chapter. After incorporating optimization in base electrode and normal metal layer roughness, magnetic material properties, and device design, systems with NiFe(1.0)/NiFeCo(1.1) and NiFe(1.25)/Ni(2) were also investigated.

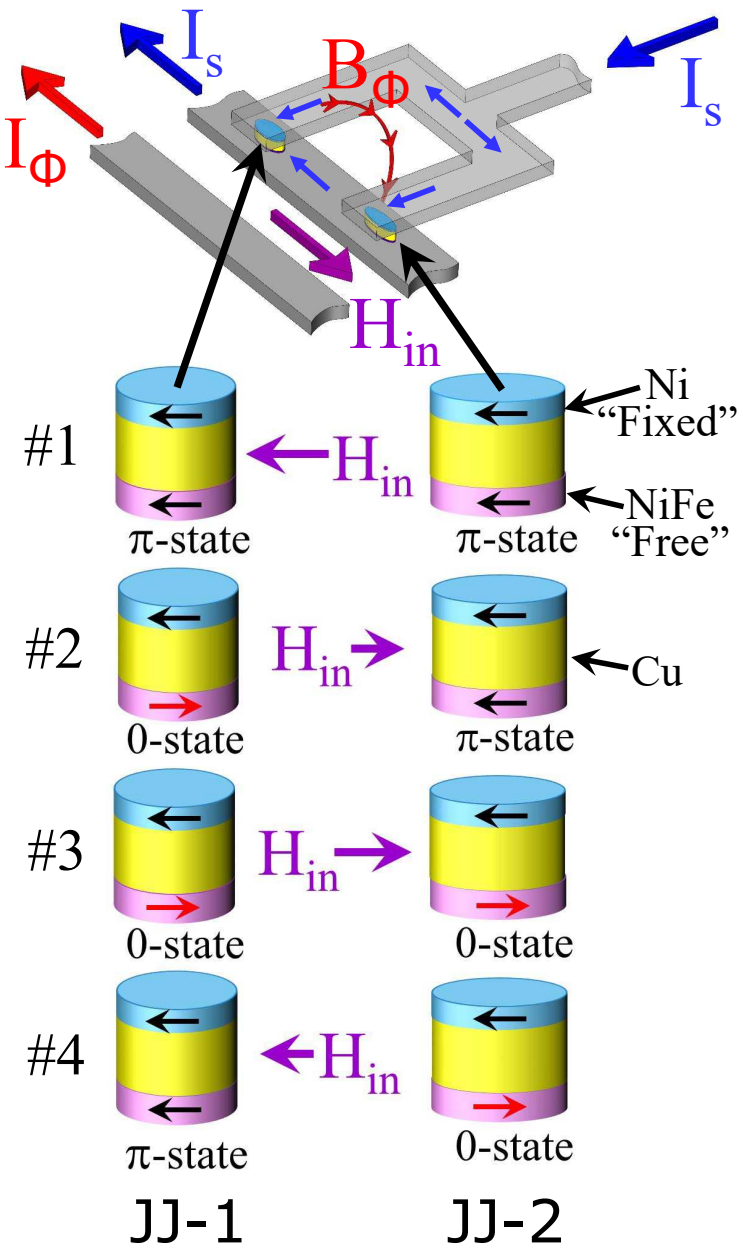


Figure 8.1 **Schematic Diagram of the Asymmetric SQUID Layout** Cartoons show the magnetization directions of the free and fixed layers for the four magnetic states discussed in this experiment. The colored arrows show positive directions of the measurement current, $I_s$, the applied in-plane magnetic field, $H_{in}$, the flux-line current, $I_\phi$ and the magnetic field produced by the flux line, $B_\phi$. The more circular junction is labeled as 'JJ-1' whereas the more eccentric elliptical junction is labeled as 'JJ-2.' The sizes of the four arrows in the four magnetic states depict the magnitude and direction of $H_{in}$ required to reach each state.

## 8.1 NiFe(1.5)/Ni(1.2) SQUIDs

The samples in this study had the following structure: [Nb(40)/Al(2.4)]$_3$/Nb(20)/Cu(5)/NiFe(1.5)/Cu(10)/Ni(1.2)/Cu(5)/Nb(20)/Au(15)/Nb(150)/Au(10). From the magnetic data shown in Chapter 6, the NiFe was the free layer with a thickness close to its 0-$\pi$ transition thickness and the Ni was the fixed layer with a thickness less than its 0-$\pi$ transition thickness. The SQUID design and layout are shown in Figure 8.1. The design includes two spin-valve junctions with the same material composition together in a superconducting loop. The junctions are patterned into ellipses with different aspect ratios to induce a difference in the free layer switching field and to provide a preferred easy axis magnetization direction along the long axis of the ellipse [74, 71]. The ellipses both had an area of 0.5 $\mu$m$^2$ and aspect ratios of 2.2 or 2.8 with the 2.2 aspect ratio junction corresponding to a lower switching field for the free layer than the 2.8 aspect ratio junction. The straight bottom lead and pitchfork-shaped top lead make up the SQUID and were both 5 $\mu$m wide. The inner dimensions of the resulting loop were 10 $\mu$m by 10 $\mu$m. The adjacent straight, long wire is 10 $\mu$m wide. In this measurement technique, sample current, $I_s$ is driven down the pitchfork top lead where it must split, with some current traveling down each leg of the loop, through a junction, and recombining through the straight bottom lead. The adjacent flux-line wire is driven with a current, $I_\phi$, which creates a magnetic field, $B_\phi$, that injects magnetic flux into the SQUID loop.

As described in Chapter 2, the critical current of a SQUID loop will oscillate with the flux through the loop. The junctions are labeled JJ-1 and JJ-2 for the more circular and more elliptical junctions, respectively. If both junctions are in the 0 phase state, this oscillation will be unaltered. If one junction is in the $\pi$ state and the other is in the 0 state, then the oscillation will be horizontally shifted by a phase of $\pi$ or equivalently, an extra flux of $\Phi_0/2$. If both junctions are in the $\pi$ state, the two additional phase shifts cancel out and the oscillation is unaltered. These phase states are achieved by manipulating the magnetization directions of the two F layers in the spin valve into the parallel or antiparallel configuration using an external in-plane magnetic field, labeled $H_{in}$ in Figure 8.1. This figure also shows the positive directions for $I_s$, $I_\phi$, $B_\phi$, and $H_{in}$ with the corresponding

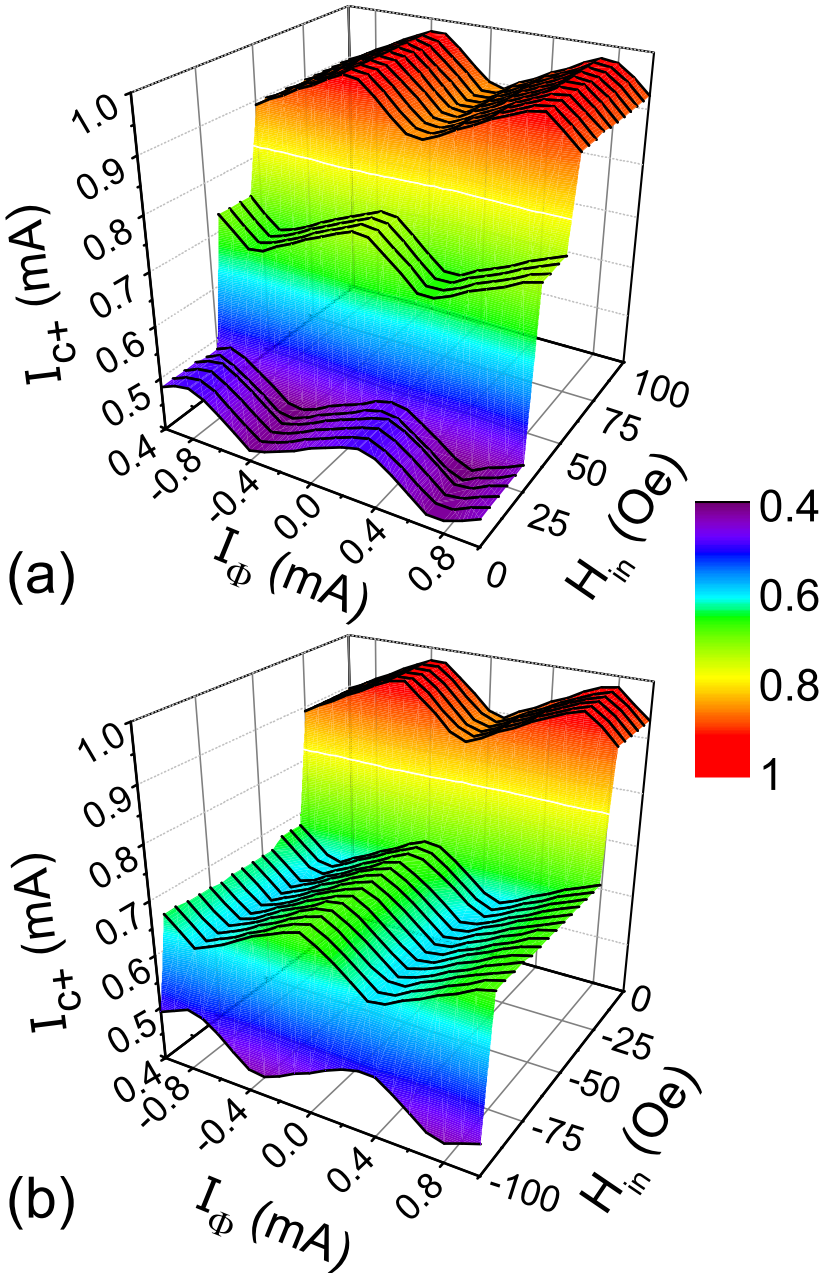


Figure 8.2 **Three-Dimensional Plots of Positive SQUID Critical Current, $I_{c+}$, vs Flux-Line Current, $I_\phi$, and In-Plane Set Field, $H_{in}$** After each value of $H_{in}$ is applied, the field is returned to zero and a scan of $I_{c+}$ vs $I_\phi$ is measured. Cross-sections at a fixed $H_{in}$ value show clear SQUID oscillations in $I_{c+}(I_\phi)$ with a period of about 1.1 mA, corresponding to one flux quantum, $\Phi_0$. Sudden jumps in the magnitude and phase of $I_{c+}$ indicate changes in the magnetic state of one of the Josephson junctions in the SQUID. The four total jumps correspond to the four magnetic states shown in the cartoons in Figure 8.1. a) shows the data for $H_{in} > 0$ and b) shows the data for $H_{in} < 0$. In both cases the data are taken with $|H_{in}|$ increasing in time.

arrows. Four distinct magnetic states can be accessed combining the P and AP states of the two junctions in the loop. They are shown in the cartoon below the SQUID layout in the figure with labels indicating the magnetization direction of the Ni and NiFe layers with black or red arrows and the expected phase state of the junctions with the P state corresponding to the $\pi$ phase state and the AP state corresponding to the 0 phase state.

These devices are mounted onto a quick dipper probe with a surrounding solenoid magnet and submerged in liquid helium for measurements. To start, we initialize the junctions into the $(\pi - \pi)$ state by applying a large in-plane field of $H_{in}$ = -2,600 Oe, which sets all four magnetic layers in the negative direction. The sample is then warmed above 10 K by raising the sample up out of the liquid helium to remove any trapped flux from the initialization process. We then measure, at zero field, a set of IV curves while varying the current, $I_\phi$, through the flux line to observe oscillations in the SQUID critical current as a function of applied flux. Critical currents are obtained by fitting the IV curves to the standard form for an overdamped Josephson junction given in equation 2.16. Note that the critical currents for the two polarities of applied current, $I_{c+}$ and $Ic-$, need not be the same. Next we apply a small 'set' field of $H_{in}$ = 5 Oe, return the field to zero, and repeat the scan of IV curves versus flux. We continue taking small steps in $H_{in}$, each time setting the field back to zero and repeating a full flux scan.

Figure 8.2 shows three-dimensional plots of $I_{c+}$ versus $H_{in}$ and $I_\phi$ as $H_{in}$ is stepped from 0 to 100 Oe. Cross-sections of the plot at fixed values of $H_{in}$ exhibit clear oscillations in $I_{c+}(I_\phi)$. As $H_{in}$ is varied, those cross-sections exhibit two large jumps, the first at $H_{in}$ = 30 Oe and the second at $H_{in}$ = 50 Oe. At each jump, the overall magnitude of the critical current changes, and the peaks in $I_{c+}$ shift along the flux axis. We identify the first jump with the NiFe free layer in the more circular JJ-1 switching its magnetization direction, so that the phase state of JJ-1 switches from $\pi$ to 0, thus changing the SQUID from the $(\pi - \pi)$ to the (0-$\pi$) state. The second jump signifies that the NiFe layer in the more elliptical JJ-2 has switched its magnetization direction, and is now also in the 0-state, so the SQUID is now in the (0–0) state. Figure 8.2 part b) shows similar data acquired for $H_{in} < 0$. Again, there are two jumps in the plot, the first occurring at $H_{in}$ = -35 Oe, putting the

SQUID in the ($\pi$-0) state, and the second at $H_{in}$ = -100 Oe, returning the SQUID to the ($\pi - \pi$) state as at initialization. Taken together, Fig. 2a, b corresponds to a major loop through all four accessible magnetic states of the system, where only the NiFe layer of each junction switches and the Ni in both junctions remains always in the initialization direction. The fact that the magnitudes of the switching fields for $H_{in} < 0$ are generally larger than for $H_{in} > 0$ is consistent with the effect of dipolar coupling between the fixed Ni layer and the free NiFe layer in each junction.

Figure 8.3 shows more detailed data of $I_{c+}$ and $I_{c-}$ versus $I_\phi$ for four selected values of $H_{in}$ taken just after each phase jump. Several features are immediately apparent in the data. First, $I_{c+}$ and $I_{c-}$ never approach zero, but rather oscillate with an amplitude of approximately 85 $\mu$A in all four magnetic states. Second, the oscillations of $I_{c+}$ and $I_{c-}$ are not sinusoidal, but rather have an asymmetric saw tooth or ratchet shape. Third, the maxima in the $I_{c+}$ and $I_{c-}$ data do not line up with each other, so in general $I_{c-}(\phi) \neq -I_{c+}(\phi)$. All three of these features are well understood [9, 18]; the first is due to the finite geometrical inductance of the SQUID loop, whereas the second and third are due to asymmetries in the inductances of the two arms of the loop and in the critical currents of the two junctions. The four magnetic states were fit independently, as described below. They properly take these asymmetries into account and show not only excellent agreement with the data but confirm $\pi$ phase shifts between successive magnetic states. These are most obviously observed in Figure 8.3 part b) which shows the average critical current, $I_c^{ave} = (I_{c+} - I_{c-})/2$, vs $I_\phi$. Though the offsets in $I_{c+}$ and $I_{c-}$ cause these curves to have an atypical shape, the black dashed line guides the eye to see the $\pi$ phase shifts between each state. The NiFe switching fields are also labeled for each state.

The results represented in Figure 8.3 were reproducible upon repeating the whole major loop several times. In addition, we obtained 'minor loop' data after initialization by keeping $H_{in}$ between +30 Oe and -35 Oe, so that only the free layer of JJ-1 switches its state back and forth. We have obtained similar minor loop data from several different nominally identical devices; the best major loop data were obtained in the device shown here.

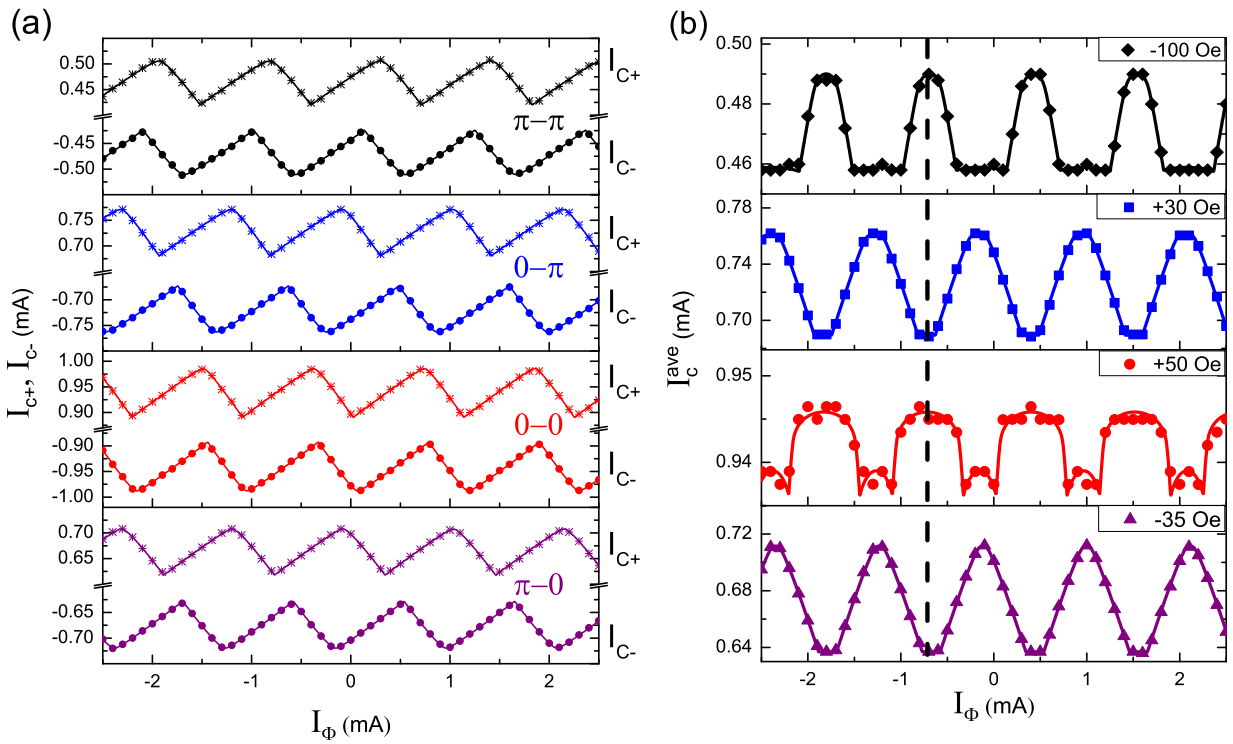


Figure 8.3 **$I_{c+}$, $I_{c-}$, and $I_c^{ave}$ Data with Fits for All Four Magnetic States for a SQUID containing NiFe(1.5)/Ni(1.2) Free and Fixed Layers** a) Positive and negative critical current values vs flux-line current, $I_\phi$ for the four magnetic states of the major loop. The state labels of '$\pi - \pi$,' '0 - $\pi$,' etc, refer to the phase states of JJ-1 and JJ-2, respectively. The ratchet shapes of the curves are due to asymmetries in the critical currents of the two junctions and the path inductance of the two arms of the loop. For each magnetic state, the $I_{c+}$ and $I_{c-}$ curves are shifted with respect to each other in opposite directions and by amounts that depend on the individual critical currents, $I_{c1}$ and $I_{c2}$, of the two Josephson junctions. The solid lines are the result of least-squares fits to the data using the asymmetric SQUID model described in Chapter 2. b) Plot of average critical current, $I_c^{ave} = (I_{c+} - I_{c-})/2$ versus $I_\phi$, for the same four magnetic states represented in a) including the switching field for each state. The colored solid lines are derived from the fits in a). Whereas the shapes of the $I_c^{ave}$ curves depend on the alignment between the $I_{c+}$ and $I_{c-}$ curves, the positions of the maximum and minima in $I_c^{ave}$ are immune to the shifts in $I_{c+}$ and $I_{c-}$. This figure shows schematically the $\pi$ phase shifts in the (0 - $\pi$) and ($\pi$ – 0) states relative to the ($\pi - \pi$) and (0 – 0) states, though the full fit analysis is required to verify the 0 - $\pi$ switching of the junctions.

### 8.1.1 SQUID Data Analysis

Several complementary methods were used to fit this asymmetric SQUID data to confirm a $\pi$ phase shift between successive magnetic states. The theory of an asymmetric SQUID was discussed in Chapter 2. The SQUID is characterized by the four parameters $L_1$, $L_2$, $I_{c1}$ and $I_{c2}$, which are the effective inductances of the two arms and the critical currents of the two Josephson junctions. $L_1$ and $L_2$ are simply related to the geometric inductances of the two arms if the mutual inductance between them is properly taken into account [77]. On the basis of the geometry shown in Figure 8.1, we expect that $L_2 > L_1$. In our samples $L_1$ and $L_2$ are fixed to the same value in all four magnetic states, whereas $I_{c1}$ and $I_{c2}$ change depending on whether the corresponding junction is in the 0 or $\pi$ state. The phase shifts seen in part b) of Figure 8.3 are not sufficient to verify real phase changes within the junctions because apparent $\pi$ shifts in the $I_c^{ave}(I_\phi)$ curves can arise purely from changes in $I_{c1}$ or $I_{c2}$. One can detect the presence of $\pi$ phase shifts by analyzing the shifts in the peak positions of the $I_{c+}$ and $I_{c-}$ curves when the SQUID transitions from state to state, as shown by the following argument.

The current reaches its maximum value, $I_c = I_{c1} + I_{c2}$, when the phase drop across each junction is $\pi/2$, so that the currents $I_1$ and $I_2$ through the two arms of the SQUID equal $I_{c1}$ and $I_{c2}$, respectively. Those currents induce a flux through the SQUID loop, $\Phi_{int} = L_1 I_{c1} - L_2 I_{c2}$. That must be balanced by the externally applied flux, so the peak in $I_{c+}$ occurs at a flux of $\Phi_{peak+} = -\Phi_{int+} = L_2 I_{c2} - L_1 I_{c1}$. The maximum negative critical current occurs at flux $\Phi_{peak-} = -\Phi_{peak+}$, hence the peaks in $I_{c+}(\phi)$ and $I_{c-}(\phi)$ are shifted with respect to each other by $\Delta\Phi_{peak} \equiv \Phi_{peak+} - \Phi_{peak-} = 2(L_2 I_{c2} - L_1 I_{c1})$. Because the $I_c(\phi)$ curves are periodic, $\Delta\Phi_{peak}$ can be determined only modulo $\Phi_0$. That means that the center of the pattern, that is the point half-way between an $I_{c+}$ peak and its corresponding $I_{c-}$ peak, can be determined only modulo $\Phi_0/2$. Fortunately, you can determine which of the possible values for $\Delta\Phi_{peak}$ is the physical value by analyzing the changes in $\Delta\Phi_{peak}$ when the critical current of only one of the junctions changes. If JJ-1 changes its critical current by an amount $\Delta\ I_{c1}$ whereas $I_{c2}$ remains unchanged, then the peak separation will

change by $\delta(\Delta\Phi_{peak}) = -2L_1\delta I_{c1}$. Turning the argument around, one can extract the inductance $L_1$ from the transition using $L_1 = -\delta(\Delta\Phi_{peak})/2\delta I_{c1}$. Similarly, if JJ-2 changes its critical current by an amount $\delta I_{c2}$ whereas $I_{c1}$ remains unchanged, then the peak separation will change by $\delta(\Delta\Phi_{peak}) = +2L_2\delta I_{c2}$. What one finds is that, if one takes the wrong value of $\delta(\Delta\Phi_{peak})$ for a transition, then the value of $L_1$ or $L_2$ extracted from the transition is unphysical. Our data set provides four transitions; the transitions from the ($\pi - \pi$) state to the (0-$\pi$) state and from the (0-0) state to the ($\pi$-0) state allow us to extract $L_1$, because only $I_{c1}$ changes, whereas the transitions from the (0-$\pi$) state to the (0-0) state and from the ($\pi$-0) state to the ($\pi - \pi$) state allow us to extract $L_2$, because only $I_{c2}$ changes. Only when $\pi$ phase shifts are included between successive staes can a consistent set of inductance values be obtained with $L_1$ = 6.0 $\pm$ 0.5 pH and $L_2$ = 11.7 $\pm$ 0.1 pH. These values are in agreement with the results of simulations of our SQUID geometry using the FastHenry software, which produced values in the range of 6–7 pH for $L_1$ and 13 pH for $L_2$, with variations of about 1 pH for each depending on the type of mesh used in the simulation. The inductance and junction critical current values obtained from this method are summarized in the first data row of Table 8.1. Different choices of $\delta(\Delta\Phi_{peak})$ that do not include the $\pi$ shifts yield values of $L_1$ and $L_2$ that differ in either direction by about 5 pH; those values are not only inconsistent with simulations of our geometry, but more importantly they are inconsistent with the observed depth of the $I_c(\phi)$ oscillations, which must be approximately equal to $\Phi_0$/L [18]. The phase shifts deduced from this analysis confirm that the SQUID does indeed acquire a phase shift of $\pi$ each time the system transitions between successive states in the sequence. Analyzing the four SQUID transitions in this manner also provides us with values for $\delta I_{c1}$ and $\delta I_{c2}$, but not values of the individual critical currents for each junction in each magnetic state. To estimate the latter, one can assume that the ratios of critical current densities between the 0 and $\pi$ states in both junctions are equal. That assumption implies that $I_{c10}/I_{c1\pi} = I_{c20}/I_{c2\pi}$, but allows the areas of the two junctions to differ. That analysis leads to the approximate critical current values listed in the top data row of Table 8.1.

To obtain more accurate values of the SQUID parameters, we performed a nonlinear least-

| | $L_1$ (pH) | $L_2$ (pH) | $I_{c1}^0$ ($\mu$A) | $I_{c1}^\pi$ ($\mu$A) | $I_{c2}^0$ ($\mu$A) | $I_{c2}^\pi$ ($\mu$A) |
|---|---|---|---|---|---|---|
| Preliminary Analysis | $6.0 \pm 0.5$ | $11.7 \pm 0.1$ | $560 \pm 10$ | $290 \pm 10$ | $420 \pm 10$ | $220 \pm 10$ |
| Least-squares fits | $5.68 \pm 0.1$ | $11.46 \pm 0.12$ | $565.9 \pm 1.4$ | $292.8 \pm 1.2$ | $419.5 \pm 0.2$ | $210 \pm 7$ |

Table 8.1 **NiFe(1.5)/Ni(1.2) SQUID and Junction Parameters** The inductances of the two arms of the SQUID and the critical currents of each junction in each of its two possible magnetic states are estimated from a simple analysis described in the text (top data row), or by least-squares fitting of the data shown in Figure 8.3 by numerical analysis.

| State | $L_1$ (pH) | $L_2$ (pH) | $I_{c1}$ ($\mu$A) | $I_{c2}$ ($\mu$A) | $\phi_{shift}$ | $\phi_{shift}$- $\phi_{global}$ |
|---|---|---|---|---|---|---|
| ($\pi$-$\pi$) | 5.73±0.05 | 11.38±0.08 | 291.6±1.5 | 216.8±1.5 | -0.1195±7E-4 | 0.0076 |
| (0-$\pi$) | 5.64±0.04 | 11.33±0.07 | 564.5±1.8 | 202.5±1.8 | +0.3517±6E-4 | 0.4788 |
| (0-0) | 5.63±0.03 | 11.56±0.06 | 567.3±2.0 | 419.3±2.0 | -0.1360±5E-4 | -0.0089 |
| ($\pi$-0) | 5.71±0.03 | 11.56±0.05 | 294.0±1.3 | 419.7±1.3 | +0.3955±4E-4 | 0.5226 |

Table 8.2 **Inductances of the Two SQUID Arms and Junction Critical Currents from Fit Parameters** These inductance values were obtained from the fits to the data for the four SQUID states listed in column 1. The uncertainties are given by the Nonlinear Least Squares fitting routine in Mathematica, and do not account for correlations between the fitting parameters [61]. $\phi_{global}$ = -0.1271 and is the average of the $\phi_{shift}$ values after subtracting 0.5 from the values of the (0-$\pi$) and ($\pi$-0) states.

squares fit to the data of a numerical analysis of the asymmetric SQUID using the Mathematica software. This fitting software was almost exclusively coded and executed by my coworker Joseph Glick. The asymmetric SQUID model used for this analysis was fully described in Chapter 2. To reduce the number of free parameters in the fits, we first determined the conversion from $I_\phi$ to $\phi$ by fitting the $I_c^{ave}(\phi)$ curves shown in Figure 8.3 part b) with a simple Fourier series. For the (0-$\pi$) and ($\pi$–0) states, a single cosine wave fits the data well, whereas for the (0–0) and ($\pi$–$\pi$) states we used a cosine wave plus its second harmonic. From the Fourier series fits to the four data sets, we determined that $I_\phi = (1.115 \pm 2)\mu A * \phi/\Phi_0$. That conversion factor was then kept fixed in all the ensuing fits. The fitting procedure was as follows. For each magnetic state, the data for $I_{c+}(I_\phi)$ and $I_{c-}(I_\phi)$ were fitted simultaneously. The free parameters in each fit were $I_{c+}$, $|I_{c-}|$, $\beta_L$, $\alpha_L$, $\alpha_I$ and $\phi_{shift}$. The dimensionless parameters $\beta_L$, $\alpha_L$, and $\alpha_I$ were discussed in Chapter 2 and

can be easily manipulated to determine the physical parameters $L_1$, $L_2$, $I_{c1}$, and $I_{c2}$. Although we expected $I_{c+}$ and $|I_{c-}|$ to be equal to each other, the data exhibited small differences between $I_{c+}$ and $|I_{c-}|$, of order a few $\mu$A. The last parameter, $\phi_{shift}$, is the dimensionless shift of the center of the pattern relative to zero flux. The values of the physical SQUID parameters extracted from the fits to all four magnetic states are shown in Table 8.2 with the average values of $L_1$, $L_2$, $I_{c1}^0$, $I_{c1}^\pi$, $I_{c2}^0$, and $I_{c2}^\pi$ listed in the bottom row of Table 8.1 for comparison with the phase-shift method values. The independent fits to the four magnetic states produce remarkably consistent results for the values of the two SQUID inductances and the critical currents of the two junctions, each in two magnetic states. Those values are very close to the preliminary values extracted from the analysis of the peak positions described above. The junction critical current values in each state confirm that between each successive magnetic state, primarily, one junction was switching. There is about an 8% change in the critical current of JJ-2 when JJ-1 was primarily switching from the $(\pi - \pi)$ state to the (0-$\pi$) state, but this change is required to obtain consistent inductance values so we believe this is a real effect caused by a slight magnetic change to JJ-2 during this switching process. Also, all these critical current values are large enough for JMRAM applications. Most importantly, the values of $\phi_{shift}$ confirm the additional phase shifts of $\pi$ that occur at each magnetic transition which is most obvious from the last column of Table 8.2 where $\phi_{shift}$ values of 0 and 0.5 correspond to phase shifts of 0 and $\pi$, respectively.

The data did include a global phase shift, $\phi_{global}$ = 0.1271 that is the average of the $\phi_{shift}$ values after subtracting 0.5 from the values of the (0-$\pi$) and ($\pi$-0) states. Despite our best efforts, we were not able to pin down the origin of this global shift. The data in the last column of Table 8.2 also show that, after subtracting $\phi_{global}$ from $\phi_{shift}$, the values of $\phi_{shift}$ are not exactly equal to 0 or 0.5 but include extra small shifts of about 0.022 in the (0-$\pi$) and ($\pi$-0) states and less than 0.01 in the (0-0) and ($\pi$-$\pi$) states. These small changes in $\phi_{shift}$ are consistent in relative magnitude and sign with what one would expect from the flux coupled into the SQUID by the NiFe layer magnetizations as they change direction. For example, the (0-$\pi$) state has both NiFe magnetizations pointing inward so they induce positive flux into the SQUID loop, thereby causing

the peaks in $I_{c+}$ and $I_{c-}$ to shift toward smaller flux. We have calculated the magnitude of these flux changes and find values several times larger than what is observed in the experiment; we believe that most of the flux is shielded by the wide superconducting electrodes placed directly above and below the junctions, which were not taken into account in the calculations. The major change in $\phi_{shift}$ is the addition of 0.5 in the (0-$\pi$) and ($\pi$-0) states relative to the (0,0) and ($\pi$-$\pi$) states, which is the major result of this work. This is clear from the last column of Table 8.2. This experiment and these results are similarly explained in reference [28].

## 8.2 NiFe(1.0)/NiFeCo(1.1) SQUIDs

After successfully demonstrating 0-$\pi$ phase switching in the NiFe(1.5)/Ni(1.2) system, we turned our attention to working towards optimizing these devices. Now that the proof of concept for JMRAM was complete, we needed to work towards creating many such phase controllable junctions with similar properties for use in a memory array and unit cell demonstration. We believed that the Ni fixed layer had poor magnetic properties and wanted to replace it with a better behaved magnetic material. Preliminary work measuring the 0-$\pi$ transition thickness for NiFeCo led us to believe that it would make a better choice. NiFeCo requires a lower initialization field of only several hundred Oersted, it was found to have single domain properties at the 0.5 $\mu m^2$ size, its switching field was sufficiently larger than that of the free layer, NiFe, and its magnetic switching showed more ideal behavior both directly from magnetometry measurements and indirectly from Fraunhofer pattern measurements.

The fixed layer NiFeCo was chosen to be a thickness of 1.1 nm to be close to its 0-$\pi$ transition thickness and the free layer NiFe was chosen to be a thickness of 1.0 nm to be below its 0-$\pi$ transition thickness. Additional improvements of the smoother base Nb electrode $[Nb(25)/Al(2.4)]_3$/(Nb(20) and a switch to a symmetric SQUID design, as shown in Figure 8.4, were implemented. The smoother electrode should improve the surface morphology and hence the magnetic properties of the two F layers. The symmetric design will reduce the inductance asymmetry since now $L_1$

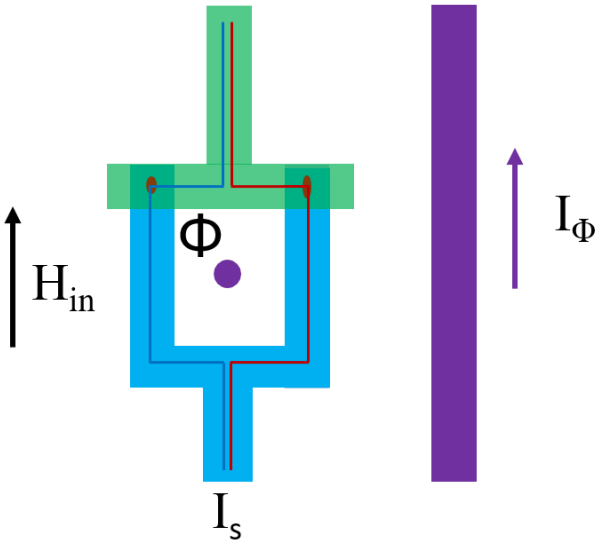


Figure 8.4 **Cartoon of Symmetric SQUID Layout** The SQUID device is made up of the blue pitchfork bottom lead which has a 3 $\mu$m width and the green T-shaped top lead with a 4 $\mu$m width. The inner dimensions of the loop are 6 $\mu$m by 6 $\mu$m. Sample current, $I_s$, travels up through the pitchfork and recombines in the green top lead. The nearby 3 $\mu$m wide purple flux line is driven with a current, $I_\phi$, to inject magnetic flux into the loop. An external in-plane field, $H_{in}$, is used to manipulate the magnetic layers in the junctions. The red and blue solid lines show the equal sample current paths through this symmetric SQUID design.

= $L_2$ which will reduce the shift in the $I_{c+}$ and $I_{c-}$ curves. This design also features smaller line widths. The blue bottom lead and purple flux line are 3 $\mu$m wide, the green top lead is 4 $\mu$m wide, and the inner dimension of the SQUID loop is 6 $\mu$m by 6 $\mu$m. The device functions in the same way as the asymmetric design described in Figure 2.15, but now the red and blue lines depicting the sample current path should have the same length. This new layout required slightly more flux-line current to complete one SQUID oscillation, with Fourier fits giving 1.382 mA of current for each flux quantum induced in the loop.

Since the NiFeCo has a lower saturation field, initializations were performed at -600 Oe before removing trapped flux from the device. In the same way as with the NiFe(1.5)/Ni(1.2) SQUID, oscillations of the critical current with applied flux were measured (at zero field) after an in-plane 'set' field was slowly stepped from 0 to +100 Oe and 0 to -100 Oe. The results from one such measurement are shown in the 3D plot of Figure 8.5. Here, the average critical current, $I_c^{ave}$, was

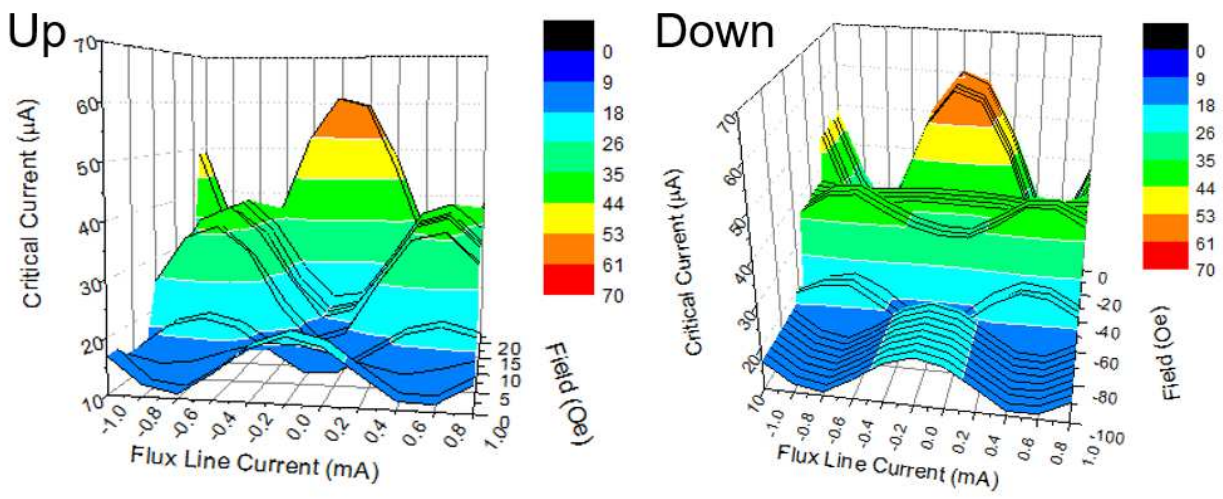


Figure 8.5 **Three-Dimensional Plots of Average SQUID Critical Current vs Flux-Line Current and In-Plane Set Field, $H_{in}$ for NiFe(1.0)/NiFeCo(1.1) SQUID** The $I_c^{ave}$ vs $I_\phi$ oscillations have much more sinusoidal shape due to the reduced asymmetry of these junctions and the low critical current values. These plots show evidence of 0-$\pi$ switching between successive states, but also several intermediate states. The 'up' sweep shows data for $H_{in} > 0$ and the 'down' sweep show data for $H_{in} < 0$.

plotted against the flux-line current and the 'set' field. While 0-$\pi$ switching is visually observed between several states, with a total of two phase switches in each field sweep direction, as expected, now we see the presence of intermediate switching states as well. The first oscillation at zero field, colored in light and dark blue, shows a maximum at zero flux-line current and is characterized as the ($\pi$-$\pi$) state. At around 5 Oe, the device exhibits a shift in phase with little change in the critical current total height before increasing drastically in critical current while maintaining the same phase shift by around 14 Oe. This lower critical current state at 5 Oe was characterized as an intermediate state with the full (0-$\pi$) state occurring at 14 Oe. This state is maintained until the 'set' field reaches 28 Oe when the device cleanly switches into the (0-0) state. Continuing with the 'set' field in the negative direction, the device transitions into a second intermediate state before switching to the ($\pi$-0) state at -44 Oe, and a third intermediate state before returning to the ($\pi$-$\pi$) initialization state at -70 Oe. These three intermediate states and the features of the 3D plot in general were reproducible over several major loop iterations and cooling cycles. Robust minor loops

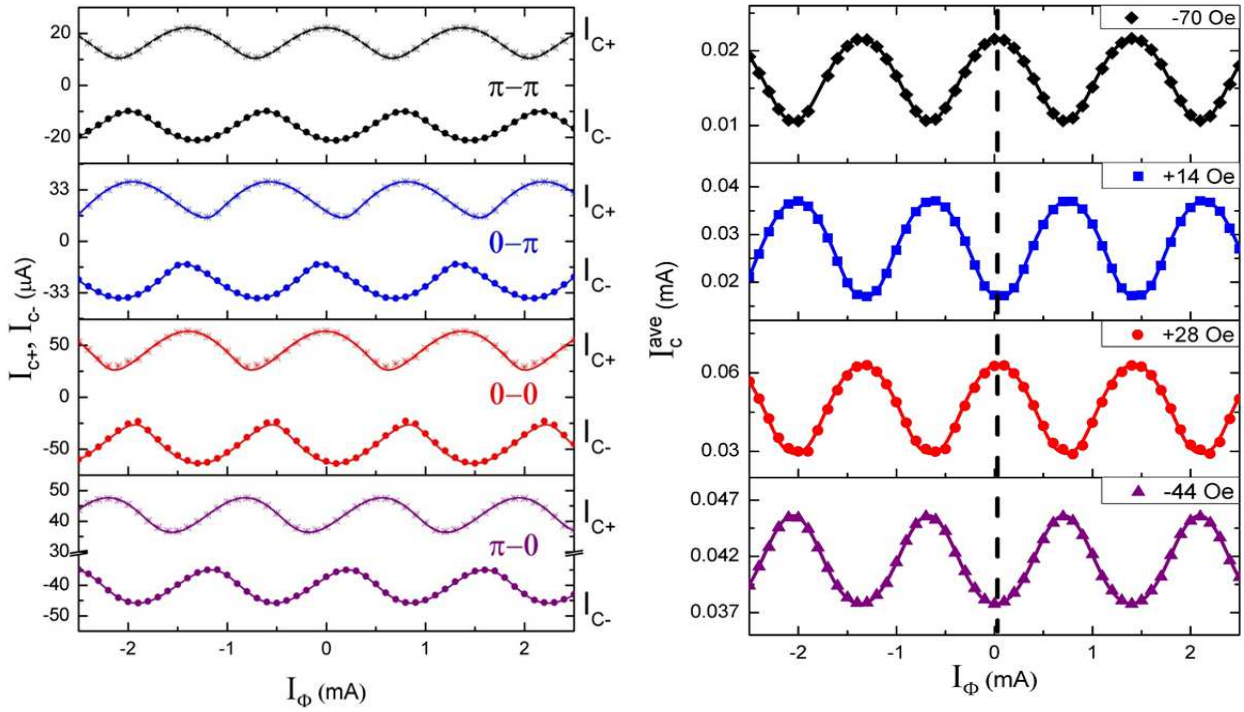


Figure 8.6 **$I_{c+}$, $I_{c-}$, and $I_c^{ave}$ Data with Fits for All Four Magnetic States for a NiFe(1.0)/NiFeCo(1.1) SQUID** The left-hand plot shows positive and negative critical current values vs flux-line current, $I_\phi$ for the four magnetic states of the major loop. These oscillations show a much more sinusoidal shape due to the reduced asymmetry and lower critical current values compared to the data in Figure 8.3. The solid lines are the result of least-squares fits to the data using the asymmetric SQUID model described in Chapter 2. The right-hand plot shows the average critical current, $I_c^{ave}$ versus $I_\phi$, for the same four magnetic states represented in a) including the switching field for each state. The colored solid lines are derived from the fits in a). This figure shows the $\pi$ phase shifts in the (0 - $\pi$) and ($\pi$ – 0) states relative to the ($\pi - \pi$) and (0 – 0) states, though the full fit analysis is required to verify the 0 - $\pi$ switching of the junctions.

with only the NiFe layer of one junction switching back and forth were also reproducibly collected. The intermediate switching states are not ideal, as they indicate some kind of magnetic change to the junctions before the full switch is realized. This could indicate a magnetic layer breaking into magnetic domains, remaining a single domain but with a a non-uniform magnetization direction, or another magnetic change that is stable over a small field range. However, intermediate states of this type do not pose a problem for JMRAM elements as long as a consistent field value can be used to change the junction phase by $\pi$.

Figure 8.6 shows these four magnetic states in terms of the $I_{c+}$, $I_{c-}$, and $I_c^{ave}$ oscillations with

| State | $L_1$ and $L_2$ (pH) | $I_{c1}(\mu A)$ | $I_{c2}(\mu A)$ | $\phi_{shift}$ |
|---|---|---|---|---|
| ($\pi - \pi$) | 5.9 | 16 | 7 | 0.024 |
| (0-$\pi$) | 12.1 | 15 | 23 | 0.541 |
| (0-0) | 7.9 | 37 | 27 | 0.035 |
| ($\pi$-0) | 6.1 | 42 | 6 | 0.513 |
| Average | 8.0 | | | |
| Standard Deviation | 2.9 | | | |

Table 8.3 **Fit Results for NiFe(1.0)/NiFeCo(1.1) SQUID 2328 4A-4** Since the symmetric design was used, the fits assumed that $L_1 = L_2$. There is a larger spread in the fitted inductance values compared to the NiFe(1.5)/Ni(1.2) SQUID and that is not well understood. The $\phi_{shift}$ values changing between around 0 and 0.5 represent the successive $\pi$ phase changes to the junctions between magnetic states.

flux-line current, $I_\phi$. It is immediately obvious that all of these oscillations are considerably more sinusoidal in shape than those from the NiFe(1.5)/Ni(1.2) SQUID since here the inductances are symmetric and the critical current is much lower. The solid lines represent least-squared fits to the data described in the analysis section above. Again, the theory is aptly able to match the data in all four states. The right-hand plot of $I_c^{ave}$ vs $I_\phi$ shows the 0-$\pi$ phase shifts between each state with the black dashed line guiding the eye. The switching fields obtained for this sample are somewhat lower than those from the NiFe(1.5)/Ni(1.2) SQUID, possibly due to the thinner NiFe or smoother base electrode used in this case. We also see that the switching fields are asymmetric, with larger values in the negative direction. This is again consistent with the effect of dipolar coupling which will favor a junction switching into the AP state.

The numerical results of the fits were used to calculate the physical parameters of the device, $L_1$, $L_2$, $I_{c1}$, $I_{c2}$, and $\phi_{shift}$. These values are summarized in Table 8.3. Since the symmetric SQUID design was used, $L_1$ and $L_2$ were constrained to have the same value. There is more variability in the value state to state, but the average of 8.0 pH is consistent with the expected value of 8.5 pH from our device geometry. The junction critical currents show that while primarily only one junction critical current changes between phase states, JJ-2 actually switches first instead of JJ-1 as expected from the junction shapes. Luckily, there was still a switching field difference between the

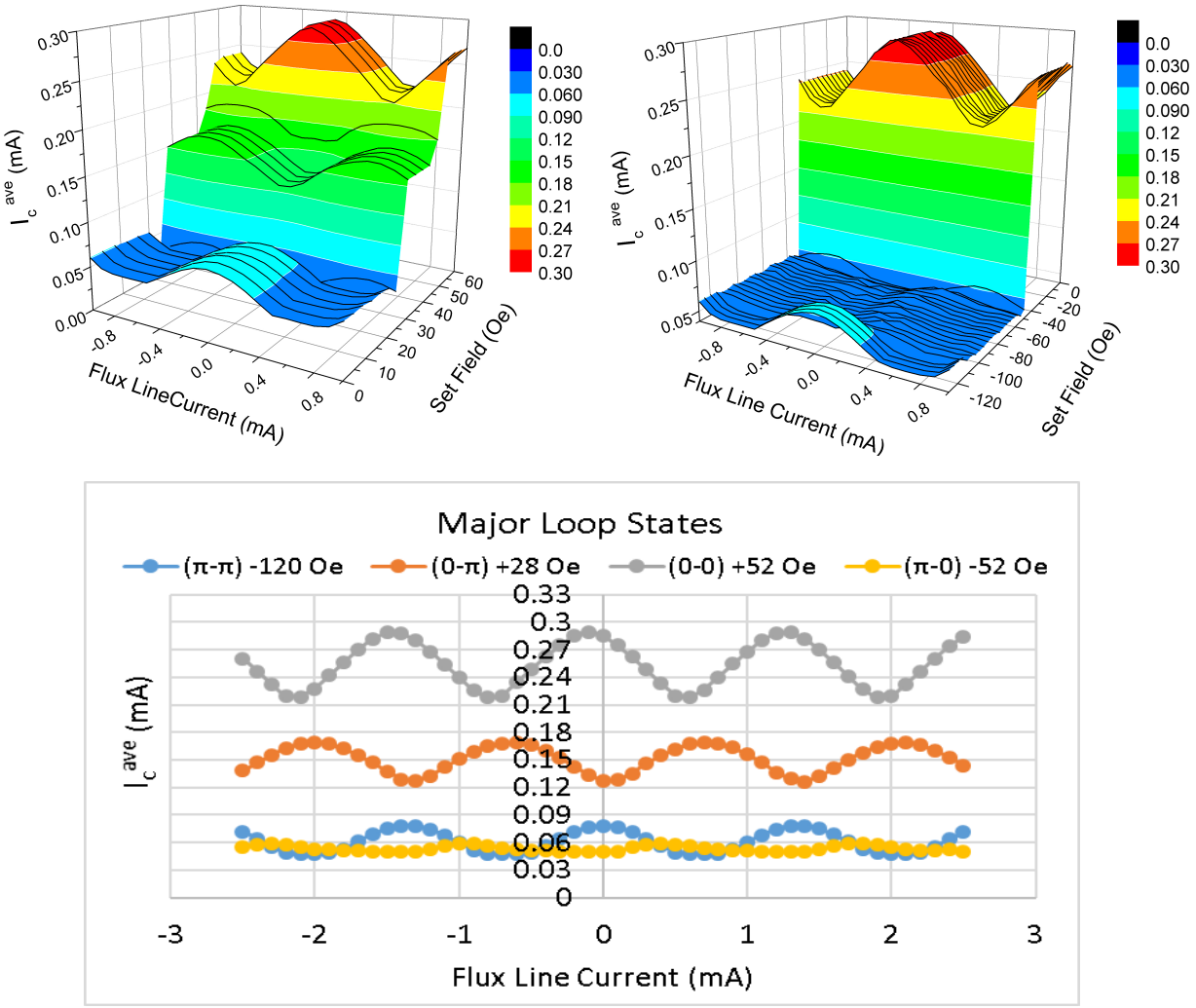


Figure 8.7 **3D Plots of the average critical current, $I_c^{ave}$, vs the flux-line current, $I_\phi$, and the 'set' field, $H_{in}$ for a NiFe(1.0)/NiFeCo(1.1) SQUID** These curves are also primarily sinusoidal in shape but the critical currents are significantly higher than those seen in the previous nominally identical SQUID. There are still some intermediate states but they persist over a much narrower field range. Below the 3D plots, four slices at each magnetic state are plotted together and labeled with their switching field values.

two junctions, but clearly the aspect ratio is not sufficient to control which junction will switch at a lower field value. There are some small critical current changes in the presumed non-switching junction which are not ideal and the magnitude of all these critical currents are too low for JRMAM applications. The $\phi_{shift}$ values, though, convincingly display 0-$\pi$ switching between the magnetic states making this system the second to demonstrate the effect.

The point of this second 0-$\pi$ demonstration was to show the $\pi$ phase switching in a more reproducible system, so another batch of nominally identical SQUIDs were fabricated in an attempt to observe the same effect in several additional samples. Unfortunately, that desire was not realized. Several samples showed reproducible minor loops, but the one sample which appeared to have 0-$\pi$ switching in a reproducible major loop showed its true behavior through the fit parameters and peak-shift analysis. Figure 8.7 shows the 3D plot for this second NiFe(1.0)/NiFeCo(1.1) SQUID. There are two apparent $\pi$ phase changes in each direction with less glaring intermediate states. The presumed '($\pi$-0)' state, colored dark blue, has a very small oscillation amplitude, but does also show an apparent $\pi$ phase shift. This is a little easier to see in the lower plot showing the four magnetic states of the major loop where the '($\pi$-0)' state is colored yellow. Some key differences between this sample measurement and the previous NiFe(1.0)/NiFeCo(1.1) SQUID are apparent. First, the maximum total critical current here is about four times larger. Second, the switching fields for the NiFe in this sample are also significantly larger. Third, the intermediate states are still occasionally present, but they persist for a much shorter field range. Lastly, even looking at the $I_c^{ave}$ data, the successive states do not show perfect $\pi$ phase shifts between all four states. This is most obviously seen in the lower plot.

Fits were only obtained for the first three magnetic states, with the '($\pi$-0)' state showing too small of an oscillation amplitude for a reliable fit to be found. A summary of the fit result parameters are shown in Table 8.3 where the fit starting values were chosen to encourage a $\pi$ phase shift in the '(0-$\pi$)' state. You can see that the first fit to this state has highly irregular $L_1$ and $L_2$ values. Additionally, the critical current values show that both junctions change their critical currents between successive states. Also, when the peak shift analysis is considered between the '($\pi$-$\pi$)' and '(0-$\pi$)' state and between the '(0-$\pi$)' and '(0-0)' state a value for $L_1$ and $L_2$ can be obtained. Using this process gives $L_1$ = 0.45 pH and $L_2$ = 3.25 pH. These values are clearly too small for the physical device layout.

When the $\pi$ phase shift is not encouraged in the starting fit values, a different local minima is chosen by the fit which gives more reasonable $L_1$ and $L_2$ values from the fits. This is shown

| State | $L_1$ (pH) | $L_2$ (pH) | $I_{c1}(\mu A)$ | $I_{c2}(\mu A)$ | $\phi_{shift}$ |
|---|---|---|---|---|---|
| ('$\pi-\pi$') | 8.24 | 7.63 | 27 | 51 | 0.00 |
| ('0-$\pi$' (1)) | 9.90 | 16.99 | 101 | 67 | 0.524 |
| ('0-$\pi$' (2)) | 10.13 | 12.81 | 133 | 35 | 0.024 |
| ('0-0') | 7.65 | 7.59 | 151 | 138 | -0.075 |
| Average (1) | 8.59 | 10.74 | | | |
| Standard Deviation (1) | 1.17 | 5.42 | | | |
| Average (2) | 8.67 | 9.35 | | | |
| Standard Deviation (2) | 1.30 | 3.01 | | | |

Table 8.4 **NiFe(1.0)/NifeCo(1.1) SQUID 2336 5B-4 Fit Parameters** Fit Parameters giving initial conditions to encourage the appearance of 0-$\pi$ switching in the $\phi_{shift}$ value for NiFe(1.0)/NiFeCo(1.1) SQUID 2336 5B-4. Only the first three magnetic states could be successfully fit. The forced state, '($\pi$-0)(1)', shows an unphysically large asymmetry in $L_1$ and $L_2$. State '($\pi$-0)(2),' which does not include the $\pi$ phase shift, still shows some inductance asymmetry but has much more reasonable values for $L_2$. This feature leads us to believe that the junction is not showing 0-$\pi$ phase changes. Both fits show some degree of critical current change in both junctions, though only one is presumed to switch between each magnetic state. Primarily, JJ-1 switches first and JJ-2 second, but the other junction is somewhat affected.

in Table 8.3 as state '(0-$\pi$) (2).' The peak-shift analysis inductances are also much closer to the expected values with $L_1$ = 10.08 pH and $L_2$ = 7.70 pH. However, even this fit with no 0-$\pi$ phase changes shows that both junctions change critical current in each state change. This analysis indicates that the second NiFe(1.0)/NiFeCo(1.1) SQUID did not show phase switching despite being nominally identical in material stack and fabrication to the first sample which did show phase switching. This unfortunate result led us to believe that even though these material thicknesses were chosen based on single layer S/F/S studies of the two individual materials, perhaps that is not sufficient to predict how the junction will behave in a spin-valve stack. Perhaps this set of thicknesses puts either the P or AP state very close to a phase transition so that small variations in material thickness from sputtering run to sputtering run could cause one sample to show 0-$\pi$ phase switching while another does not. This result led to the first of the single junction spin-valve series studies described in Chapter 7 used to pin down the range of thicknesses that would produce phase switching in several systems.

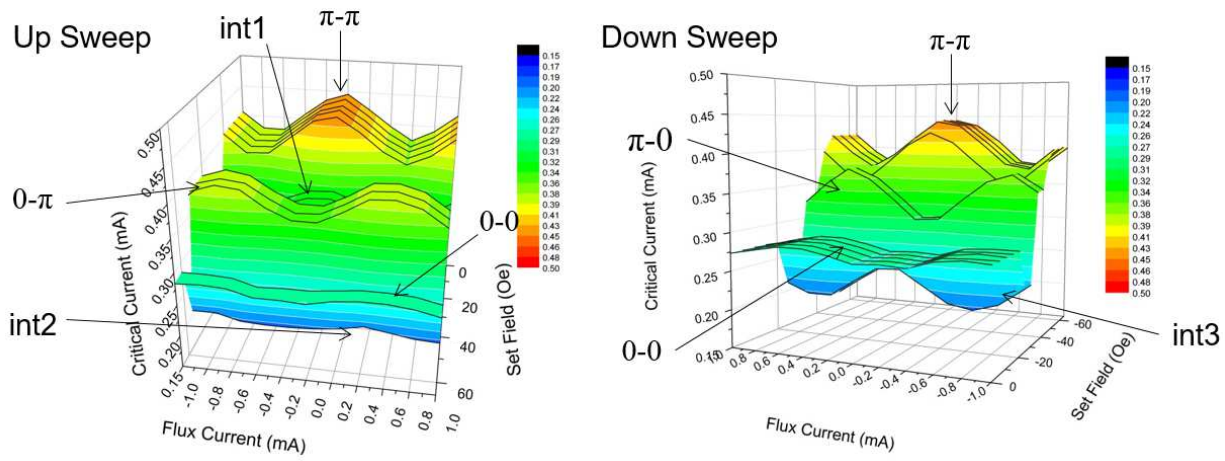


Figure 8.8 **3D plot of average critical current vs flux current and applied 'set' field for NiFe(1.25)/Ni(2) SQUID 1A-2** The 'up sweep' shows positive set field values and the 'down sweep' shows negative field values. The first measured oscillation at zero field had the largest critical current, so the 'up sweep' data is rotated with zero field in the back of the plot working forward to positive field values so the data can be better seen. The 'real' phase states and intermediate phase states are labeled in the plots with black arrows.

## 8.3 NiFe(1.25)/Ni(2.0) SQUIDs

Continuing the quest for reproducible phase switching samples, we returned to the NiFe/Ni system. A smoother base electrode and normal metal buffer and spacer layers were developed, as discussed in Chapter 4, which were expected to reduce sample roughness and improve magnetic behavior. Thicker Ni was investigated as a fixed layer in a single junction spin-valve study which showed acceptable magnetic results as well as determined the optimum NiFe thickness to use with Ni(2). This thickness was shown to be 1.25 nm based on where 0-$\pi$ switching was expected to occur and where the critical currents of the junction was most similar in the P and AP state at zero field. We believed that this would highly reduce the critical current asymmetry in the SQUID devices. Paired with the symmetric SQUID design which reduces the inductance asymmetry, we expected very little shift in the $I_{c+}$ and $I_{c-}$ curves for these samples.

The final structure of these samples was [Nb(25)/Al(2.4)]$_3$/Nb(20)/Cu(2)/NiFe(1.25)/Cu(4)/Ni(2.0)/Cu(2)/Nb(5)/Au(15)/Nb(150)/Au(10). A handful of SQUIDs were measured from this batch. Samples were initialized with a -1500 Oe field and trapped flux was removed. Many

samples showed minor loop behavior and apparent $\pi$ phase switching. The best major loop data is shown in Figure 8.8. This 3D plot shows the average critical current vs flux-line current and applied 'set' field for an 'up' and 'down' sweep of positive and negative field values, respectively. The 'real' and 'intermediate' states are labeled in the plot with black arrows. In addition to the four expected magnetic states, three intermediate states were observed for this sample. The intermediate states all show a dip in critical current reminiscent of the dips in critical current of the Fraunhofer patterns near zero field in the spin-valve series studies. Switches occurred at +25 Oe, +60 Oe, -25 Oe, and -45 Oe. For the first time, the asymmetry in these switching fields does not favor the AP magnetic state.

Both the presumed 'real' phase states and intermediate states were fit to determine the physical parameters of the SQUID and to see if 0-$\pi$ switching occurred in this sample. Figure 8.9 shows the results of these fits for the four main phase states. Each row represents one of the four magnetic states and each column represents a starting horizontal shift ($\phi_{shift}$) value for the fit of either 0 or 0.5. A shift of 0 indicates both junctions are in the 0 or $\pi$ phase states and a shift of 0.5 indicates that one junction is the the 0 state and the other is in the $\pi$ state. Both versions of the fit for each magnetic state not only have excellent agreement with the data, but the other fit parameters, shown in Figure 8.10, have physically reasonable values. For past samples, fit ambiguity was distinguished by unphysical inductance values obtained either directly from the fit parameters or from the peak-shift analysis. Figure 8.10 shows that the SQUID parameters obtained from the two fits for each of the expected and intermediate states have reasonable inductance values. Intermediate states 2 and 3 were only able to be fit with one set of parameters and the black arrows on the left-hand side of the table indicate where the intermediate states fall into the ordering of the major loop. The set of states colored either light or dark blue run through a full major loop of states and exhibit $\pi$ phase switching between successive state. The light blue data begin assuming the correct ($\pi$-$\pi$) state has $\phi_{shift} = 0$ while the dark blue data begin assuming the correct ($\pi$-$\pi$) state has $\phi_{shift} = 0.5$. Both states tell the same story with one junction switching between each magnetic state except for the ($\pi$-0) to ($\pi$-$\pi$) state change where both stories require that both junctions change

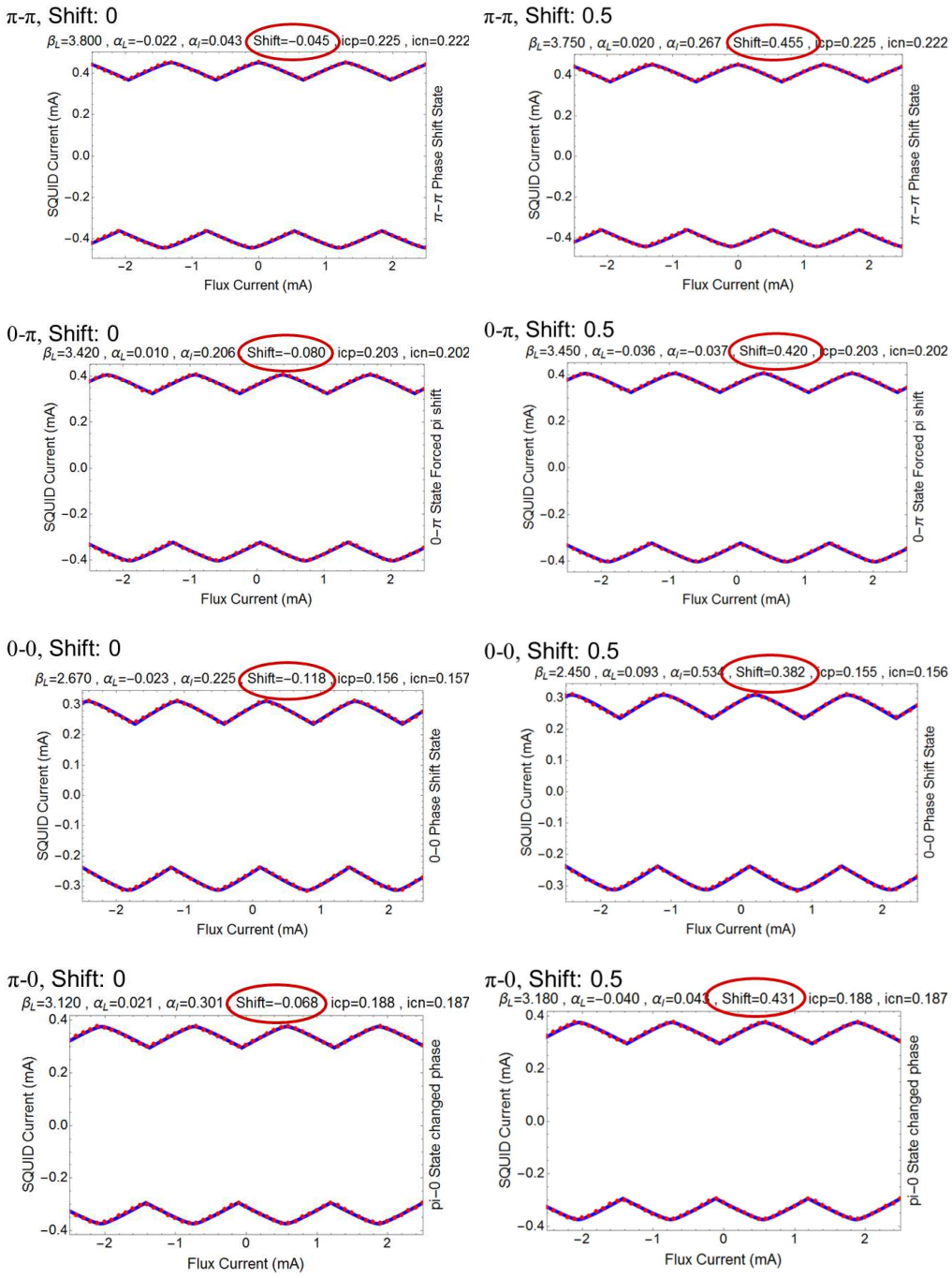


Figure 8.9 **Ambiguous Fits to NiFe(1.25)/Ni(2) SQUID Major Loop States** Each row represents one of the four magnetic states. Depending on the starting values given to the fitting software, fits with shift values of approximately 0 (both junctions are in the same phase state) or 0.5 (only one junction is in the $\pi$ phase state) could be obtained. In previous cases, the fit inductance values or peak-shift analysis inductance values could be used to distinguish the physically relevant state. Unfortunately, for this data, both fits for each state give nearly identical inductance values by both analysis methods, so the results are ambiguous.

| | State | $L_1$ (pH) | $L_2$ (pH) | $I_{c1}$ (mA) | $I_{c2}$ (mA) | $\phi_{shift}$ |
|---|---|---|---|---|---|---|
| | π-π | 8.97 | 8.59 | 213.7 | 233.1 | -0.045 |
| int1 → | π-π (2) | 8.49 | 8.83 | 163.5 | 283.1 | 0.455 |
| | 0-π | 8.64 | 8.81 | 160.9 | 244.5 | -0.080 |
| int2 → | 0-π (2) | 9.12 | 8.48 | 210.3 | 195.2 | 0.420 |
| | 0-0 | 9.05 | 8.65 | 120.9 | 191.2 | -0.118 |
| int3 → | 0-0 (2) | 7.37 | 8.89 | 72.5 | 238.8 | 0.382 |
| | π-0 | 9.12 | 8.42 | 179.2 | 195.2 | 0.431 |
| | π-0 (2) | 8.43 | 8.79 | 130.7 | 243.4 | -0.068 |
| | int1 | 8.71 | 9.18 | 161.4 | 188.1 | -0.054 |
| | (2) | 9.15 | 8.62 | 209.2 | 140.2 | 0.446 |
| | int2 | 22.78 | 15.06 | 75.1 | 138.6 | 0.357 |
| | (2) | | | | | |
| | int3 | 12.00 | 8.74 | 0.1009 | 0.1470 | 0.070 |
| | (2) | | | | | |

Figure 8.10 **SQUID Fit Data to All Major Loop States for a NiFe(1.25)/Ni(2) SQUID** Each of the four expected magnetic states and three intermediate states were fit with starting parameters to encourage either a $\phi_{shift}$ of 0 or 0.5. Intermediate states 2 and 3 only converged into one fit. State sets marked in either light or dark blue represent a complete set of major loop states that include $\pi$ phase shifts between successive states. The inductance values obtained from the fits can't be used to distinguish between physcial and unphysical fits since the values are very similar whether the phase shift is 0 or 0.5.

critical current.

The peak-shift analysis requires looking at the changes between two different magnetic states. This was used to investigate whether the light or dark blue data sets gave physically relevant inductance values. Unfortunately, both sets gave almost identical inductance values, so that method could not be used to eliminate one set of fits. Mixing states from the light and dark blue sets so that no phase switching is assumed sometimes gives identical inductance parameters and sometimes values that differ by 3-4 pH. So while it is likely that this sample and others in this set are showing 0-$\pi$ phase switching, we cannot reliably distinguish the physical SQUID parameters that describe the sample.

To overcome this issue, it would be helpful if it were only possible to fit each magnetic state with one set of parameters. This can be achieved with a low inductance SQUID design. Generally,

the peak position of one state is given by $\phi_{peak} = (L_2 I_{c2} - L_1 I_{c1})/\Phi_0 = \beta_L(\alpha_L + \alpha_I)/2$. (Reminder that $\alpha_L = (L_2 - L_1)/(L_1 + L_2)$, $\alpha_I = (I_{c2} - I_{c1})/(I_{c1} + I_{c2})$, and $\beta_L = I_c L/\Phi_0$). The peak shift when a magnetic state changes from one state to the next is given by $\Delta\phi_{peak} = \beta_L * \Delta\alpha_I/2$. Since $\alpha_I$ is constrained to have values between -1 and 1, we find the maximum peak shift $\Delta\phi_{peak}^{max} = \beta_L$. If $\Delta\phi_{peak} < 1/2$ then only one set of fit parameters will match the data, so if we design our SQUIDs so that $\beta_L < 0.5$ we will be able to avoid ambiguity regarding $\pi$ phase shifts in our fits. Assuming SQUID critical currents of 0.5 mA, total SQUID inductance of 2 pH or less will meet this criteria. This criteria is very strict since we use $\Delta\alpha_I = 2$ indicating that in one state all the critical current passes through JJ-1 with none passing through JJ-2 and in the next state all the critical current passes through JJ-2 with none passing through JJ-1. Since this is unlikely to happen in our samples, slightly larger L values would likely still produce unambiguous fits. The group is currently working towards fabricating SQUIDs with much lower inductances to continue the search for reproducible phase switching junctions.

# CHAPTER 9

# CONCLUSIONS

## 9.1 Summary of Results

Throughout this work, an extensive study of ferromagnetic Josephson junctions was performed with the hopes to experimentally realize the first phase-controllable junctions. Theories predicted that a phase-controllable junction could be realized if the junction contained two ferromagnetic layers (a spin valve) with properly chosen thicknesses. Then, when the magnetizations of these two layers are manipulated between the parallel and antiparallel configurations, the junctions would change its ground state phase between $\pi$ and 0. Such a phase-controllable junction has immediate applications as the switching element in a superconducting memory to serve ultra-low power computing efforts.

To experimentally verify phase switching, interference measurements were needed. This required complicated measurements with two spin-valve junctions together in a superconducting loop so that the relative phase between the two junctions could be probed. The results from such an experiment are difficult to interpret without adequate background information about the magnetic and superconducting properties of the ferromagnetic materials used as well as interface effects and roughness induced from the base superconducting electrode and normal metal spacer layers.

Preliminary work was completed to address these issues. Prior to my time in the group, samples were fabricated with one of two base superconducting layers. One was a slab of Nb and the other interleaved Al with that Nb for smoother surface morphology. My AFM study of seven additional base electrode candidates varying Nb thickness, interleave material, and number of base structure repeats was able to identify a base electrode with 35% lower RMS roughness than the previous best structure. Subsequently, the surface roughness of the normal metal layers used in the full spin-valve stack were also evaluated. Historically, Cu(5) was used as a magnetic seed layer and Cu(10) was used to magnetically decouple two ferromagnetic layers. TEM images revealed that

these layers were introducing roughness to the thin ferromagnetic layer, which can have adverse effects on their magnetic properties. Indirect roughness measurements were taken by sandwiching a NiFe layer between a spacer layer of interest and comparing the magnetic properties of that NiFe with magnetometry measurements. Many normal metal spacer layers were identified that produced better NiFe magnetic properties than Cu(5) and Cu(10). However, some of these layers, namely Ru(2)/Al(7)/Ru(2) and Cu(2)/Al(6)/Cu(2) produced excellent NiFe magnetic properties, but later were found to cripple the critical current through a Josephson junction. The struggle to obtain both adequate superconducting properties (sufficient critical current through the junction) and adequate magnetic properties (low switching field for free layer, single domain reproducible magnetic behavior) within a single Josephson junction was the main goal of these background studies. Cu(2) and Cu(4) spacers were decided to have the most advantages for both properties.

Magnetometry is a valuable tool to determine the magnetic properties of potential materials for spin-valve devices. Measurements of extended thin films gave information about the switching field range of the material, dead layer effects at interfaces, saturation magnetization, and the fields required to obtain this saturation. Data from studies of free layer candidate NiFe and fixed layer candidates Ni, NiFeCo, and NiFe/FeMn were showcased to support their inclusion in subsequent junction studies.

Next, ferromagnetic materials of interest for the spin-valve stack were first classified alone in S/F/S Josephson junctions while varying the F layer thickness. This crucial study informed the 0-$\pi$ transition thickness of the material, the switching field range to change the material magnetization direction by 180°, the magnitude of the critical current that can traverse the junction, and the decay in that critical current as the F layer thickness increases. After these studies, NiFeMo and NiFe/FeMn were found to have undesirable properties and were not further studied. Free layer material NiFe and fixed layer materials Ni and NiFeCo were the focus of spin valve and SQUID devices.

Independently studying materials in S/F/S junctions gave us much information about the superconducting and magnetic properties of our materials of interest. However, we learned that when

putting two such materials together in a spin valve, you don't have sufficient predictive power from only these single F layer studies. To bridge this gap, studies of several series of spin-valves varying the thickness of one F layer were performed. These valuable studies shed light on the proper thickness combinations for the F layers that produce phase switching, the total critical currents obtained when the junction is in the parallel and antiparallel configurations, switching field ranges for the two F layers, fields required to saturate the magnetization of the two F layers, and the stability of the magnetic state at and around zero external applied field. Series with NiFe/NiFeCo and NiFe/Ni were studied to inform SQUID device reproduciblity and F layer thickness choices.

The culmination of this work came from the successful demonstration of phase-controllable SQUID devices in both the NiFe/NiFeCo and NiFe/Ni magnetic systems. Major loop measurements where both junctions' free layers switched back and forth, and minor loop measurements where only one junction's free layer switched back and forth were shown in both cases. Independent fits to the four accessible magnetic configurations in the major loop were performed to verify the presence of successive $\pi$ phase shifts between states. This marked the first phase-sensitive demonstration of phase-controllable ferromagnetic Josephson junctions.

## 9.2 Future Work

Though great progress has been made in this work to demonstrate phase-controllable ferromagnetic Josephson junctions, for memory application, large numbers of junctions with the same properties are required for memory arrays. This will require much additional investigation. First, the magnetic materials used in the spin-valve junctions could be improved. A free layer with lower switching fields and a fixed layer with more reliable magnetic properties are desired. We are constrained, however, by the need to obtain at least 100 $\mu$A of critical current through the stack, limiting our options. Future free layer material studies will include PdFe alloys and fixed layer material studies will include attempting to pin Ni with IrMn. PdFe is a weak ferromagnet, so its 0-$\pi$ transition thickness can be many times larger than that of NiFe depending on the Fe concentration. This

gives larger margins on the layer thickness and could improve magnetic properties. We know from our studies of Ni that it shows non-reproducible magnetic behavior. Perhaps this could be controlled by pinning the Ni with IrMn. In contrast to the FeMn pinning used previously, IrMn could allow more critical current through the junction. Additionally, the Ni is known to have significantly higher critical current values than NiFe, so a spin-valve stack with this fixed layer could possibly meet the 100 $\mu$A desired value.

To address SQUID fitting ambiguity issues, low inductance SQUID layouts have already been designed by the group recently. If the inductance of the design is sufficiently low, such that only one set of fit parameters can describe the data, it will greatly simplify the SQUID analysis procedure. With this advantage, minor loops alone could be used to verify phase switching in the devices. This opens up new experimental designs where one bit is patterned into a specific shape to increase its switching fields, such as a high aspect ratio diamond or hexagon, while the other remains an easy to switch elliptical bit. Then measurements would only switch the elliptical bit back and forth while the higher switching field bit would remain always in the same initialized state. This would speed up the measurement and analysis process as well as restrict measurements to lower field ranges, decreasing the possibility of altering unstable magnetic states.

Lastly, our collaborators at Northrop Grumman have been developing read and write architecture to use our phase-controllable junction in a real memory scheme. They recently realized a functional unit cell demonstration using the magnetic stack developed by our group at Michigan State, but hopefully the future will hold larger array demonstrations and eventually a commercially available memory system. In time, this, or a similar memory system could be integrated into a fully superconducting supercomputer, able to solve interesting problems at a fraction of the energy cost needed for conventional technology.

# BIBLIOGRAPHY

## BIBLIOGRAPHY


[1] Makram Abd El Qader, R. K. Singh, Sarah N. Galvin, L. Yu, J. M. Rowell, and N. Newman. Switching at small magnetic fields in Josephson junctions fabricated with ferromagnetic barrier layers. *Appl. Phys. Lett.*, 104(2), 2014.

[2] P. W. Anderson and J. M. Rowell. Probable observation of the Josephson superconducting tunneling effect. *Phys. Rev. Lett.*, 10:230–232, Mar 1963.

[3] A. F. Andreev. The thermal conductivity of the intermediate state in superconductors. *J. Exptl. Theoret. Phys. (U.S.S.R.)*, 46(5):1823–1828, 1964.

[4] B. Baek, W. H. Rippard, S. P. Benz, S. E. Russek, and P. D. Dresselhaus. Hybrid superconducting-magnetic memory device using competing order parameters. *Nature Commun.*, 5:3888, 2014.

[5] S. V. Bakurskiy, N. V. Klenov, I. I. Soloviev, V. V. Bol'ginov, V. V. Ryazanov, I. V. Vernik, O. A. Mukhanov, M. Yu. Kupriyanov, and A. A. Golubov. Theoretical model of superconducting spintronic SIsFS devices. *App. Phys. Lett.*, 102(19), 2013.

[6] A. A. Bannykh, J. Pfeiffer, V. S. Stolyarov, I. E. Batov, V. V. Ryazanov, and M. Weides. Josephson tunnel junctions with a strong ferromagnetic interlayer. *Phys. Rev. B*, 79:054501, Feb 2009.

[7] J. Bardeen, L. N. Cooper, and J. R. Schrieffer. Microscopic theory of superconductivity. *Phys. Rev.*, 106:162–164, Apr 1957.

[8] J. Bardeen, L. N. Cooper, and J. R. Schrieffer. Theory of superconductivity. *Phys. Rev.*, 108:1175–1204, Dec 1957.

[9] A. Barone and G. Paternò. *Physics and applications of the Josephson effect*. Wiley, 1982.

[10] C. Bell, G. Burnell, C. W. Leung, E. J. Tarte, D.-J. Kang, and M. G. Blamire. Controllable Josephson current through a pseudospin-valve structure. *Appl. Phys. Lett.*, 84:1153–1155, 2004.

[11] Y. Blum, A. Tsukernik, M. Karpovski, and A. Palevski. Oscillations of the superconducting critical current in Nb-Cu-Ni-Cu-Nb junctions. *Phys. Rev. Lett.*, 89:187004, 2002.

[12] Kurt M. Boden, W. P. Pratt, and Norman O. Birge. Proximity-induced density-of-states oscillations in a superconductor/strong-ferromagnet system. *Phys. Rev. B*, 84:020510, Jul 2011.

[13] L. N. Bulaevskii, V. V. Kuzzii, and A. A. Sobyanin. Superconducting system with weak coupling to the current in the ground state. *JETP Lett.*, 25:290, 1977.

[14] A. I. Buzdin. Proximity effects in superconductor-ferromagnet heterostructures. *Rev. Mod. Phys.*, 77:935–976, Sep 2005.

[15] A. I. Buzdin, L. N. Bulaevski, and S. V. Panyukov. Critical-current oscillations as a function of the exchange field and thickness of the ferromagnetic metal (F) in an S-F-S Josephson junction. *JETP Lett.*, 35:179, 1982.

[16] A. I. Buzdin and M. Yu. Kupriyanov. Transition temperature of a superconductor-ferromagnet superlattice. *JETP Lett.*, 52:488, 1990.

[17] A. I. Buzdin and M. Yu. Kupriyanov. Josephson junction with a ferromagnetic layer. *JETP Lett.*, 53:321, 1991.

[18] Boris Chesca, Reinhold Kleiner, and Dieter Koelle. *The SQUID Handbook, Volume 1*. Wiley-VCH Verlag GmbH & Co. KGaA, 2005.

[19] T. W. Clinton and Mark Johnson. Nonvolatile switchable Josephson junctions. *Journal of Applied Physics*, 85(3):1637–1643, 1999.

[20] R. de Bruyn Ouboter and A. Th. A. M. de Waele. Superconducting point contacts weakly connecting two superconductors. *Rev. Phys. Appl. (Paris)*, 5:25, 1970.

[21] P. G. de Gennes. Boundary effects in superconductors. *Rev. Mod. Phys.*, 36:225–237, Jan 1964.

[22] E. A. Demler, G. B. Arnold, and M. R. Beasley. Superconducting proximity effects in magnetic metals. *Phys. Rev. B*, 55:15174–15182, Jun 1997.

[23] G. Deutscher and P. G. de Gennes. *Superconductivity, Vol. II*. edited by R. D. Parks, Marcel Dekker, New York, NY, USA, 1969.

[24] D. E. Eastman, F. J. Himpse, and J. A. Knapp. Experimental band structure and temperature-dependent magnetic exchange splitting of nickel using angle-resolved photoemission. *Phys. Rev. Lett.*, 40:1514–1517, Jun 1978.

[25] D. E. Eastman, F. J. Himpse, and J. A. Knapp. Experimental exchange-split energy-band dispersions for Fe, Co, and Ni. *Phys. Rev. Lett.*, 44:95–98, Jan 1980.

[26] R. P. Feynman, R. B. Leighton, and M. Sands. *The Feynman Lectures on Physics, Vol III.* Addison-Wesley Publishing Company, Massachusetts, 1965.

[27] T. A. Fulton, L. N. Dunkleberger, and R. C. Dynes. Quantum interference properties of double Josephson junctions. *Phys. Rev. B*, 6:855–875, Aug 1972.

[28] E. C. Gingrich, Bethany M. Niedzielski, Joseph A. Glick, Yixing Wang, D. L. Miller, Reza Loloee, W. P. Pratt Jr, and Norman O. Birge. Controllable 0-$\pi$ Josephson junctions containing a ferromagnetic spin valve. *Nat. Phys.*, 12(6):564–567, Jun 2016.

[29] J. A. Glick, M. A. Khasawneh, B. M. Niedzielski, E. C. Gingrich, P. G. Kotula, N. Missert, R. Loloee, W. P. Jr. Pratt, and N. O. Birge. Critical Current Oscillations of Elliptical Josephson Junctions with Single-Domain Ferromagnetic Layers. *arXiv:1608.08998*, August 2016.

[30] J. A. Glick, R. Loloee, W. P. Pratt, and N. O. Birge. Critical current oscillations of Josephson junctions containing PdFe nanomagnets. *IEEE Transactions on Applied Superconductivity*, 27(4):1–5, June 2017.

[31] E. Goldobin, H. Sickinger, M. Weides, N. Ruppelt, H. Kohlstedt, R. Kleiner, and D. Koelle. Memory cell based on a $\phi$ Josephson junction. *App. Phys. Lett.*, 102(24), 2013.

[32] R. Gross and A. Marx. *Applied Superconductivity: Josephson Effect and Superconducting Electronics*. Walther-Meissner-Institute, 2005.

[33] D. M. Heim, N. G. Pugach, M. Yu Kupriyanov, E. Goldobin, D. Koelle, R. Kleiner, N. Ruppelt, M. Weides, and H. Kohlstedt. The effect of normal and insulating layers on 0-$\pi$ transitions in Josephson junctions with a ferromagnetic barrier. *New J. Phys.*, 17(11):113022, 2015.

[34] R. Held, J. Xu, A. Schmehl, C. W. Schneider, J. Mannhart, and M. R. Beasley. Superconducting memory based on ferromagnetism. *Applied Physics Letters*, 89(16):163509, 2006.

[35] A. Y. Herr and Q. P. Herr. Josephson magnetic random access memory system and method,, September 18 2012. US Patent 8,270,209.

[36] A.Y. Herr, Q.P. Herr, and O. Naaman. Phase hysteretic magnetic Josephson junction memory cell,, March 8 2016. US Patent 9,281,057.

[37] Quentin P. Herr, Anna Y. Herr, Oliver T. Oberg, and Alexander G. Ioannidis. Ultra-low-power superconductor logic. *Journal of Applied Physics*, 109(10):103903, 2011.

[38] D. S. Holmes, A. L. Ripple, and M. A. Manheimer. Energy-efficient superconducting computing[mdash]power budgets and requirements. *IEEE Trans. Appl. Supercond.*, 23:1701610, 2013.

[39] R. C. Jaklevic, John Lambe, A. H. Silver, and J. E. Mercereau. Quantum interference effects in Josephson tunneling. *Phys. Rev. Lett.*, 12:159–160, Feb 1964.

[40] B.D. Josephson. Possible new effects in superconductive tunnelling. *Physics Letters*, 1(7):251 – 253, 1962.

[41] B.D. Josephson. Supercurrents through barriers. *Advances in Physics*, 14(56):419–451, 1965.

[42] S. O. Kasap. *Principles of Electronic Materials and Devices, Third Edition*. McGraw-Hill Education, 2005.

[43] D. E. Kirichenko, S. Sarwana, and A. F. Kirichenko. Zero static power dissipation biasing of RSFQ circuits. *IEEE Transactions on Applied Superconductivity*, 21(3):776–779, June 2011.

[44] C. Klose. *Spin Triplet Superconductivity in Conventional Superconductor/Ferromagnetic Hybrid Systems*. Bachelor's Thesis, Michigan State University, 2010.

[45] Carolin Klose, Trupti S. Khaire, Yixing Wang, W. P. Pratt, Norman O. Birge, B. J. McMorran, T. P. Ginley, J. A. Borchers, B. J. Kirby, B. B. Maranville, and J. Unguris. Optimization of spin-triplet supercurrent in ferromagnetic Josephson junctions. *Phys. Rev. Lett.*, 108:127002, 2012.

[46] T. Kontos, M. Aprili, J. Lesueur, F. Genêt, B. Stephanidis, and R. Boursier. Josephson Junction through a Thin Ferromagnetic Layer: Negative Coupling. *Phys. Rev. Lett.*, 89:137007, Sep 2002.

[47] T. Kontos, M. Aprili, J. Lesueur, and X. Grison. Inhomogeneous superconductivity induced in a ferromagnet by proximity effect. *Phys. Rev. Lett.*, 86:304–307, Jan 2001.

[48] L. D. Landau and E. M. Lifschitz. *Lehrbuch der Theoretischen Physik*. Bd. IX, Akademie-Verlag, Berlin, 1980.

[49] B. Landman. Calculation of threshold curves for Josephson quantum interference devices. *IEEE Transactions on Magnetics*, 13(1):871–874, Jan 1977.

[50] Timofei I. Larkin, Vitaly V. Bol'ginov, Vasily S. Stolyarov, Valery V. Ryazanov, Igor V. Vernik, Sergey K. Tolpygo, and Oleg A. Mukhanov. Ferromagnetic Josephson switching device with high characteristic voltage. *Applied Physics Letters*, 100(22), 2012.

[51] K. K. Likharev and V. K. Semenov. RSFQ logic/memory family: a new Josephson-junction technology for sub-terahertz-clock-frequency digital systems. *IEEE Transactions on Applied Superconductivity*, 1(1):3–28, March 1991.

[52] J. Matisoo. Critical currents and current distributions in Josephson junctions. *Journal of Applied Physics*, 40(4):1813–1820, 1969.

[53] D. E. McCumber. Effect of ac impedance on dc voltage-current characteristics of superconductor weak-link junctions. *Journal of Applied Physics*, 39(7):3113–3118, 1968.

[54] W. H. Meiklejohn and C. P. Bean. New magnetic anisotropy. *Phys. Rev.*, 105:904–913, Feb 1957.

[55] Th. Mühge, N. N. Garif'yanov, Yu. V. Goryunov, G. G. Khaliullin, L. R. Tagirov, K. Westerholt, I. A. Garifullin, and H. Zabel. Possible origin for oscillatory superconducting transition temperature in superconductor/ferromagnet multilayers. *Phys. Rev. Lett.*, 77:1857–1860, Aug 1996.

[56] O. A. Mukhanov. Energy-efficient single flux quantum technology. *IEEE Transactions on Applied Superconductivity*, 21(3):760–769, June 2011.

[57] Bethany M Niedzielski, E. C. Gingrich, Reza Loloee, W. P. Pratt, and Norman O. Birge. S/F/S Josephson junctions with single-domain ferromagnets for memory applications. *Supercond. Sci Technol.*, 28(8):085012, 2015.

[58] V. A. Oboznov, V. V. Bol'ginov, A. K. Feofanov, V. V. Ryazanov, and A. I. Buzdin. Thickness Dependence of the Josephson Ground States of Superconductor-Ferromagnet-Superconductor Junctions. *Phys. Rev. Lett.*, 96:197003, 2006.

[59] H. Kammerling Onnes. The resistance of pure mercury at helium temperatures. *Leiden Comm.*, 120b, 122b, 124c, Sep 1911.

[60] R. D. Parks. *Superconductivity, Vol 2*. Marcel Dekker, New York, NY, USA, 1969.

[61] W. H. Press, B. P. Flannery, S. A. Teukolsky, and W. T. Vetterling. *Numerical Recipes*. Cambridge Univ. Press, Cambridge, 1988.

[62] Z. Radović, L. Dobrosavljević-Grujić, A. I. Buzdin, and John R. Clem. Upper critical fields of superconductor-ferromagnet multilayers. *Phys. Rev. B*, 38:2388–2393, Aug 1988.

[63] Zoran Radović, Marko Ledvij, Ljiljana Dobrosavljević-Grujić, A. I. Buzdin, and John R. Clem. Transition temperatures of superconductor-ferromagnet superlattices. *Phys. Rev. B*, 44:759–764, Jul 1991.

[64] N. D. Rizzo, D. Houssameddine, J. Janesky, R. Whig, F. B. Mancoff, M. L. Schneider, M. DeHerrera, J. J. Sun, K. Nagel, S. Deshpande, H. J. Chia, S. M. Alam, T. Andre, S. Aggarwal, and J. M. Slaughter. A fully functional 64 Mb DDR3 ST-MRAM built on 90 nm CMOS technology. *IEEE Transactions on Magnetics*, 49(7):4441–4446, July 2013.

[65] J. W. A. Robinson, Gábor B. Halász, A. I. Buzdin, and M. G. Blamire. Enhanced Supercurrents in Josephson Junctions Containing Nonparallel Ferromagnetic Domains. *Phys. Rev. Lett.*, 104:207001, May 2010.

[66] J. W. A. Robinson, S. Piano, G. Burnell, C. Bell, and M. G. Blamire. Critical current oscillations in strong ferromagnetic $\pi$ junctions. *Phys. Rev. Lett.*, 97:177003, 2006.

[67] J. W. A. Robinson, S. Piano, G. Burnell, C. Bell, and M. G. Blamire. Zero to $\pi$ transition in superconductor-ferromagnet-superconductor junctions. *Phys. Rev. B*, 76:094522, Sep 2007.

[68] V. V. Ryazanov. Coupling of two superconductors through a ferromagnet: evidence for a $\pi$ junction. *Phys. Rev. Lett.*, 86:2427–2430, 2001.

[69] Hermann Sellier, Claire Baraduc, Francois Lefloch, and Roberto Calemczuk. Temperature-induced crossover between 0 and $\pi$ states in S/F/S junctions. *Phys. Rev. B*, 68:054531, Aug 2003.

[70] V. Shelukhin, A. Tsukernik, M. Karpovski, Y. Blum, K. B. Efetov, A. F. Volkov, T. Champel, M. Eschrig, T. Löfwander, G. Schön, and A. Palevski. Observation of periodic $\pi$-phase shifts in ferromagnet-superconductor multilayers. *Phys. Rev. B*, 73:174506, May 2006.

[71] Nicola A. Spaldin. *Magnetic Materials, Fundamentals and Applications*. Cambridge University Press, Cambridge, 2011.

[72] D Sprungmann, K Westerholt, H Zabel, M Weides, and H Kohlstedt. Josephson tunnel junctions with ferromagnetic Fe 0.75 Co 0.25 barriers. *Journal of Physics D: Applied Physics*, 42(7):075005, 2009.

[73] W. C. Stewart. Current-voltage characteristics of Josephson junctions. *Applied Physics Letters*, 12(8):277–280, 1968.

[74] E. C. Stoner and E. P. Wohlfarth. A mechanism of magnetic hysteresis in heterogeneous alloys. *Philosophical Transactions of the Royal Society of London A: Mathematical, Physical and Engineering Sciences*, 240(826):599–642, 1948.

[75] C. Strunk, C. Sürgers, U. Paschen, and H. v. Löhneysen. Superconductivity in layered Nb/Gd films. *Phys. Rev. B*, 49:4053–4063, Feb 1994.

[76] National Security Agency Superconducting Technology Assessment. Available at. *https://www.nitrd.gov/pubs/nsa/sta.pdf*, 2005.

[77] Claudia D. Tesche and John Clarke. dc SQUID: Noise and optimization. *Journal of Low Temperature Physics*, 29(3):301–331, 1977.

[78] C. D. Thomas, M. P. Ulmer, and J. B. Ketterson. Superconducting tunnel junction base electrode planarization. *J. App. Phys.*, 84(1):364–367, 1998.

[79] Michael Tinkham. *Introduction to Superconductivity, Second Edition*. Dover Publications, Inc., New York, 1996.

[80] Won-Tien Tsang and T. Van Duzer. dc analysis of parallel arrays of two and three Josephson junctions. *Journal of Applied Physics*, 46(10):4573–4580, 1975.

[81] M. H. Volkmann, A. Sahu, C. J. Fourie, and O. A. Mukhanov. Implementation of energy efficient single flux quantum digital circuits with sub-aj/bit operation. *Superconductor Science and Technology*, 26(1):015002, 2013.

[82] Y. Wang, W. P. Pratt Jr, and N. O. Birge. Area-dependence of spin-triplet supercurrent in ferromagnetic Josephson junctions. *Phys. Rev. B*, 85:214522, 2012.

[83] M. Weides, M. Kemmler, E. Goldobin, D. Koelle, R. Kleiner, H. Kohlstedt, and A. Buzdin. High quality ferromagnetic 0 and $\pi$ Josephson tunnel junctions. *Appl. Phys. Lett.*, 89:122511, 2006.